

**MODELLING ELECTRONIC AND  
STRUCTURAL PROPERTIES OF GRAPHENE  
AND TRANSITION METAL CHALCOGENIDE  
NANOSTRUCTURES**

**A Thesis Submitted to  
the Graduate School of Engineering and Sciences of  
İzmir Institute of Technology  
in Partial Fulfillment of the Requirements for the Degree of**

**DOCTOR OF PHILOSOPHY**

**in Physics**

**by  
Hediye Duygu ÖZAYDIN**

**July 2016  
İZMİR**

We approve the thesis of **Hediye Duygu ÖZAYDIN**

**Examining Committee Members:**

---

**Prof. Dr. Ramazan Tuğrul Senger**  
Department of Physics, İzmir Institute of Technology

---

**Assoc. Prof. Dr. Özgür Çakır**  
Department of Physics, İzmir Institute of Technology

---

**Assit. Prof. Dr. Özgeç Ebil**  
Department of Chemical Engineering, İzmir Institute of Technology

---

**Prof. Dr. Oğuz Gülseren**  
Department of Physics, Bilkent University

---

**Assoc. Prof. Dr. Cem Sevik**  
Department of Mechanical Engineering, Anadolu University

**29 July 2016**

---

**Prof. Dr. Ramazan Tuğrul Senger**  
Supervisor, Department of Physics  
İzmir Institute of Technology

---

**Prof. Dr. Ramazan Tuğrul Senger**  
Head of the Department of  
Physics

---

**Prof. Dr. Bilge KARAÇALI**  
Dean of the Graduate School of  
Engineering and Sciences

# ACKNOWLEDGMENTS

I would like to express my gratitude to all people supporting me for all the period of my thesis. First and foremost, my utmost gratitude to Prof. Dr. R. Tuğrul Senger, whose sincerity, help, motivation and encouragement I am very indebt to. I also would like thank Assoc. Prof. Dr. Hasan Şahin for his priceless and endless contributions, suggestions and support. I am sincerely grateful to my groupmates Cihan Bacaksız, Fadıl İyikanat, and Mehmet Yağmurcukardeş for their friendship and outstanding collaborations. This thesis would certainly be lifeless without their colorful contributions. Last, but not least, I wish to express my special thanks to my love, my husband, my best friend Serdar Özaydın and my little babyboy Arel Deniz. I deeply appreciate them for encouraging me to follow my dreams and their endless love.

# ABSTRACT

## MODELLING ELECTRONIC AND STRUCTURAL PROPERTIES OF GRAPHENE AND TRANSITION METAL CHALCOGENIDE NANOSTRUCTURES

The purpose of this thesis is to investigate the electronic and structural properties of one- and two-dimensional materials such as graphene, graphene-like transition metal chalcogenides by using density functional theory. The single-atom thickness of graphene sheet is a novel material and attracts great interest due to its unique features. In recent years, theoretical and experimental studies on graphene provide quick knowledge and have opened up possibilities for many other two-dimensional new materials. Among these materials, especially transition metal chalcogenides have recently been the focus of studies of condensed matter physics.

Unlike many superior properties of graphene, lack of band gap in electronic structure have highlighted the necessity of such transition metal chalcogenides materials for electronic applications. As compared to graphene, transition metal chalcogenides have various physical properties and possess sizable band gaps, for this reason they are promising candidate for many applications.

Many experiments have revealed that the surfaces of graphene and graphene-like structures can play an active role as a host surface for clusterization of metal atoms. Motivated by these observations, we investigate characteristic properties of Pt atoms on graphene,  $\text{MoS}_2$  and  $\text{TaS}_2$ . Similarly,  $\text{TiSe}_2$  is very recently synthesized two-dimensional transition metal dichalcogenide material and stable in 1T phase. Two-dimensional  $\text{TiSe}_2$  has a metallic electronic property and widely studied material. We analyze how to change the structural and electronic properties of  $\text{TiSe}_2$  by functionalization with hydrogen atom. Again to the effects of hydrogenation on two-dimensional  $\text{TiSe}_2$  monolayer we also study the structural and electronic properties of this material in nanoribbon form. At the same time,  $\text{PtSe}_2$  which is also very recently synthesized two-dimensional transition metal dichalcogenide and stable in 1T phase like  $\text{TiSe}_2$ , its nanoribbon structural and electronic properties have also been investigated and compared with  $\text{TiSe}_2$  nanoribbons. Finally,  $\text{TiS}_3$  which is also transition metal chalcogenide but entirely different crystal structure, is recently widely studied materials. The structural and electronic properties as well as carrier mobility and strain response of  $\text{TiS}_3$  nanoribbons have been investigated.

Besides many comprehensive theoretical studies, a lot of experimental studies are available about the synthesis of these materials. In brief, these materials which tackles a

contemporary and rapidly developing field, the nanoribbon form and functionalization of them that hold promise for many other applications.

# ÖZET

## GRAFEN ve GEÇİŞ METALİ KALKOJENİT NANOYAPILARIN ELEKTRONİK ve YAPISAL ÖZELLİKLERİNİN MODELLENMESİ

Bu tezin amacı, grafen ve benzeri geçiş metali kalkojenitlerin bir ve iki boyutlu nano yapılarının elektronik ve yapısal özelliklerinin yoğunluk fonksiyoneli teorisi ile incelenmesidir. Tek atom kalınlığındaki grafen, bilinen ilk iki boyutlu nanomalzemedir ve benzersiz özellikleri nedeniyle oldukça ilgi çekmektedir. Son yıllarda yapılan grafen araştırmaları, gerek deneysel gerekse teorik olarak hızlı bir bilgi birikimi sağlayarak farklı birçok 2 boyutlu yeni malzemelerin de önünü açmıştır. Bu malzemeler arasında özellikle geçiş metali kalkojenitleri yakın zamanlarda yapılan yoğun madde fiziği araştırmalarının odağı olmuştur.

Grafen malzemesinin birçok üstün özelliğine rağmen, bant aralığının olmayışı elektronik uygulamalarda geçiş metali kalkojenitleri gibi malzemelerin gerekliliği öne çıkarmıştır. Grafene kıyasla geçiş metali kalkojenitlerinin fiziksel özellikleri daha çeşitlidir ve yasak bant aralığının varlığı, pek çok elektronik uygulama alanı için umut vermektedir.

Grafen ve benzeri yüzeylerde yapılan deneyler çeşitli metal atomlarının yüzeyde hızlı difüzyonlarının mümkün olduğunu ve bunların atom öbekleri oluşturma eğiliminde olduklarını ortaya koymuştur. Yaptığımız çalışmada Pt atomlarının grafen,  $\text{MoS}_2$  ve  $\text{TaS}_2$  üzerindeki karakteristik davranışları incelenmiştir. Benzer şekilde,  $\text{TiSe}_2$  malzemesi yeni sentezlenmiş iki boyutlu geçiş metali dikalkojenitidir ve 1T fazında metalik özellik gösteren bu malzeme oldukça fazla çalışılmıştır. Bu iki-boyutlu malzemenin hidrojen atomu ile fonksiyonelleştirdiğimizde yapısal ve elektronik özelliklerinin nasıl değiştiği araştırılmıştır. Yine bu malzemenin nanoşeritlerinin elektronik ve yapısal özellikleri ile, benzer 1T fazında ve yeni sentezlenmiş olan iki-boyutlu  $\text{PtSe}_2$  malzemesinin nanoşeritlerinin elektronik özellikleri kıyaslanmıştır. En son olarak da, geçiş metali kalkojeniti olan ama tamamen farklı kristal yapıya sahip ve son zamanlarda oldukça fazla çalışılan  $\text{TiS}_3$  malzemesinin, nanoşeritlerinin yapısal ve elektronik özelliklerinin yanısıra mobilite ve mekanik gerilim altında elektronik yapısının nasıl değiştiğine bakılmıştır.

Teorik olarak yapılan kapsamlı birçok çalışmanın yanısıra deneysel olarak bu malzemelerin sentezi konusunda da çok fazla yeni çalışma mevcuttur. Kısacası, konusu güncel ve hızla gelişen bir alana giren bu malzemelerin nanoşeritleri ve işlevselleştirmeleri birçok uygulama alanı için umut vaad etmektedir.

# TABLE OF CONTENTS

LIST OF FIGURES .....	ix
LIST OF TABLES .....	xiii
CHAPTER 1. INTRODUCTION .....	1
1.1. Graphene.....	1
1.2. Transition Metal Chalcogenides .....	4
CHAPTER 2. METHODOLOGY - DENSITY FUNCTIONAL THEORY .....	8
2.1. Schrödinger Equation and Density Functional Theory .....	8
2.1.1. Thomas-Fermi Theory .....	9
2.1.2. The Hohenberg-Kohn Theorems .....	10
2.1.3. The Kohn-Sham Approach .....	12
2.2. Exchange-Correlation Energy .....	14
2.2.1. Local Density Approximation .....	15
2.2.2. Generalized Gradient Approximation .....	15
2.3. The Plane-wave Basis Sets and Pseudopotential Approach .....	16
2.4. Computational Package .....	18
CHAPTER 3. PT CLUSTERS ON GRAPHENE, $\text{MOS}_2$ , $\text{TAS}_2$ .....	19
3.1. Computational Details .....	20
3.2. Adsorption and migration of single Pt atom .....	21
3.3. $\text{Pt}_n$ clusters on graphene and transition metal dichalcogenides .....	24
3.3.1. $\text{Pt}_2$ Clusters .....	24
3.3.2. $\text{Pt}_3$ Clusters .....	25
3.3.3. $\text{Pt}_4$ Clusters .....	27
CHAPTER 4. TUNING ELECTRONIC AND MAGNETIC PROPERTIES OF $\text{TISE}_2$ MONOLAYER .....	29
4.1. Computational Details .....	30
4.2. $\text{TiSe}_2$ Monolayer .....	31
4.3. Adsorption of Single Hydrogen Atom .....	31

4.4. The Effects of Full One- and Two-Side Hydrogenation .....	32
4.5. Hydrogenated $\text{TiSe}_2$ Monolayers on $\text{HfX}_2$ .....	36
CHAPTER 5. ELECTRONIC AND MAGNETIC PROPERTIES OF ZIGZAG AND ARMCHAIR EDGED $\text{TiSe}_2$ AND $\text{PtSe}_2$ NANORIBBONS .....	40
5.1. Computational Details .....	40
5.2. Two-Dimensional Monolayer $\text{TiSe}_2$ .....	41
5.3. Nanoribbons of 1T- $\text{TiSe}_2$ .....	43
5.3.1. Electronic Properties .....	44
5.4. Hydrogen Termination of Edges .....	48
5.5. Pristine Single Layer and Nanoribbons of 1T- $\text{PtSe}_2$ .....	50
CHAPTER 6. WIDTH-INDEPENDENT BAND-GAP: $\text{TiS}_3$ NANORIBBONS ....	57
6.1. Computational Details .....	58
6.2. Structural Properties and Edge Energetics .....	58
6.3. Width-Dependent Electronic Structure .....	60
6.3.1. Mechanical Properties and Response to Strain .....	63
6.3.2. Carrier Mobility .....	66
6.4. Edge Termination .....	69
CHAPTER 7. CONCLUSION .....	72
REFERENCES .....	75



# LIST OF FIGURES

<u>Figure</u>	<u>Page</u>
Figure 1.1. (Color online) Primitive unit cell of the honeycomb structure of graphene with the reciprocal lattice vectors and corresponding Brillouin zone (BZ) having special k-points $\Gamma$ , M, and K. Calculated electronic band structure of graphene. ....	2
Figure 1.2. (Color online) Schematic representation of the periodic table in which about 40 different layered transition metal dichalcogenides exist. The transition metal and three chalcogen elements are highlighted blue and yellow in the periodic table, respectively. (from Ref. Kuc, 2014) .....	4
Figure 1.3. (Color online) Atomic structure of a typical transition metal dichalcogenides, such that TMDs have a hexagonal structure with an upper and lower sublattice of chalcogen atoms (yellow) and a middle layer of transition metal atom (purple). ....	5
Figure 2.1. (Color online) How to employ DFT. General algorithm for self-consistent DFT calculation. ....	14
Figure 3.1. (Color online) Top views of the atomic structures of (a) graphene, (b) 1H-MoS <sub>2</sub> and (c) 1T-TaS <sub>2</sub> and possible adsorption sites: the hollow site (H), the bridge site (B), the top-Mo site (Mo) and the top-Ta site (Ta). S1 and S2 refer to the point on top of a S atom of upper and lower chalcogen layers in 1T-TaS <sub>2</sub> , respectively. ....	21
Figure 3.2. Variation of energy for a single Pt adatom along the symmetry points (shown in Fig.3.1) of single layer graphene, MoS <sub>2</sub> and TaS <sub>2</sub> . Zero of energy is set to the energy of the most favorable site. ....	23
Figure 3.3. (Color online) Possible configurations of Pt <sub>n</sub> clusters on the surface of monolayers of graphene, MoS <sub>2</sub> and TaS <sub>2</sub> . ....	24
Figure 3.4. (Color online) Most stable configurations for Pt <sub>n</sub> -clusters on three different substrates, graphene (left column), MoS <sub>2</sub> (middle column) and TaS <sub>2</sub> (right column). The red balls denote Pt atoms. ....	26
Figure 4.1. (Color online) Top and side views of 1T-TiSe <sub>2</sub> monolayer with its band structure (left-panel) and corresponding partial density of states. The dashed red vectors show the unitcell of the structure. ....	32

Figure 4.2.	Top and side views of (a) TiSe <sub>2</sub> monolayer with one-side fully covered by hydrogen atoms (TiSe <sub>2</sub> -1H), and (b) TiSe <sub>2</sub> monolayer with both sides fully covered by hydrogen atoms (TiSe <sub>2</sub> -2H), with the dashed white area is for the unitcell of the structures. ....	34
Figure 4.3.	(Color online) The spin-polarized band structures of (a) TiSe <sub>2</sub> -1H and (b) TiSe <sub>2</sub> -2H monolayers. The $E_F$ is at 0. The red and blue dashed curves represent spin-up and spin-down bands, respectively. ....	35
Figure 4.4.	(Color online) The spin charge density difference of TiSe <sub>2</sub> -1H structures top and side views, for the antiferromagnetic (AFM) and ferromagnetic (FM) states where yellow (blue) colors represent the majority (minority) spin states. The spin charge density difference is plotted at same isosurface value of 0.003 e/Å <sup>3</sup> . ....	36
Figure 4.5.	(Color online) The PBE band structures of (a) HfSe <sub>2</sub> , and (b) HfS <sub>2</sub> monolayers, where red curves are for spin-up while dashed blue curves are spin down. The $E_F$ level is set to the valence band maximum. ....	37
Figure 4.6.	(Color online) Top and side views of hydrogenated monolayers on HfX <sub>2</sub> (X=Se, S). Their band structures are shown at the bottom of the figure, where the red and blue (dashed) curves represent spin-up and spin-down bands, respectively. The $E_F$ is set 0 eV. ....	38
Figure 5.1.	(Color online) (a) Atomic structure of monolayer 1T-TiSe <sub>2</sub> with top and side views where the dashed yellow area denotes the unitcell of the monolayer, and (b) the band structure calculated with PBE and HSE06, (c) partial density of states as calculated with PBE. Labels M1 and M2 are discussed in Fig. 5.6. ....	42
Figure 5.2.	(Color online) Top view of (a) zigzag and (b) armchair TiSe <sub>2</sub> nanoribbons. The unitcell is indicated by the dashed box. ....	43
Figure 5.3.	(Color online) Energy gap of zigzag ( $2 \leq N_z \leq 10$ ) and armchair ( $2 \leq N_a \leq 10$ ) 1T-TiSe <sub>2</sub> nanoribbons as function of the ribbon width. Dashed curves are exponential fits. ....	45
Figure 5.4.	(Color online) Different magnetic interaction cases for (a) TiSe <sub>2</sub> -5ZNR and (b) TiSe <sub>2</sub> -5ANR. ....	46
Figure 5.5.	(Color online) Electronic band structure of a series of zigzag and armchair nanoribbons of 1T-TiSe <sub>2</sub> by using the PBE method. ....	47

Figure 5.6. (Color online) Band decomposed charge density plots of monolayer and $N_z=3,4,7,8$ nanoribbons of $\text{TiSe}_2$ where Z1 and Z2 are shown in the band-structures (see Fig. 5.5). Inset shows the $\Gamma$ -point charge densities of M1 and M2 band edges (shown in Fig. 5.1) of 2D $\text{TiSe}_2$ . . . . .	48
Figure 5.7. (Color online) $\text{TiSe}_2$ -3ANR band structure and band decomposed charge densities of $N_a=3,4,7,8$ nanoribbons of $\text{TiSe}_2$ where the A1 and A2 refer to the states indicated in Fig. 5.5. . . . .	49
Figure 5.8. (Color online) Passivation of the edge states with hydrogen atoms (blue colored) for the zigzag and armchair nanoribbons. . . . .	50
Figure 5.9. (Color online) Band structures for zigzag and armchair nanoribbons where the edge atoms are passivated by hydrogen atoms. . . . .	51
Figure 5.10. (Color online) Band structure and density of states (DOS) of monolayer $\text{PtSe}_2$ . . . . .	52
Figure 5.11. (Color online) Band structures for zigzag and armchair edged $\text{PtSe}_2$ nanoribbons. . . . .	53
Figure 5.12. (Color online) Band structures of $\text{PtSe}_2$ -7ZNR and the hydrogenated $\text{PtSe}_2$ -7ZNR-H (and right side for the similar case of armchair nanoribbons.) The red solid and blue dashed lines are showed the spin-up and spin-down channels, respectively. . . . .	54
Figure 5.13. (Color online) Band structures for zigzag and armchair edged $\text{PtSe}_2$ nanoribbons. . . . .	54
Figure 5.14. (Color online) Band structures for zigzag and armchair edged $\text{PtSe}_2$ nanoribbons. . . . .	55
Figure 6.1. (Color online) (a) Top view and side view of an 8- <b>a</b> - $\text{TiS}_3$ NR. $a$ and $b$ are the lattice vectors of the 2D $\text{TiS}_3$ . The dashed lines indicate the unitcell of the 8- <b>a</b> - $\text{TiS}_3$ NR. The bonds at the edge are labeled by 1-5. (b) The lattice constant and edge energy of different <b>a</b> - $\text{TiS}_3$ NRs. The red dashed line indicates the lattice constant along $a$ of the 2D $\text{TiS}_3$ . (c) The same as (a) but for a 6- <b>b</b> - $\text{TiS}_3$ NR. (d) The same as (b) but for 6- <b>b</b> - $\text{TiS}_3$ NRs. . . . .	60
Figure 6.2. (Color online) (a) The band structures of a 10- <b>a</b> - $\text{TiS}_3$ NR obtained by GGA-PBE. Spin-up and spin-down channels are presented by red solid and blue dashed curves, respectively. The Fermi level is set to zero. (b) The magnetization charge density of the 10- <b>a</b> - $\text{TiS}_3$ NR. . . . .	61

Figure 6.3. (Color online) (a) The band structures of an 8- <b>b</b> -TiS <sub>3</sub> NR obtained by GGA-PBE and HSE06, and the charge density of its CBM and VBM states. (b) The band gap as a function of the <b>b</b> -TiS <sub>3</sub> NR width $N$ . Both GGA-PBE and HSE06 results are given. The dashed lines are the values for the 2D case. ....	62
Figure 6.4. The calculated 1D elastic modulus for <b>a</b> -TiS <sub>3</sub> NRs and <b>b</b> -TiS <sub>3</sub> NRs, as function of the NR width. ....	64
Figure 6.5. (Color online) (a) The band gap of <b>b</b> -TiS <sub>3</sub> NRs as function of tensile strain $\varepsilon$ . (b) The band structure of an 8- <b>b</b> -TiS <sub>3</sub> NR with $\varepsilon=0, 4\%$ and $8\%$ . The dots indicate the CBM and VBM states. (c) The CBM and VBM charge density of a 4- <b>b</b> -TiS <sub>3</sub> NR which is locally strained with $8\%$ . ....	65
Figure 6.6. Carrier mobility for <b>b</b> -TiS <sub>3</sub> NRs. The inset shows the calculated effective mass $m^*$ of electrons and holes for different ribbon widths. $m_0$ is the mass of a free electron. ....	68
Figure 6.7. (Color online) Band dispersions of a (a) 8- <b>a</b> -TiS <sub>3</sub> NR and (b) 8- <b>b</b> -TiS <sub>3</sub> NR in which the edge atoms are passivated by hydrogen (red colored) atoms. The solid and dashed curves are spin-up and spin-down components. Insets: side view of edge structure. ....	70

# LIST OF TABLES

<u>Table</u>	<u>Page</u>
Table 3.1. Calculated parameters for $Pt_n$ clusters on graphene, 1H-MoS <sub>2</sub> and 1T-TaS <sub>2</sub> respectively; stable configurations for the $Pt_n$ -cluster/substrate systems, total magnetic moment of the cluster $M_{total}$ ( $\mu_B$ ), binding energy per Pt atom $E_b$ (eV/atom) and the average charge transferred between the surface and the Pt cluster $\Delta\rho$ . Positive values of $\Delta\rho$ correspond to charge donation to the Pt cluster. ....	22
Table 4.1. The optimized lattice parameters of bare TiSe <sub>2</sub> , TiSe <sub>2</sub> -1H (with one-side hydrogenation) and TiSe <sub>2</sub> -2H (both sides hydrogenated), $c$ is the Se-Se distance in the vertical direction, $d_{Ti-Se}$ is the Ti-Se bond length, $d_{Se-H}$ is the Se-H bond length, $EC$ denotes electronic character of the structures and $M_{total}$ is the total magnetic moment per supercell. ....	33
Table 6.1. The lengths of the edge bonds of a 8- <b>a</b> -TiS <sub>3</sub> NR and an 6- <b>b</b> -TiS <sub>3</sub> NR, and the corresponding values in a TiS <sub>3</sub> monolayer. The labels of bonds are shown in Fig. 6.1 .....	59
Table 6.2. Calculated effective mass of hole ( $m_h^*$ ) and electron ( $m_e^*$ ), deformation potential constants for VBM ( $E_v$ ) and CBM ( $E_c$ ), elastic modulus ( $C_{1D}$ and $C_{2D}$ ), and carrier mobility for hole and electron ( $\mu_h$ and $\mu_e$ ) at 300 K for TiS <sub>3</sub> monolayer and the <b>b</b> -TiS <sub>3</sub> NRs. $m_0$ is the mass of a free electron. ....	66

# CHAPTER 1

## INTRODUCTION

Two-dimensional (2D) materials and ultrathin films have historically been one of the most extensively studied classes of materials and have been investigated for over the 50 years, because of the abundance of unusual physical phenomena that occur when charge and heat transport is confined into a plane (Butler et al., 2013). Carbon is a basic element of nature which has a central focus in both life and physical sciences. Since the isolation of graphene (Novoselov et al., 2004) in 2004, there has been growing interest in the field because of its potential applications in future nanoelectronic devices (Neto et al., 2009). At the same time, the rapid pace of progress in graphene has led to exploration of other 2D materials (Wang et al., 2012; Mak et al., 2010; Yin et al., 2011).

Electronic devices are everywhere in our lives since miniaturization has allowed extremely powerful devices to be portable. Miniaturization itself was made possible thanks to the development of nanoelectronics. Thus, the identification and production of low dimensionality materials (Nicolosi et al., 2013; Eda et al., 2011) have opened up a range of applications especially specialised electronic devices (Zhu et al., 2013; Li et al., 2012). Theoretical calculations have become essential in this field because the control of electronic properties and confinement effects all due to reduced dimensionality.

Therefore, specific materials of interest in this thesis are low dimensional materials such as graphene, transition metal chalcogenides, also including their one-dimensional nanoribbon forms. Before dealing with the structural and electronic properties of these nanostructures with adsorption of metal atoms, hydrogenation or their nanoribbon form; we will explore a more detailed discussion about these materials starting with the most well-known graphene and comparing its structural and electronic properties with other layered nanostructures.

### 1.1. Graphene

In 2004, Andre Geim and Kostya Novoselov at Manchester University managed to extract single-atom-thick crystallites (graphene) from bulk graphite (Novoselov et al., 2004). In fact, numerous attempts to synthesize two-dimensional atomic crystals have

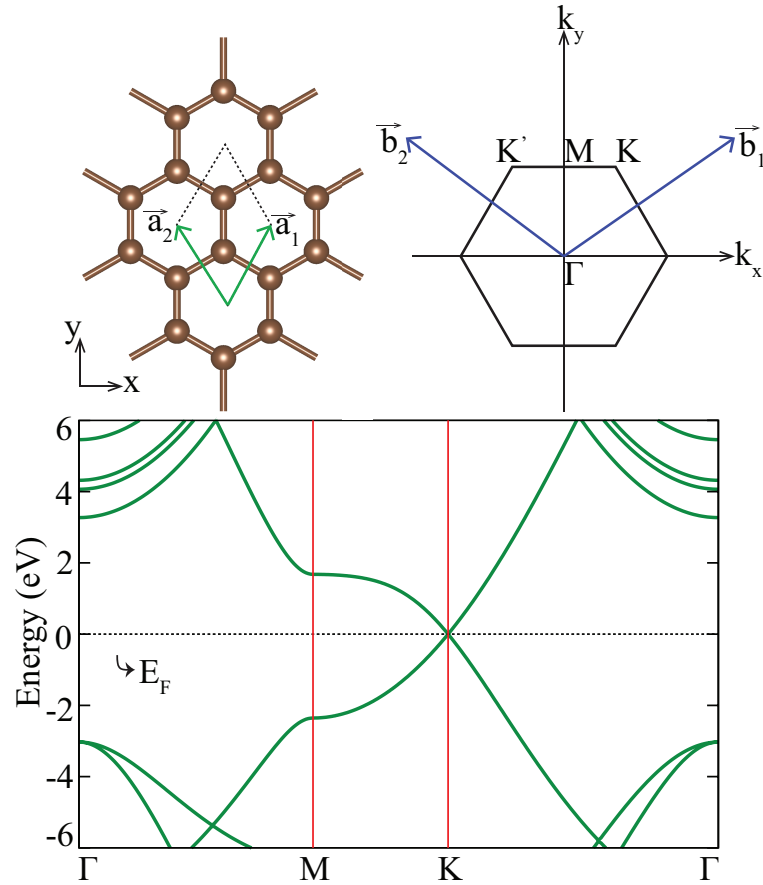


Figure 1.1. (Color online) Primitive unit cell of the honeycomb structure of graphene with the reciprocal lattice vectors and corresponding Brillouin zone (BZ) having special k-points  $\Gamma$ , M, and K. Calculated electronic band structure of graphene.

usually failed (Oshima and Nagashima, 1997), and commonly belief that 2D materials are thermodynamically unstable and thus can not be used in applications (Peierls, 1934, 1935; Landau and Lifshitz, 1980). Stable graphene has disproved previous theories, since then, graphene has been the center of theoretical and experimental studies. Graphene is a single-layer of graphite with covalently bonded 2D honeycomb structure of carbon atoms. The primitive vectors of hexagonal lattice structure and the high symmetry points of the reciprocal lattice vectors are shown in Fig.1.1. The lattice vectors can be written as:

$$\mathbf{a}_1 = a\left(\frac{3}{2}, \frac{\sqrt{3}}{2}\right), \quad \mathbf{a}_2 = a\left(\frac{3}{2}, -\frac{\sqrt{3}}{2}\right). \quad (1.1)$$

where  $a \approx 1.42 \text{ \AA}$  is the nearest carbon-carbon distance. The reciprocal lattice vectors are given by:

$$\mathbf{b}_1 = \frac{2\pi}{3a}(\sqrt{3}, 1, 0) \quad \mathbf{b}_2 = \frac{2\pi}{3a}(-\sqrt{3}, 1, 0). \quad (1.2)$$

This kind of lattice occurs due to  $sp^2$  hybridization of carbon atoms. Carbon has four valence orbitals;  $2s$ ,  $2p_x$ ,  $2p_y$ ,  $2p_z$ .  $sp^2$  hybridization is created by one  $2s$  and two  $2p$  ( $2p_x$ ,  $2p_y$ ) electrons of the carbon. Every carbon atom creates  $\sigma$  bonds with three other carbon atoms. In other words, graphene consists of covalently bonded carbon atoms and this strong binding comes from the  $\sigma$  bonds. However, the last  $2p_z$  orbitals electron where  $z$  shows the perpendicular direction to the  $x$ - $y$  plane of graphene layer, remains unpaired and creates the  $\pi$  and  $\pi^*$  bonding. The perpendicular  $\pi$  bond is weak Van der Waals bond and hence, each graphene layer is weakly interacting (Wallace, 1947; Dubois et al., 2009). Due to this unpaired electron, the electronic property of graphene can be characterized as a zero band gap semiconductor (or alternatively as a semi-metal). As can be seen from Fig.1.1(c) the conduction and valance bands cross linearly at point K at the Fermi level ( $E_F$ ), so the two points (K and K') at the corners of graphene's Brillouin Zone (BZ) is of particular importance for the electronic properties. These points are called Dirac points and their positions are given by:

$$\mathbf{K} = \left( \frac{2\pi}{3\sqrt{3}a}, \frac{2\pi}{3a} \right), \quad \mathbf{K}' = \left( -\frac{2\pi}{3\sqrt{3}a}, \frac{\sqrt{2}\pi}{3a} \right). \quad (1.3)$$

The linear electronic band dispersion leads to the term massless Dirac fermions because electrons and holes at these special points of BZ have zero effective mass (Novoselov et al., 2005). Moreover, graphene displaying exceptional properties; such as Klein tunneling, anomalous quantum hall effect and the ambipolar effect and also even at room temperature the mobility is really high (around  $15.000 \text{ cm}^2/\text{Vs}$ ) (Novoselov et al., 2007; Robinson, 2012).

However, pristine graphene lacks a finite band gap, and it is essential for electronic devices. Thus, for nanoelectronics and optics, it is necessary to open a band gap in graphene by different methods such as chemical functionalization by an atom (the mostly studied one is hydrogenation) or molecule (Ryu et al., 2008; Pumera and Wong, 2013; Jaiswal et al., 2011), cutting graphene in nanoribbon form or explore other 2D materials





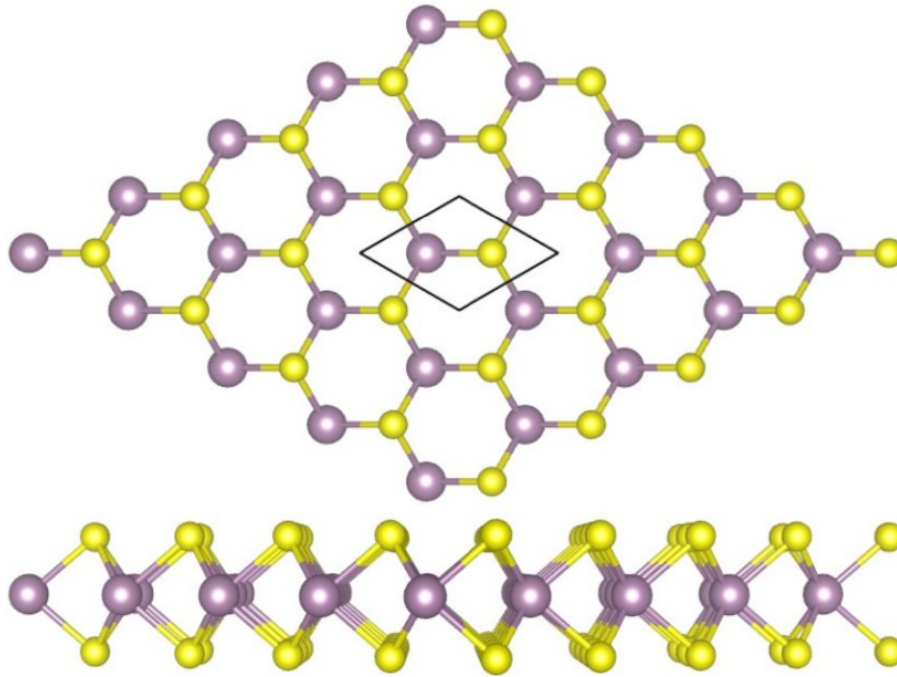


Figure 1.3. (Color online) Atomic structure of a typical transition metal dichalcogenides, such that TMDs have a hexagonal structure with an upper and lower sublattice of chalcogen atoms (yellow) and a middle layer of transition metal atom (purple).

elements Mo and W, as well as group X with elements Pd and Pt. Typical 2D TMCs are transition metal dichalcogenides (TMDs) which belong to a class of layered compounds and always present  $\text{MX}_2$  stoichiometry where M is a transition metal atom, and X is one of the chalcogens; sulfur, selenium or tellerium (Chhowalla et al., 2013a). TMDs are not atomically thin instead they are arranged in triatomic layers with a metal atom in the middle that is strongly covalent bonded to chalcogenide atoms located above and below (Wang et al., 2012), while the interlayer interactions are weak van der waals. see Fig.1.3.

These materials have 2D hexagonal lattices like graphene while each metal atom has six nearest chalcogen atoms instead of three neighboring carbon atoms in graphene. Furthermore, TMDs phases posses two types of atomic arrangements: in both the metal atom centre is either honeycomb (or trigonal prismatic) 1H or centered honeycomb (or octohedral) 1T structures; both can be viewed as positively charged plane of transition metal atom sandwiched between two planes of negatively charged chalcogen atoms (Ataca et al., 2012). The structural properties like lattice parameters, the difference of metal atoms affects slightly for the same chalcogen atom. For example, in-sheet lattice constants

of NbS<sub>2</sub> and TaS<sub>2</sub> sheets are only 0.15 Å longer than MoS<sub>2</sub> and WS<sub>2</sub> ones. However, different chalcogen atoms change the lattice parameters significantly. The diselenide and ditelluride Mo sheets increase the thickness to 3.3 and 3.6 Å, respectively.

Although the difference of chalcogen atoms affects the structural properties, it has little influence on the electronic properties. TMDs encompass a wide variety of electronic properties including metals, semi-metals, insulators and semiconductors with direct and indirect band gaps. For example, the mostly studied MoS<sub>2</sub> has an indirect band gap of 0.9 eV in the bulk form, while at the monolayer limit it gradually shifts to direct band gap with a value of 1.8 eV (Zhu et al., 2011; Mak et al., 2010), which agrees well with the photoluminescence experiments (Splendiani et al., 2010; Eda et al., 2011). The other most prominent TMDs are MoSe<sub>2</sub>, WS<sub>2</sub> and WSe<sub>2</sub> that have been widely studied for applications in electronics since they have analogous semiconducting properties. However, both the NbX<sub>2</sub> and TaX<sub>2</sub> sheets become metals.

The band gap in most semiconducting TMDs, whether in bulk or monolayer, are comparable to the 1.1 eV band gap in silicon, making them suitable for use as digital transistors. The transition to direct band gap in the monolayer form has important implications for photonics, optoelectronics and sensing. One of the most important applications of semiconductors is for transistors in digital electronics. Radisavljevic *et al.* have recently demonstrated that MoS<sub>2</sub> can be used to fabricate transistors with high electron mobility and high current on/off ratios (Radisavljevic et al., 2011; Miro et al., 2014).

As a result, the large band gaps seen in several members of TMDs family make them attractive channel materials in electronics. And, while devices based on MoX<sub>2</sub> (or WX<sub>2</sub> where X=S, Se) materials are blooming (Radisavljevic and Kis, 2013; Lopez-Sanchez et al., 2013), the properties and applications of other 2D transition metal chalcogenides materials are relatively new but exciting and rapidly expanding area of research.

The goal of this thesis is to examine graphene and transition metal chalcogenide two- and one-dimensional nanostructures using the *ab initio* calculation methods to calculate the structural and electronic properties. The organization of this thesis as follows: Chapter 2 briefly describes the theoretical background and approximations of the computational methods. Chapter 3 is related with the adsorption of transition metal atoms on graphene and graphene-like transition metal dichalcogenide nanostructures. Chapter 4 is related with the functionalization of 1T-TiSe<sub>2</sub> monolayer with hydrogenation, while in Chapter 5 we present the structural and electronic properties of zigzag and armchair edged nanoribbons of this material. At the end of this chapter, very recently synthesized 1T-PtSe<sub>2</sub> electronic properties is also presented in one-dimensional (nanoribbon)

form. Chapter 6 is related the entirely different crystal structure of  $\text{TiS}_3$  where the electronic properties, mobility and strain response of  $\text{TiS}_3$  nanoribbons are presented. Finally, Chapter 7 is conclusions summarizing the results of our studies.

# CHAPTER 2

## METHODOLOGY - DENSITY FUNCTIONAL THEORY

In this chapter, we briefly discuss the fundamental aspects of Density Functional Theory (DFT) such that the theoretical framework, computational methodologies and approximations of DFT which have been utilized in the following chapters on various systems. Instead of giving complete introduction to DFT calculations, a comprehension of the theoretical basis is needed to understand the methods used in this study. In this regard, this chapter provides aspects of the computational methodology of the simulations.

### 2.1. Schrödinger Equation and Density Functional Theory

In 1926, the Austrian physicist Erwin Schrödinger published his pioneering paper which included his famous equation (Schrödinger equation) that describes the how the wavefunction of a physical system evolves over time (Schrödinger, 1926). The quantum mechanical wavefunction contains full information of a given system. In principle, all information about a system can be extracted by solving the many-body Schrödinger equation in order to obtain that wave function.

$$\hat{H}\psi_i(\mathbf{r}, \mathbf{R}) = E_i\psi_i(\mathbf{r}, \mathbf{R}). \quad (2.1)$$

$\hat{H}$  is the Hamiltonian operator and  $E_i$  is the energy eigenvalue corresponding to many body time-independent wave function,  $\Psi_i(\mathbf{r}, \mathbf{R})$ .

Unfortunately, except for the simple systems (H or He) it is impossible to obtain the exact solutions of many-body Schrödinger equation even with computational methods. Evidently, some approximations must be involved to render the problem soluble with some tricky. The first approximation to this kind of systems is to the electrons as moving in the field of fixed nuclei. Due to the significant difference between nucleus and electron masses, the nuclei move much slower than the electrons and so the nuclei can be treated as stationary. This approach, which is known as the Born-Oppenheimer approximation

(Born and Oppenheimer, 1927), the wave function can be factorized as  $\Psi_{total} = \Psi_{electronic} \times \Psi_{nuclear}$ . However, it is still very hard to solve an electronic problem and for this reason more efficient approaches and valid approximations are implemented. DFT is developed for this aim (Parr, 1980; Koch and Holthausen, 2015), and the simplest definition of DFT, which is a method of obtaining an approximate solution to the Schrödinger equation of a many-body system where the electron density is the central quantity.

Using this theory, the complicated many-body wave function is replaced with a simpler quantity, the electron density  $n(\mathbf{r})$  for describing properties of the system. In other words, the properties of a many-body system can be determined by using functionals (name refers to functions of a function) and hence the name of the theory comes from the use of functionals of the electron density. In the last forty years, DFT is the most popular and versatile methods in condensed-matter and computational physics. The electronic structure, magnetic, mechanical and transport properties of various systems can be investigated in practice by using the DFT based computational codes.

### 2.1.1. Thomas-Fermi Theory

Historically, it can be stated that DFT is loosely based on the Thomas-Fermi model, since first attempts to use the electron density for the total energy, are based on the early works of Thomas and Fermi (Thomas, 1927; Fermi, 1927). Indeed, this theory is the boorish model of modern DFT, however it largely fails for neglect the exchange and correlation effects. The kinetic energy term was proposed in their model with a very simple way, which was based on the non-interacting electrons in homogenous electron gas and in terms of electron density:

$$T_{TF}[n(\mathbf{r})] = \frac{3h^2}{10m} \left(\frac{3}{8\pi}\right)^{2/3} \int n(\mathbf{r})^{5/3} d\mathbf{r} \quad (2.2)$$

It is noted that the Fermi wave vector is related with the electron density as:

$$n(\mathbf{r}) = \frac{k_F^3}{3\pi^2} \quad (2.3)$$

Finally, the total energy is completely obtained in terms of electron density  $n(\mathbf{r})$  using the

classical expression for electron-electron and nucleus-nucleus potential.

$$E_{TF}[n(\mathbf{r})] = \frac{3h^2}{10m} \left(\frac{3}{8\pi}\right)^{2/3} \int n(\mathbf{r})^{5/3} d\mathbf{r} - Z \int \frac{n(\mathbf{r})}{r} d\mathbf{r} + \int \frac{n(\mathbf{r})n(\mathbf{r}')}{|\mathbf{r} - \mathbf{r}'|} d\mathbf{r}d\mathbf{r}' \quad (2.4)$$

They assumed that the ground state density that minimize the total energy is calculated under the constraint of;

$$\int n(\mathbf{r})d\mathbf{r} = N \quad (2.5)$$

However, the electronic structure so as the total energy calculations is not accurate enough with Thomas-Fermi model, because exchange and correlation are totally absent and so the theory cannot predict shell structures of atoms or molecular bonding. Nevertheless, Thomas-Fermi model is very important because it set up a basis for DFT.

### 2.1.2. The Hohenberg-Kohn Theorems

In 1964, Hohenberg and Kohn proved two fundamental theorems which introduced the foundation of DFT (Hohenberg and Kohn, 1964). In this work they have shown that the electron density as basic variable, and all information about electronic system can be determined by using electron density in these theorems.

*Theorem 1* : For any system of interacting particles in an external potential  $V_{ext}(\mathbf{r})$ , the electron density is uniquely determined apart from a trivial additive constant. In other words, all information about the ground state properties of a many-body system can be described by the electron density.

The proof for the first part of the theorem can be considered as two different external potentials  $V_{ext}$  and  $V'_{ext}$  differing by more than a constant and which give the same ground state density  $n(\mathbf{r})$ . Obviously, they belong to distinct Hamiltonians  $H$  and  $H'$ , and which have distinct ground state wave functions  $\psi$  and  $\psi'$ . Similarly, the ground state energies are  $E_0$  and  $E'_0$  for  $H$  and  $H'$ , respectively. Taking the  $\psi'$  as a trial wave function

for  $H$  since it is not ground state wave function of  $H$ , and calculating expectation values:

$$\begin{aligned} E_0 < \langle \psi' | H | \psi' \rangle &= \langle \psi' | H | \psi' \rangle + \langle \psi' | (H - H') | \psi' \rangle \\ &= E_0' + \int n(\mathbf{r}) [V_{ext}(\mathbf{r}) - V'_{ext}(\mathbf{r})] d\mathbf{r} \end{aligned} \quad (2.6)$$

Similarly,

$$\begin{aligned} E_0' < \langle \psi | H' | \psi \rangle &= \langle \psi | H' | \psi \rangle + \langle \psi | (H - H') | \psi \rangle \\ &= E_0 + \int n(\mathbf{r}) [V_{ext}(\mathbf{r}) - V'_{ext}(\mathbf{r})] d\mathbf{r} \end{aligned} \quad (2.7)$$

Adding equations 2.6 and 2.7 gives an inconsistent result,

$$E_0 + E_0' < E_0' + E_0 \quad (2.8)$$

Thus, they have been showed that there cannot be any other external potential giving the same ground state density  $n(\mathbf{r})$ , which means that ground state density uniquely determines (to within a constant) the external potential. In this way, the total energy can be written as a functional for an arbitrary external potential in terms of electron density;

$$E_V[n(\mathbf{r})] = F[n(\mathbf{r})] + \int n(\mathbf{r}) V(\mathbf{r}) d\mathbf{r} \quad (2.9)$$

where  $F[n(\mathbf{r})]$  is a universal Hohenberg-Kohn functional and it is completely independent from the system.

*Theorem 2* : The total energy of the system can be expressed as a functional of the electron density, and the global minimum value of this functional is the exact ground state.

The proof for the second part of the theorem, let us assume that any other trial electron density function  $n'(\mathbf{r})$  which determines its own properties  $V'_{ext}$ ,  $\psi'$  and  $H'$  and such that giving an energy higher or equal to the ground state energy.



$$E[n'(\mathbf{r})] \geq E[n(\mathbf{r})] \quad (2.10)$$

where  $E[n(\mathbf{r})]$  is evaluated total energy for the ground state electron density  $n(\mathbf{r})$ .

$$\begin{aligned} \langle \psi' | H | \psi' \rangle &= F[n'(\mathbf{r})] + \int n'(\mathbf{r}) V_{ext}(\mathbf{r}) d\mathbf{r} \\ &= E[n'(\mathbf{r})] \geq E[n(\mathbf{r})] \\ E_0 &= \langle \psi | H | \psi \rangle \end{aligned} \quad (2.11)$$

It follows that the total energy of the system can be minimized according to the correct electron density instead of electronic wave functions. It means that all properties of a system can be completely derived from the ground state density and it is much simpler to deal with total electron density rather than full electronic wave function.

### 2.1.3. The Kohn-Sham Approach

After the idea of Hohenberg-Kohn theorems, in 1965 the idea was further developed by Kohn-Sham such that they provided applicability for modern DFT by publishing a paper (Kohn and Sham, 1965). Since the explicit form of universal function  $F[n(\mathbf{r})]$  do not known, they proposed an alternative approach for the kinetic energy functional. The idea of the Kohn-Sham approach is replacing interacting system with non-interacting system, in such a way, that the ground state of the interacting system is equal to the electronic density of the fictitious non-interacting system. With this assumption the total density of the N electron system can be written as:

$$n(\mathbf{r}) = 2 \sum_{i=1} |\varphi_i(\mathbf{r})|^2 \quad (2.12)$$

where factor 2 comes from spin states and  $\varphi_i$  are the orbitals of non-interacting system. With the kinetic term

$$T[n(\mathbf{r})] = -\frac{1}{2} \sum_{i=1}^N \int \varphi_i \nabla^2 \varphi_i^* d\mathbf{r} \quad (2.13)$$

The effective single-particle potential can be written in more detail and the single particle Kohn-Sham equation is given as:

$$\left[ \frac{-\hbar^2}{2m} + V_{ext}(\mathbf{r}) + V_H(\mathbf{r}) + V_{XC}(\mathbf{r}) \right] \varphi_i = \epsilon_i \varphi_i \quad (2.14)$$

where  $V_H$  is the Hartree potential

$$V_H = e^2 \int \frac{n(\mathbf{r}')}{|\mathbf{r} - \mathbf{r}'|} d\mathbf{r}' \quad (2.15)$$

and  $V_{XC}$  is the exchange-correlation potential

$$V_{XC}(\mathbf{r}) = \frac{\delta E_{XC}[n(\mathbf{r})]}{\delta n(\mathbf{r})} \quad (2.16)$$

The universal density functional can be written in the following form by using the new form of  $T[n(\mathbf{r})]$ .

$$F[n(\mathbf{r})] = T[n(\mathbf{r})] + \frac{e^2}{2} \int \int \frac{n(\mathbf{r})n(\mathbf{r}')}{|\mathbf{r} - \mathbf{r}'|} d\mathbf{r}d\mathbf{r}' + E_{XC} \quad (2.17)$$

Using this functional in the total energy functional in eqn. 2.9, the total energy of a system can be expressed as a functional of the charge density which is known as Kohn-Sham density functional:

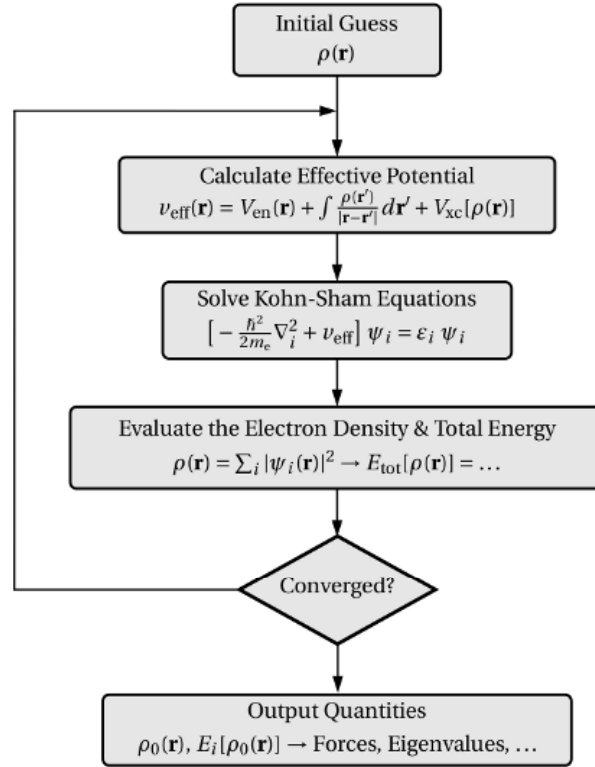


Figure 2.1. (Color online) How to employ DFT. General algorithm for self-consistent DFT calculation.

$$E_{KS}[n(\mathbf{r})] = T[n(\mathbf{r})] + \int n(\mathbf{r})V_{ext}(\mathbf{r})d\mathbf{r} + \frac{e^2}{2} \int \int \frac{n(\mathbf{r})n(\mathbf{r}')}{|\mathbf{r} - \mathbf{r}'|} d\mathbf{r}d\mathbf{r}' + E_{XC} \quad (2.18)$$

As a result of Kohn-Sham density functional theory, the complicated many-body problem can be solved by mapping exactly the set of self-consistent single-particle equations. Since the effective potential depends on the actual electron density  $n(\mathbf{r})$ , the solutions of Kohn-Sham equations can be obtained by an iterative self-consistent-field (SCF) procedure. This can be achieved by constructing an initial guess of the electron density for a given configuration of ionic positions, solving the equations, obtaining a new density and energy and repeating this process until convergence in both quantities is reached which is shown in Fig. 2.1

## 2.2. Exchange-Correlation Energy

In the previous sections, we briefly described the DFT theory, and saw that the only missing ingredient is exchange-correlation term.  $E_{XC}$  is very complex because it includes all the remaining complicated non-analytical electronic contributions and so some approximations need to be made. In this reason, there are several approximations like local density approximation (LDA) (Jones and Gunnarsson, 1989) and generalised gradient approximation (GGA) (Perdew et al., 1992) which are derived in order to deal with exchange-correlation functional.

### 2.2.1. Local Density Approximation

LDA is a class of and simplest approximation to the exchange-correlation energy functional in DFT, as suggested by Kohn-Sham (Jones and Gunnarsson, 1989) which is based on the homogeneous electron gas such that the density can be treated locally as a uniform electron gas. Using the LDA approach, the exchange-correlation energy at each point in the system is the same as that of an uniform electron gas of the same density and so the  $E_{XC}$  for a density  $n(r)$  is given by

$$E_{XC}^{LDA}[n(\mathbf{r})] = \int \epsilon_{XC}(\mathbf{r})n(\mathbf{r})d\mathbf{r} \quad (2.19)$$

where the  $\epsilon_{XC}(\mathbf{r})$  is exchange-correlation energy per electron at a point  $r$  in a uniform electron gas which has the same density as the electron at point  $r$ . For systems where the density varies slowly, LDA works best and generally gives very good results for some solids like nearly-free-electron metal. However, for in many simpler cases LDA finds the wrong ground state. It gives higher binding energy for molecules and solids but the chemical trends are usually well predicted. For the description of hydrogen-bonding, the LDA approach tends to fail because it does not account for van der Waals bonding.

### 2.2.2. Generalized Gradient Approximation

GGA (Perdew et al., 1992) is another functional like LDA, but the gradient of the electron density at the same position is also included, because LDA fails in situations where the density undergoes rapid changes such as in molecules. Therefore, exchange-correlation energy is described in GGA

$$E_{XC}^{GGA}[n(\mathbf{r})] = \int \epsilon_{XC}(n(\mathbf{r}), \nabla n(\mathbf{r}))n(\mathbf{r})d\mathbf{r} \quad (2.20)$$

Since the electron density is not uniform, GGA often provides more accurate results by taking into account the inhomogeneous nature of the electron density. Especially molecular geometries, binding energies and ground state energies are improved in GGA when compared to the ones obtained by LDA. However, both of the approximations is valid depending on the purpose and the system of interest. An improvement to these functionals can be made by modifying to include van der Waals interactions. Among physicists, probably the most widely used functionals proposed by Perdew, Burke, and Ernzerhof (PBE)(Perdew et al., 1996) can be given.

### 2.3. The Plane-wave Basis Sets and Pseudopotential Approach

There are some difficulties arising when the many-body problem is mapped into equivalent in an effective single-particle problem, because a very large number of ions and non-interacting electrons moving in a crystal so that the wavefunction must be calculated for very large number of electrons in the system. At the same time, since the every wave function extends over the entire crystal, infinite number of basis set is necessary in computational calculation. To overcome these difficulties, performing calculations on periodic systems and Bloch's theorem are used.

Bloch's theorem states that in a periodic solid each electron wave function can be written as the product of a periodic function and a plane wave:

$$\psi_i(\mathbf{r}) = \exp(i\mathbf{k}\cdot\mathbf{r})f_i(\mathbf{r}) \quad (2.21)$$

where  $f_i(\mathbf{r})$  ( $f_i(\mathbf{r}) = f_i(\mathbf{r}+\mathbf{T})$ ) is the lattice periodic part can be expanded using a basis set in terms of discrete plane-waves with reciprocal lattice vectors  $\mathbf{G}$  such that:

$$f_i(\mathbf{r}) = \sum_{\mathbf{G}} c_{i,\mathbf{G}} \exp(i\mathbf{G} \cdot \mathbf{r}) \quad (2.22)$$

Here, reciprocal lattice vector  $\mathbf{G}$  are defined by using the fact that  $\mathbf{G} \cdot \mathbf{l} = \pi m$  with  $\mathbf{l}$  is a lattice vector,  $m$  is an integer and  $c_{i,\mathbf{G}}$  are plane wave coefficient. Therefore wavefunction for each electron can be written as a sum of plane-waves as:

$$\psi_i(\mathbf{r}) = \sum_{\mathbf{G}} c_{i,\mathbf{k}+\mathbf{G}} \exp(i\mathbf{K}+\mathbf{G} \cdot \mathbf{r}) \quad (2.23)$$

By using the Bloch's theorem we change the problem of calculating infinite number of electronic wave functions to the one of calculating a finite number of electronic wave-functions at an infinite number of  $\mathbf{k}$ -points. Usually  $\mathbf{k}$ -points in the Brillouin zone is sampled such that electronic wave-functions in the  $\mathbf{k}$  space is represented by the single  $\mathbf{k}$ -point (Payne et al., 1992). There are several important schemes for  $\mathbf{k}$  point sampling *e.g* Monkhorst-Pack. Furthermore the computed total energy will converge as the density of  $\mathbf{k}$ -points increases (Monkhorst and Pack, 1976). In principle, an infinite number of plane-waves are required to expand the wavefunction at each  $\mathbf{k}$ -point in above sum. However, only the small kinetic energy terms are important. For this reason, an energy cut-off ( $E_{cutoff}$ ) can be imposed on plane-waves such that  $|\mathbf{k}+\mathbf{G}|^2 < E_{cutoff}$ . Introduction of this cutoff energy to the discrete plane-wave basis set produces a finite basis set. Moreover, increase or decrease of  $E_{cutoff}$  allow the control of accuracy in plane-wave calculations.

Although Bloch's theorem states that every electronic wave functions can be expressed using a discrete plane-waves, sometimes it is very difficult to deal with highly localized states such as core electrons because an extremely large plane-wave basis set may be necessary to include the all electrons of each atom in the unitcell. In order to avoid this, pseudopotential approximation can be used in which allows the expansion of electronic wave functions using a much smaller plane-waves. Since the electronic properties of solids depends on valance electrons rather than the core electrons, this approximation removes the core electrons and consider the crystal as ions and valance electrons. Therefore, only contribution comes from valance states. Several different schemes are devised for pseudopotential approximation, this thesis we always use the Projector Augmented

wave method (Blöchl, 1994).

## 2.4. Computational Package

Our calculations have been performed in this thesis are based on DFT in the framework of the plane-wave projector-augmented wave (PAW) methodology implemented in the Vienna *ab-initio* simulation package VASP (Kresse and Furthmüller, 1996; Kresse and Joubert, 1999). VASP is a computer program for atomic scale materials modelling, *e.g* electronic structure calculations and quantum-mechanical molecular dynamics, from first principles. VASP computes an approximate solution to the many-body Schrödinger equation that allows the electronic structure of systems with periodic boundary conditions to be calculated. The input is a configuration of atoms with periodic boundary conditions *e.g* crystal structure. The simplest output is the electronic structure and energy of that configuration of atoms and the forces on atoms. More complex output can be obtained, such as the electronic band structure and spin densities from spin polarized calculations.

## CHAPTER 3

### PT CLUSTERS ON GRAPHENE, $\text{MoS}_2$ , $\text{TAS}_2$

Many experiments have revealed that the surfaces of graphene and graphene-like structures can play an active role as a host surface for clusterization of transition metal atoms. In the literature, some works have concentrated on the absorption of alkali, noble and transition metals on graphene (Sahin and Ciraci, 2012; Cabria et al., 2010; Ishii et al., 2008; Uchoa et al., 2008; Chan et al., 2008). The attachment of metal nanoparticles to graphene surfaces is a very challenging problem with possible application for electro-catalysis. Regarding the growth of metal clusters on graphene, in particular the formation of platinum nanoclusters is important due to their excellent catalytic behavior (Błoński et al., 2011; Błoński and Hafner, 2011; Zhou et al., 2010). In addition, when  $\text{Pt}_n$  clusters are formed on graphene the equilibrium structure of the gas-phase of the clusters is preserved (Błoński et al., 2011) and magnetic anisotropy energies (MAE) are strongly reduced as compared to free clusters. (Błoński and Hafner, 2011) Theoretical studies have also shown that depending on the growth conditions  $\text{Pt}_n$  nanostructures with diverse structural symmetries can be formed on graphene (Błoński et al., 2011; Błoński and Hafner, 2011; Zhou et al., 2010; Huda et al., 2006).

Similar to graphene, TMDs form weakly bonded lamellar bulk structures and these van der Waals layers can host intercalation of foreign atoms and the formation of various clusters. Aydinol et al. investigated theoretically the intercalation properties of various lithium-metal-oxides, sulfides, and selenides (Aydinol et al., 1997). Ramirez and Schkatte performed a detailed study of the migration and energetics of Li adatoms on a  $\text{TiSe}_2(0001)$  surface and showed that notwithstanding the high energy barrier, direct intercalation can be possible (Ramirez and Schattke, 2001). Jishi et al. showed that the electronic density of states in  $\text{TiSe}_2$  can be significantly enhanced upon copper intercalation (Jishi and Alyahyaei, 2008). Furthermore, Meziane et al. calculated Li and Na intercalation in dichalcogenides of Tantalum and found that they are promising candidates for thermoelectric applications (Meziane et al., 2013). Experimentally, Kim et al. reported that  $\text{MoS}_2$  and  $\text{WS}_2$  can be decorated with gold atoms and the resulting gold nanoparticles tend to grow at defective sites and the resulting  $\text{MoS}_2/\text{Au}$  and  $\text{WS}_2/\text{Au}$  hybrid structures show significant enhanced electro-catalytic performance towards hydrogen evolution reactions (Kim et al., 2013). Moreover, Sreepasad et al. demonstrated the possibility of



raising the effective gate-voltage of MoS<sub>2</sub> devices by an order of magnitude through the incorporation of highly capacitive gold nanoparticles onto the surface (Sreeprasad et al., 2013). Very recently the successful functionalization of graphene membranes with platinum nanoparticles that tend to exhibit a preferred orientation was reported by Xu et al (Xu et al., 2014).

Although structural, electronic and magnetic properties of freestanding and graphene-supported Pt<sub>*n*</sub> clusters were investigated before, only very few studies are available on cluster formation on surfaces of various TMDs having different crystal symmetry. Motivated by these observations, in this chapter, we investigate theoretically the adsorption, diffusion and magnetic properties of platinum (Pt) clusters on three different two-dimensional atomic crystals (graphene, molybdenum disulfide (1H-MoS<sub>2</sub>) and tantalum disulfide (1T-TaS<sub>2</sub>)) (Ozaydin et al., 2014). We discuss:

- What are the migration characteristics of Pt atoms on different monolayer surfaces?
- How transition metal dichalcogenide (TMD) substrates having different crystal symmetries affect the formation of Pt<sub>*n*</sub> nanoclusters ( $n < 5$ )?

Therefore, in the following sections, we properly present adsorption and diffusion characteristics of single Pt atom on monolayers of graphene, MoS<sub>2</sub> and TaS<sub>2</sub>. Then, our results on the binding energies and magnetic properties of Pt<sub>2</sub>, Pt<sub>3</sub> and Pt<sub>4</sub> nanostructures on three different surfaces are given.

### 3.1. Computational Details

For Pt<sub>*n*</sub> clusters on graphene, MoS<sub>2</sub> and TaS<sub>2</sub> sheets, calculations were performed using  $5 \times 5 \times 1$  supercells which are large enough to avoid interactions between neighboring clusters. The Perdew-Burke-Ernzerhof (PBE)(Perdew et al., 1996) form of the Generalized Gradient Approximation (GGA) are adopted to describe electron exchange and correlation. The plane-wave cutoff energy is set to 500 eV in all calculations. The Brillouin Zone is sampled using a  $\Gamma$ -centered k-point mesh and a Gaussian smearing of 0.01 eV is used for total energy calculations. Structural relaxations are performed using a conjugate gradient method where total energy and atomic forces are minimized. The convergence criteria for energy is chosen as  $10^{-5}$  eV between two iteration steps, and the maximum force allowed on each atom is less than  $10^{-4}$  eV/Å. The pressure in the unit cell is held below 1 kBar in the optimized structures. Spin-polarized calculations are per-

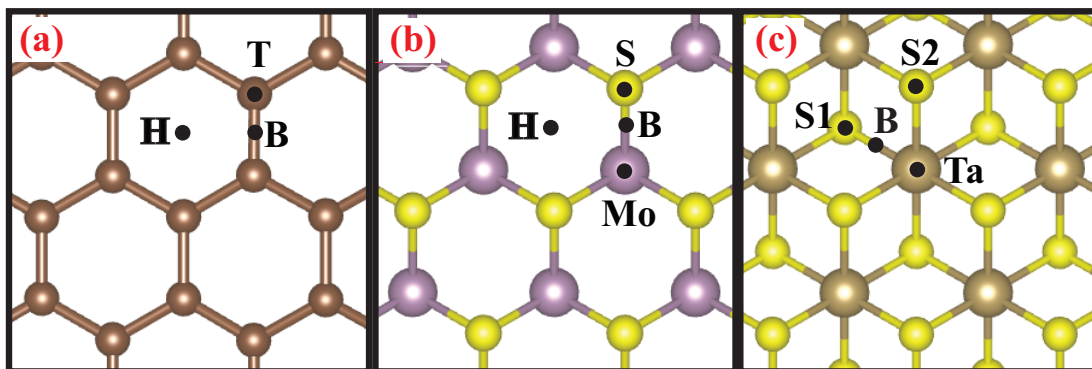


Figure 3.1. (Color online) Top views of the atomic structures of (a) graphene, (b) 1H-MoS<sub>2</sub> and (c) 1T-TaS<sub>2</sub> and possible adsorption sites: the hollow site (H), the bridge site (B), the top-Mo site (Mo) and the top-Ta site (Ta). S1 and S2 refer to the point on top of a S atom of upper and lower chalcogen layers in 1T-TaS<sub>2</sub>, respectively.

formed in all cases and atomic charges are calculated by using the Bader method. Schmidt et al. (1993); Henkelman et al. (2006).

For the determination of the most favorable adsorption sites calculations are performed by placing Pt single atoms over various high symmetry lattice points. In Table I, only the energetically most favorable sites are reported. The binding energies (per Pt atom) are calculated according to the formula  $E_b = [E(Host) + n E(Pt) - E(Host + Pt_n)]/n$ , where  $E(Host)$  is the energy of the supporting monolayer sheet,  $E(Host + Pt_n)$  is the total energy of the monolayer with Pt atom(s),  $E(Pt)$  is the energy of an isolated Pt atom and  $n$  is the number of Pt atoms in the cluster.

### 3.2. Adsorption and migration of single Pt atom

In this section, we present our results concerning favored adsorption sites, the binding energies and magnetic ground states for a single Pt atom on monolayers of graphene, MoS<sub>2</sub> and TaS<sub>2</sub>. Just like graphene, MoS<sub>2</sub> and TaS<sub>2</sub> have hexagonal crystal structure composed of layers of metal atoms (M) sandwiched between layers of chalcogen atoms (X) with stoichiometry MX<sub>2</sub>. As shown in Fig. 3.1, while MoS<sub>2</sub> has trigonal prismatic coordination, each Ta atom has octahedral coordination in monolayer TaS<sub>2</sub>. In the following discussion, trigonal prismatic and octahedral phases are referred as 1H and 1T structures, respectively. In both H and T phases the trigonally arranged monolayer

Graphene				1H-MoS <sub>2</sub>				1T-TaS <sub>2</sub>				
<i>Shape</i>	$M_{total}$	$E_b$	$\Delta\rho$	<i>Shape</i>	$M_{total}$	$E_b$	$\Delta\rho$	<i>Shape</i>	$M_{total}$	$E_b$	$\Delta\rho$	
	( $\mu_B$ )	(eV/atom)	( $e$ )		( $\mu_B$ )	(eV/atom)	( $e$ )		( $\mu_B$ )	(eV/atom)	( $e$ )	
Pt <sub>1</sub>	-	0.0	1.70	0.02	-	0.0	2.89	-0.07	-	1.0	3.71	-0.10
Pt <sub>2</sub>	Dimer	0.0	2.25	-0.02	Dimer	0.0	3.03	-0.07	Dimer	0.1	3.68	-0.01
Pt <sub>3</sub>	Triangle	0.0	2.97	-0.03	Triangle	0.0	3.35	0.08	Triangle	1.0	3.87	0.16
Pt <sub>4</sub>	Bent Rhombus	2.0	3.15	-0.11	Tetrahedral	0.0	3.60	0.03	Tetrahedral	0.3	4.01	0.21

Table 3.1. Calculated parameters for Pt<sub>n</sub> clusters on graphene, 1H-MoS<sub>2</sub> and 1T-TaS<sub>2</sub> respectively; stable configurations for the Pt<sub>n</sub>-cluster/substrate systems, total magnetic moment of the cluster  $M_{total}$  ( $\mu_B$ ), binding energy per Pt atom  $E_b$  (eV/atom) and the average charge transferred between the surface and the Pt cluster  $\Delta\rho$ . Positive values of  $\Delta\rho$  correspond to charge donation to the Pt cluster.

lattice of metal atoms is sandwiched between two chalcogen layers and hence each metal atom is surrounded by six chalcogen atoms. In contrast to the weak inter-layer interaction, metal and chalcogen atoms have strong intra-planar bonds that have a covalent character. Due to different lattice symmetries of these monolayers one can expect different diffusion characteristics for foreign atoms on these different surfaces. Our results are summarized in Table I. Diffusion pathways (see Fig. 3.2) of a Pt atom on different supporting layers were obtained by calculating the total energy on different adsorption sites along the high symmetry points.

The calculated lattice constant of the primitive unitcell of graphene is  $a = 2.46 \text{ \AA}$ . For adsorption calculations of a single platinum atom on a non-defective surface a  $4 \times 4$  graphene supercell is used. As shown in Fig. 3.1(a) there are three favorable adsorption sites on the surface of graphene: the hollow (H) site on the center of a hexagon, the bridge (B) site on the midpoint of a C-C bond, and the top (T) site directly above a carbon atom. In agreement with recent *ab-initio* calculations the bridge site is found to be the energetically most favorable site. Each Pt atom is adsorbed at the B site with binding energy of 1.70 eV. Although, an isolated platinum is in a magnetic ground state with  $2 \mu_B$  net moment, when it is adsorbed on graphene there exists no net magnetic moment. This finding is consistent with the previously reported data. (Sahin and Ciraci, 2012) Our analysis reveals that the nonmagnetic state is favored by 0.92 meV over the magnetic state with  $2 \mu_B$  net moment.

Differing from the one-atom-thick crystal structure of graphene, MoS<sub>2</sub> has a three-

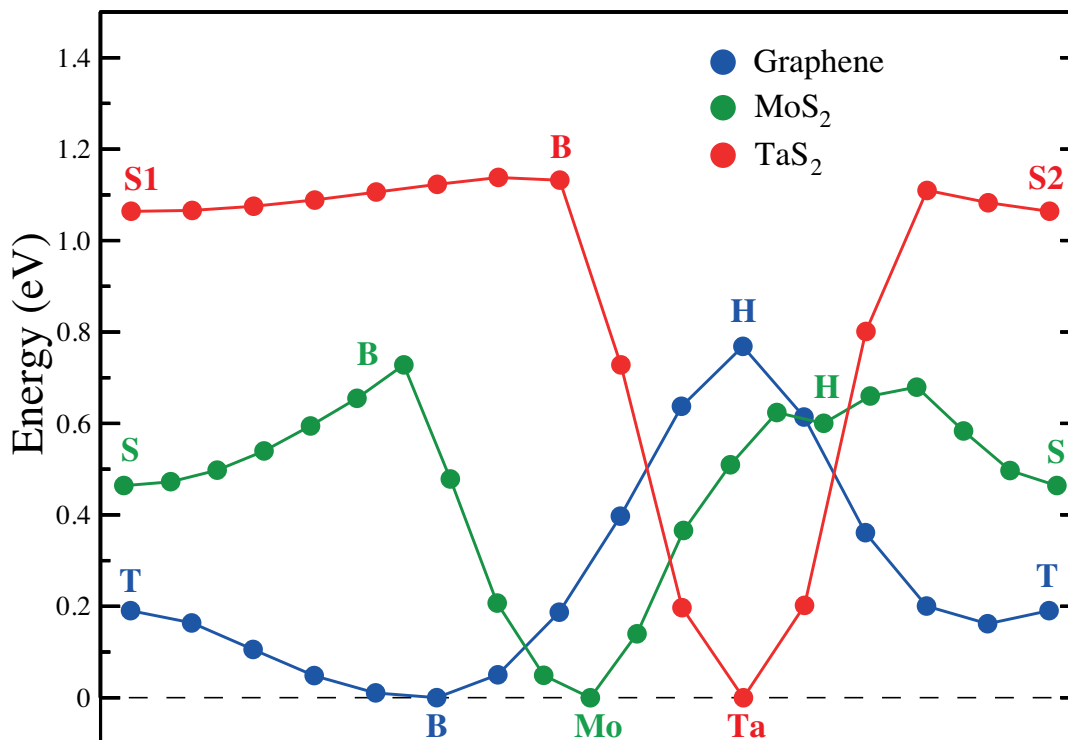


Figure 3.2. Variation of energy for a single Pt adatom along the symmetry points (shown in Fig.3.1) of single layer graphene, MoS<sub>2</sub> and TaS<sub>2</sub>. Zero of energy is set to the energy of the most favorable site.

layered structure made of trigonally arranged Mo atoms sandwiched by two S layers. The point group of graphene is  $D_{6h}$ , while the monolayer (1H) structure of MoS<sub>2</sub> belongs to the  $D_{3h}$  symmetry group. We found that the optimized lattice constant of 1H-MoS<sub>2</sub> is 3.18 Å and a 3×3 supercell is large enough to hinder the interaction between Pt atoms in adjacent cells. For the adsorption of a single Pt atom on 1H-MoS<sub>2</sub> there are four different possible sites: on top of Mo (Mo), on top of S (S), on top of a Mo-S bond (B) and on top of the hollow (H) sites (see Fig. 3.1(b)). When a Pt atom is adsorbed at the Mo site, the largest binding energy (minimum total energy) is found. It is also seen that immersion of a Pt atom to the Mo layer is not allowed at the hollow site by an energy barrier of 6.91 eV. Therefore, the most stable site of Pt atom absorption occurs at the Mo site with a binding energy of 2.89 eV.

Similar to MoS<sub>2</sub>, TaS<sub>2</sub> monolayer contains 3 layers of octahedrally coordinated S-Ta-S atoms. This monolayer (1T) structure belongs to the symmetry group of  $D_{3d}$ . However, differing from 1H-MoS<sub>2</sub>, 1T-TaS<sub>2</sub> shows metallic behavior. The optimized lattice constant of the 1T-TaS<sub>2</sub> sheet is  $a = 3.74$  Å and a 3×3 supercell is used. Calculations

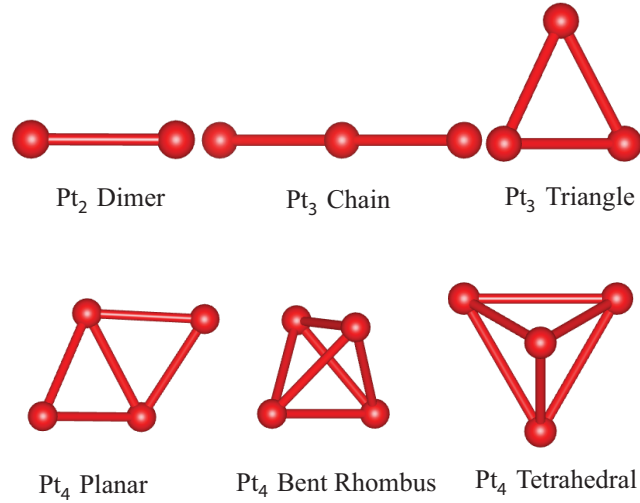


Figure 3.3. (Color online) Possible configurations of  $Pt_n$  clusters on the surface of monolayers of graphene,  $MoS_2$  and  $TaS_2$ .

of adatom Pt and monolayer  $TaS_2$  system are carried out for the Pt atom located at the four high symmetry sites, as indicated in Fig. 3.1(c): on bridge (B), on top of S (S1), on top of Ta (Ta) and on top of lower layer S atom (S2). The most favorable site for Pt atom adsorbed on  $TaS_2$  was found to be the Ta site with binding energy of  $E_b = 3.71$  eV/atom. Upon the adsorption of a Pt atom on Ta site  $TaS_2$  monolayer exhibits a spin polarized ground state with net magnetic moment of  $1 \mu_B$ .

### 3.3. $Pt_n$ clusters on graphene and transition metal dichalcogenides

In this section the formation of  $Pt_n$  clusters on various surfaces were investigated via total energy calculations. In order to accurately simulate the step-by-step nucleation of each  $Pt_n$  cluster, various configurations of  $Pt_{n-1}+Pt$  systems were considered. As shown in Fig. 3.3 there are several possible configurations for each  $Pt_n$  cluster. Although all the possible configurations of  $n$  Pt atoms that correspond to a minimum on the Born-Oppenheimer surface were considered in our calculations, only the atomic structures that correspond to the ground state geometry are presented in Fig. 3.4 for the sake of clarity.

### 3.3.1. Pt<sub>2</sub> Clusters

As shown in Fig. 3.4(a) when a Pt atom is adsorbed on the surface of graphene the most favorable adsorption site for the next Pt atom is found to be a second nearest bridge site. Due to the larger atomic radius of Pt atoms adsorption on the first nearest bridge site is not allowed. For this Pt<sub>2</sub> dimer the Pt-Pt bond length is 2.60 Å and the average Pt-C bond length is 2.15 Å. The binding energy of a Pt<sub>2</sub> dimer is calculated to be 2.25 eV/atom and therefore the formation of each dimer occurs with an energy benefit of 0.55 eV/atom. It is also found that the Pt<sub>2</sub>+graphene structure does not exhibit any spin polarization in its ground state.

As depicted in Fig. 3.4(b), when a Pt atom is adsorbed on MoS<sub>2</sub>, neither nearest top-sulfur nor nearest hollow site is the preferential site for the next Pt atom. Differing from the graphene surface, MoS<sub>2</sub> allows dimer formation on nearest top-Mo sites. Therefore a full coverage of the MoS<sub>2</sub> surface by a trigonally arranged one-atom-thick layer of Pt atoms may be possible under suitable conditions. Here the calculated binding energy of a dimer is 3.03 eV/atom and therefore the 0.14 eV/atom energy benefit shows the preferability of clusterization on the MoS<sub>2</sub> substrate. Here the Pt<sub>2</sub>+MoS<sub>2</sub> structure has a nonmagnetic ground state. In addition, our charge analysis showed that 0.07 of electrons are transferred from the Pt atoms to the surface whereas charge transfer from the Pt<sub>2</sub> clusters to the graphene surface is 0.02 electrons.

However changing the substrate to TaS<sub>2</sub> results in some differences in energetics and electronic properties of Pt<sub>2</sub> clusters. When Pt<sub>2</sub> clusters are formed on the TaS<sub>2</sub> sheet the distance between Pt-Pt is 2.85 Å and the Pt-S distance is 2.32 Å. The binding energy is  $E_b=3.68$  eV/atom and Pt atoms are both located on top of the Ta sites (see Fig. 3.4(c)). Although the most favorable configuration of two Pt atoms is a dimer as on the MoS<sub>2</sub> surface, the ground state is spin polarized with a net magnetic moment of 0.1  $\mu_B$ . Another significant difference between the two TMDs, MoS<sub>2</sub> and TaS<sub>2</sub>, is that the formation of Pt<sub>2</sub>-dimers is not energetically favorable on TaS<sub>2</sub>. It appears that the decoration of TaS<sub>2</sub> by Pt atoms may provide quite stable surface structures with new functionalities.

### 3.3.2. Pt<sub>3</sub> Clusters

For a Pt<sub>3</sub> cluster supported by single layer graphene, the energetically most stable form is a triangle-shaped cluster perpendicular to the surface. In this configuration

two Pt atoms sit on opposite B sites and the other Pt is located at the hollow site (see Fig. 3.4(d)). We have also considered flat-lying triangle and linear chain configurations which turned out to have higher energy. Since these two structures are not energetically favorable, thermal effects immediately drive the atoms to form a triangle-shaped  $\text{Pt}_3$  structure perpendicular to the surface. Consequently, clustering is favored since the binding energy is  $E_b=2.97$  eV/atom. The Pt atoms, which are located at the C-C bridge sites, have bonding length  $2.46$  Å, and the Pt-C bond length is  $2.24$  Å. Due to the weak interaction between them, it is nonmagnetic and 0.03 electrons are transferred from the surface to the Pt cluster.

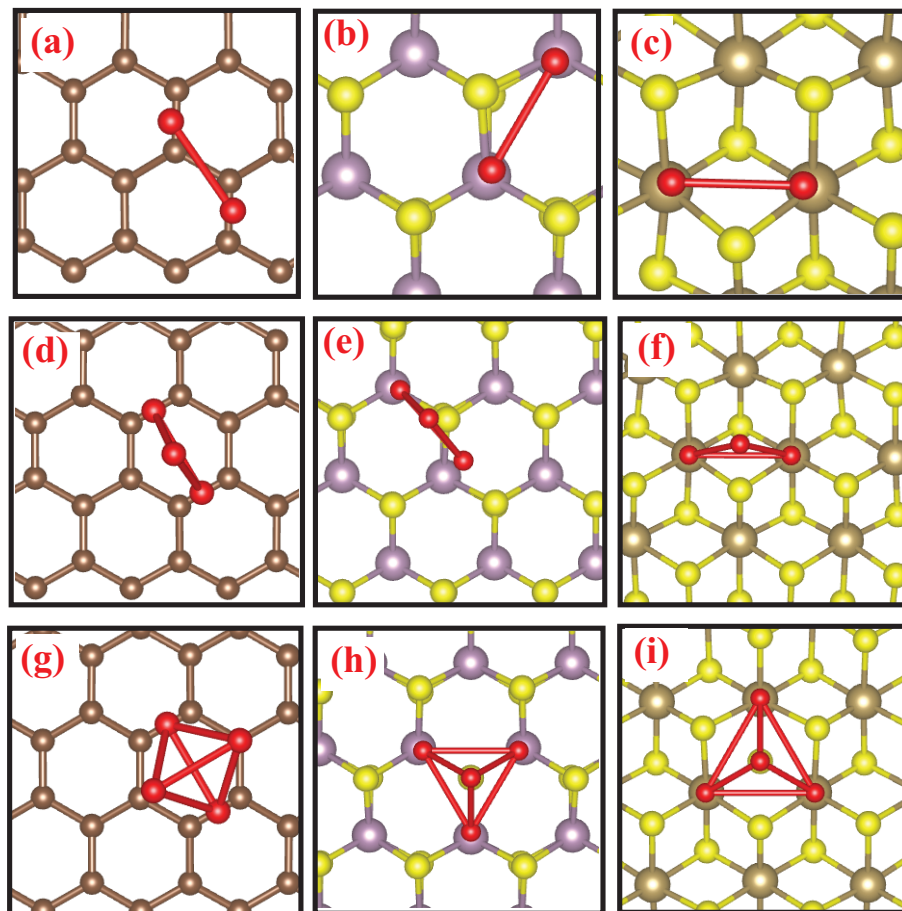


Figure 3.4. (Color online) Most stable configurations for  $\text{Pt}_n$ -clusters on three different substrates, graphene (left column),  $\text{MoS}_2$  (middle column) and  $\text{TaS}_2$  (right column). The red balls denote Pt atoms.

As discussed above for graphene, we treated both linear chain and triangular shapes for  $\text{Pt}_3$  clusters on  $\text{MoS}_2$  layer. The same behavior is shown by the  $\text{Pt}_3$ -cluster

adsorbed on MoS<sub>2</sub>. The system is inclined to form a nearly perpendicular triangle with binding energy of 3.35 eV/atom, which is depicted in Fig. 3.4(e). No significant magnetic moments are induced on the 5 × 5 MoS<sub>2</sub> layer. The average bond length of the Pt atoms is about 2.67 Å, and the length of the nearest Pt-S bond is 2.26 Å. The system is nonmagnetic and charge transfer occurs from the surface to the Pt<sub>3</sub> clusters (0.08 electrons).

On the other hand, three Pt atoms on a TaS<sub>2</sub> layer appear magnetic with a net magnetic moment of 1 μ<sub>B</sub>. The configuration shown in Fig. 3.4(f) displays a triangular shaped Pt<sub>3</sub> on graphene or MoS<sub>2</sub>, but the distance between the Pt-Pt atoms located on the Ta site is much longer and therefore the Pt-Pt interaction is weak. However the interaction between the cluster and the TaS<sub>2</sub> layer is quite strong. The two platinum atoms which sit on top of the Ta atoms have a bond length of 3.31 Å, and the distance to the other Pt atom is 2.51 Å, however the bond length with the surface is about 2.37 Å. From the Bader analysis, it appears that 0.16 electrons are given from the surface to the Pt<sub>3</sub> cluster.

### 3.3.3. Pt<sub>4</sub> Clusters

For the case of Pt<sub>4</sub>, there are three typical structures that can be formed on a surface; planar, bent rhombus or tetrahedral as shown in Fig. 3.3. The bent rhombus cluster on graphene (see Fig. 3.4(g)) is more favorable than the flat one with an energy difference of 66 meV/atom. In this configuration the length of the shortest Pt-Pt bond is 2.52 Å, and the Pt-C bond is about 2.23 Å. While the single Pt atom, the most stable Pt<sub>2</sub> and Pt<sub>3</sub> clusters on graphene are nonmagnetic, Pt<sub>4</sub> has a ferromagnetic ground state with a net magnetic moment of 2 μ<sub>B</sub>. It appears that 0.11 of electron charge are transported from the Pt atoms to the surface.

For four Pt atoms adsorbed on the MoS<sub>2</sub> surface, the most favored configuration state consists of a three dimensional tetrahedral shape where three Pt atoms are located on top of Mo, and the fourth Pt atom is bonded to the other three Pt atoms only (Fig. 3.4(h)). The average distance between the edge platinum atoms and sulfur atoms is 2.35 Å and the binding energy of the cluster is E<sub>b</sub> = 3.60 eV/atom. The plane configuration of Pt<sub>4</sub> is not a stable state. The Pt<sub>4</sub>-cluster adsorbed on the MoS<sub>2</sub> structure has a nonmagnetic ground state and the charge transfer from the surface to the adatom Pt is 0.03 electrons.

Finally, we analyzed the structural and magnetic properties of Pt<sub>4</sub> clusters on a TaS<sub>2</sub> sheet. We have compared the adsorption energies of a planar and a tetrahedron structure. Not surprisingly as shown in Fig. 3.4(i), after relaxation the Pt<sub>4</sub> clusters exhibit a tetrahedral shape on TaS<sub>2</sub> because it is 0.7 eV more favorable than the planar shape. The



Pt-Pt bond length of the edge atoms is 3.54 Å while the average distance to the S atoms is 2.37 Å. For the system of Pt<sub>4</sub>+TaS<sub>2</sub>, the magnetic properties are also investigated, and it has a degenerate ground state consisting of nonmagnetic and magnetic cases with 2 μ<sub>B</sub>. Moreover, charge transfer from the TaS<sub>2</sub> to Pt<sub>4</sub> cluster is 0.21 electrons.

As a result, we investigated the adsorption properties, the diffusion pathways and clustering of Pt atoms on graphene, 1H-MoS<sub>2</sub> and 1T-TaS<sub>2</sub> by means of density functional theory. While a single Pt atom is adsorbed on the bridge site of graphene, the top of the transition metal atom is the most favorable site on TMD substrates. It is also seen that the binding energies on TMDs are larger on 1H-MoS<sub>2</sub> and 1T-TaS<sub>2</sub>. Our total energy calculations also revealed that the formation of Pt<sub>n</sub> clusters is favorable on graphene, MoS<sub>2</sub> and TaS<sub>2</sub> substrates. We found that these substrates, with their different crystal symmetries, exhibit different absorption and diffusion characteristics. While graphene hosts an easy clusterization of Pt atoms, nucleation of Pt clusters on the surface of transition metal dichalcogenides, regardless of the 1H or 1T phase, is more difficult and can take place at higher temperatures. Due to the larger atomic separation on 1T-TaS<sub>2</sub> one can expect a smaller mobility of the clusters.

## CHAPTER 4

# TUNING ELECTRONIC AND MAGNETIC PROPERTIES OF $\text{TiSe}_2$ MONOLAYER

Despite the comprehensive research on graphene and single layer TMDs, studies on the electronic properties of the group IVB TMDs in the T phase, namely the two-dimensional 1T-MX<sub>2</sub> structures, are sparse. Nevertheless, 1T-TiSe<sub>2</sub> (titanium diselenide) (Di Salvo et al., 1976; Fang et al., 1997; Li et al., 2007; Kusmartseva et al., 2009) is an extensively studied quasi-2D TMD, which has a charge density wave (CDW) state and in condensed matter physics transitions from superconductivity to charge density wave phases has been shown to be very important (Bovet et al., 2004; Morosan et al., 2006). However, whether 1T-TiSe<sub>2</sub> is a semimetal or a semiconductor is still an open question (Rasch et al., 2008). Since TiTe<sub>2</sub> is a semi-metal with overlapping valence and conduction bands (De Boer et al., 1984; Claessen et al., 1996) and TiS<sub>2</sub> is a semiconductor with an indirect gap (Chen et al., 1980; Samuelsen et al., 1992), it can be expected that the band gap of TiSe<sub>2</sub> is smaller or even nonexistent. Note that in the periodic table selenium is in between sulfur and tellurium, and also selenium is less electronegative than sulfur. Therefore, both experimental and theoretical techniques have been used to identify the semiconducting or semimetallic nature of 1T-TiSe<sub>2</sub> (Pillo et al., 2000; Calandra and Mauri, 2011; Hildebrand et al., 2014; Rösner et al., 2014). Two-dimensional TiSe<sub>2</sub> monolayer which is a recently synthesized member of transition metal dichalcogenides (TMDs) has metallic ground state. Peng et al. (Peng et al., 2015) grew TiSe<sub>2</sub> ultrathin films on a graphitized SiC(0001) substrate by using molecular beam epitaxy (MBE). Their findings offer important insights into the nature of the charge density wave in TiSe<sub>2</sub>, and paved the way for potential applications based on its collective electronic states.

In order to achieve different applications, modifications of 2D materials intrinsic properties are often required. Taking a graphene for example, a sizable band gap is indispensable for electronic devices. To do so, several methods, such as cutting graphene into nanoribbons, or chemically functionalizing graphene by hydrogen, fluor *etc.* have been proposed (Li et al., 2008; Elias et al., 2009; Zhou et al., 2009; Han et al., 2007)

Additionally, several theoretical and experimental studies have revealed that functionalization of monolayers with hydrogen, fluor, and other adsorbands can not only mod-

ify the electronic properties of the structures, but can also induce magnetism. Sahin *et al.* (Sahin et al., 2011) have studied fluorinated graphene and they found that fluorographene (CF) display crucial features, such as high mechanical strength, charged surfaces, local magnetic moments and a wide band gap rapidly decreasing with uniform strain. Very recently, intrinsic ferromagnetism has been achieved through a new effective strategy of fluorine adsorption on MoS<sub>2</sub> nanosheets, where the fluorinated MoS<sub>2</sub> nanosheets exhibit stable ferromagnetic hysteresis at room temperature.(Gao et al., 2015) Accordingly, tuning of magnetic properties of hydrogenated MoS<sub>2</sub> monolayer from nonmagnetic to ferromagnetic, and further to nonmagnetic with the increase of tension has been reported by Shi *et al.*(Shi et al., 2013) Pan (Pan, 2014) has shown that the metallic and magnetic vanadium dichalcogenides monolayers can be made semiconducting, nonmagnetic, or antiferromagnetic by hydrogen functionalization. Similarly, Tantalum based dichalcogenides (TaX<sub>2</sub>; X= S, Se,Te) have been investigated by Manchanda *et al.* (Manchanda et al., 2015), and they showed that isotropic strain and hydrogenation yield a variety of phase transitions among magnetic and nonmagnetic states. Moreover, Cong *et al.* (Cong et al., 2015) have performed first-principles calculations to explore a variety of TMDs and the hydrogenation strategy has been applied for a part of TMDs with poor conductivity to have insight into hydrogen influence and improvement of pseudo-capacitance performance.

In particular, these both experimental and theoretical hydrogenation studies to functionalize physical properties of 2D materials have revealed some important results such as tunable band gap opening in graphene and magnetic futures in TMDs. As a result, in this chapter, we have performed first principles calculations based on density functional theory to reveal the effects of hydrogenation on two-dimensional TiSe<sub>2</sub> monolayer which is a recently synthesized member of TMDs. The structural, electronic and magnetic properties of one- and two-side hydrogenated TiSe<sub>2</sub> monolayers are systematically investigated.

## 4.1. Computational Details

The generalized gradient approximation of Perdew-Burke-Ernzerhof (GGA-PBE) is chosen as the exchange-correlation functional (including van der Waals correction (Grimme, 2006)). Energy cutoff for plane-wave expansion is set to 500 eV. For Brillouin zone integration, a 15×15×1  $\Gamma$ -centered Monkhorst-Pack k-points grid is used. A vacuum region of at least 20 Å is added in the direction normal to the nanosheet plane to prevent interactions. All the atomic positions and lattice constants are optimized where the total

energy and atomic forces are minimized. The convergence threshold for energy is chosen as  $10^{-5}$  eV and  $10^{-4}$  eV/Å for the force. The Bader analysis is used for calculating the charges on atoms.

For the determination of the stable adsorption site for hydrogen atoms on TiSe<sub>2</sub> monolayer surface, a  $4 \times 4 \times 1$  supercell is used and the binding energy, using the energy of the hydrogen molecule as reference, is calculated according to the formula:  $E_b = E(\text{TiSe}_2) + 1/2E(\text{H}_2) - E(\text{TiSe}_2 + \text{H})$ ; where  $E(\text{TiSe}_2)$  and  $E(\text{TiSe}_2 + \text{H})$  are the energies of the TiSe<sub>2</sub> supercell with and without hydrogen atom, respectively.  $E(\text{H}_2)$  is the energy of an isolated H<sub>2</sub>. Likewise, the binding energies of one- or two-side hydrogenated TiSe<sub>2</sub> monolayers on HfX<sub>2</sub> (X=S, Se) is calculated as;  $E_b = E(\text{TiSe}_2 + n\text{H}) + E(\text{HfX}_2) - E(\text{hetero.})$  where  $E(\text{hetero.})$  is the total energy of the heterostructure,  $E(\text{TiSe}_2 + n\text{H})$  and  $E(\text{HfX}_2)$  are the total energies of the isolated monolayers.

## 4.2. TiSe<sub>2</sub> Monolayer

Firstly, the structural form, electronic band dispersion, and the partial density of states (PDOS) of bare TiSe<sub>2</sub> monolayer is calculated which are summarized in Fig. 4.1. Typical TMDs have two different structural phases depending on the coordination of chalcogen atoms, where one of the trigonal prismatic (2H) or octahedral (1T) phases is thermodynamically preferred (Chhowalla et al., 2013b). TiSe<sub>2</sub> monolayer prefers the 1T phase as its ground state with a lattice constant of 3.50 Å and the corresponding Ti-Se bond length of 2.55 Å. Ti atom donates 0.7 *e* to each Se atom which indicates that the Ti-Se bonds have ionic character. According to our calculated PBE results in Fig. 4.1, 1T-TiSe<sub>2</sub> has a nonmagnetic metallic ground state, and *d* orbitals of Ti atoms ( $d_{xy}$ ,  $d_{yz}$ ,  $d_{xz}$ ) dominate near the Fermi level ( $E_F$ ), while contributions from the Se orbitals are almost negligible in that region.

## 4.3. Adsorption of Single Hydrogen Atom

For hydrogenation of monolayer TiSe<sub>2</sub>, we first investigate the most stable adsorption site for a single H atom. Previous studies showed that the hydrogen adsorption on the MoS<sub>2</sub> monolayer in which the hydrogen atom prefers to bond to the S atom (S-H bond length is 1.41) (Koh et al., 2012). Similar to hydrogen adsorption, it has been theoretically predicted that N, O, and F favor the position of top of S atom for the MoS<sub>2</sub> monolayer

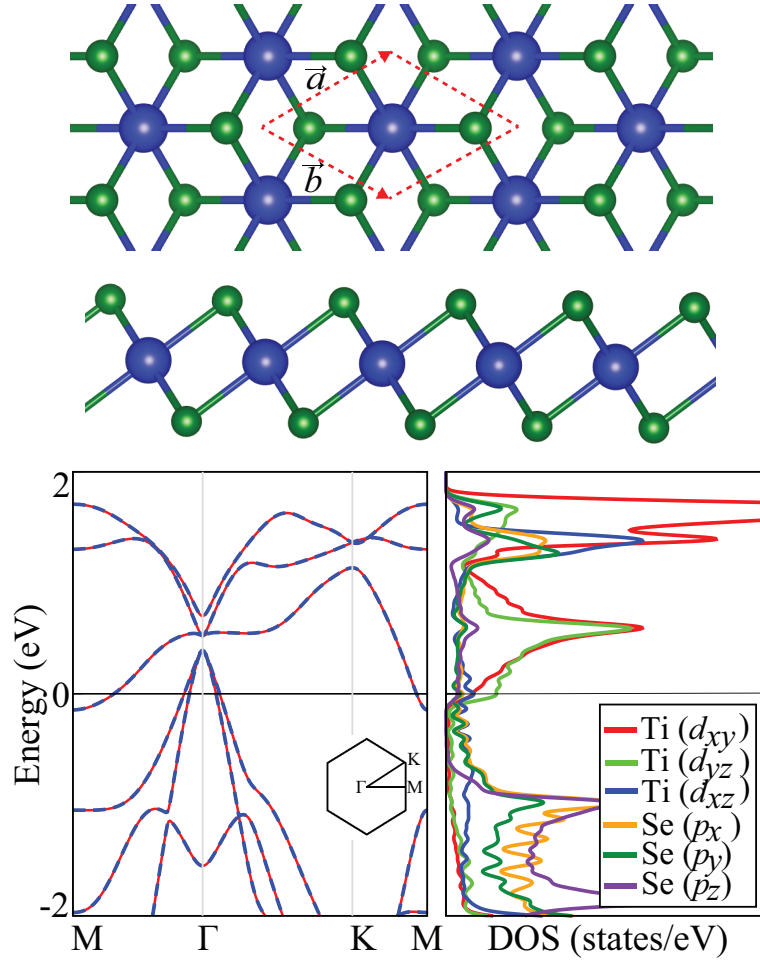


Figure 4.1. (Color online) Top and side views of 1T-TiSe<sub>2</sub> monolayer with its band structure (left-panel) and corresponding partial density of states. The dashed red vectors show the unitcell of the structure.

(He et al., 2010). Different from MoS<sub>2</sub>, while top of Ti is the most stable position to be adsorbed for F and N. However for the case of hydrogen adsorption, the calculated total energies indicate that when a hydrogen atom is adsorbed at the top of Se site which the Se-H bond length is 1.48 Å, the highest binding energy with a value of 1.70 eV (minimum total energy) is found. The total magnetic moment of the structure 1  $\mu_B$  is found. Due to small electro-negativity of H atom, 0.02  $e$  is depleted from monolayer to hydrogen-atom. Therefore, in the present study H atom is only adsorbed on TiSe<sub>2</sub> monolayer onto Se atom, and for fully-hydrogenation onto the both Se atoms which is leading to the formation of a chemical bonding of Se-H. It is noted that the situation in which H atom is only chemically bonding onto the Se atom from one-side of TiSe<sub>2</sub> monolayer can be carried out putting this monolayer on a substrate.

	$a$ (Å)	$c$ (Å)	$d_{Ti-Se}$ (Å)	$d_{Se-H}$ (Å)	$EC$	$M_{total}$ ( $\mu_B$ )
TiSe <sub>2</sub>	3.50	3.12	2.55	-	Metal	0
TiSe <sub>2</sub> -1H	3.69	2.93	2.59	1.50	Half-Metal	1
TiSe <sub>2</sub> -2H	3.64	2.97	2.57	1.52	Metal	0

Table 4.1. The optimized lattice parameters of bare TiSe<sub>2</sub>, TiSe<sub>2</sub>-1H (with one-side hydrogenation) and TiSe<sub>2</sub>-2H (both sides hydrogenated),  $c$  is the Se-Se distance in the vertical direction,  $d_{Ti-Se}$  is the Ti-Se bond length,  $d_{Se-H}$  is the Se-H bond length,  $EC$  denotes electronic character of the structures and  $M_{total}$  is the total magnetic moment per supercell.

#### 4.4. The Effects of Full One- and Two-Side Hydrogenation

After finding the most stable site for a single H, we study the optimized lattice constants for TiSe<sub>2</sub> monolayer in which one-side (Fig. 4.2a) or both of the sides (Fig. 4.2b) are fully covered by hydrogen atoms. For a convenient notation, one- and two-side hydrogenated TiSe<sub>2</sub> monolayers are denoted as TiSe<sub>2</sub>-1H and TiSe<sub>2</sub>-2H which are shown in Fig. 4.2 and also whose geometric and electronic details are listed in Table I.

The optimized lattice constant of bare TiSe<sub>2</sub> monolayer is 3.50 Å, which is extended upon hydrogenation. The structure of TiSe<sub>2</sub>-1H has a lattice constant of 3.69 Å. Compared with the bare TiSe<sub>2</sub> monolayer, the lattice constant increases by 4% (3.64 Å) for the TiSe<sub>2</sub>-2H. The vertical Se-Se distance effective width of the monolayer gets longer with H coverage on its surface(s). The Se-H bond length is 1.50 and 1.52 Å for the TiSe<sub>2</sub>-1H and TiSe<sub>2</sub>-2H monolayers, respectively.

After optimizing the lattice constants, we next investigate the electronic and magnetic properties of these structures. The results indicate that the TiSe<sub>2</sub> monolayer is qualitatively affected by hydrogenation. Fig. 4.3(a)-(b) show the calculated spin-polarized band structures of TiSe<sub>2</sub>-1H and TiSe<sub>2</sub>-2H monolayers, respectively. As we discussed in the previous subsection, bare TiSe<sub>2</sub> monolayer has metallic ground state, in contrast TiSe<sub>2</sub>-1H exhibit half-metallic property, i.e. the monolayer behaves like a metal with respect to the electrons of majority spin and like a semiconductor with respect to the electrons of minority spin. Such spin-dependent asymmetric electronic states can be utilized in spintronics applications. On the other hands, similar to its bare form TiSe<sub>2</sub>-2H is also metallic (Fig. 4.3(b)).

Besides that, it can be seen in Fig. 4.3(a), the band dispersion of the minority spin

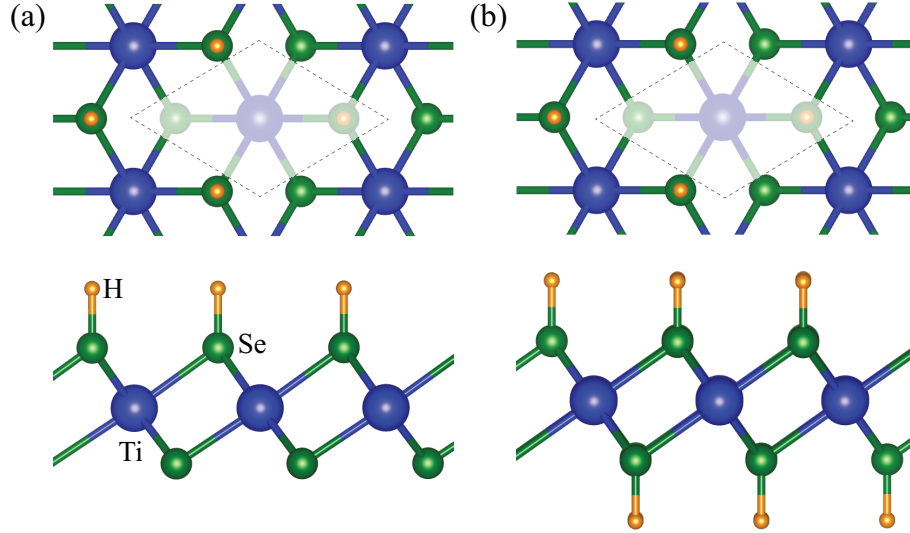


Figure 4.2. Top and side views of (a)  $\text{TiSe}_2$  monolayer with one-side fully covered by hydrogen atoms ( $\text{TiSe}_2\text{-1H}$ ), and (b)  $\text{TiSe}_2$  monolayer with both sides fully covered by hydrogen atoms ( $\text{TiSe}_2\text{-2H}$ ), with the dashed white area is for the unitcell of the structures.

(blue dashed curve) shows different parabolic curvature at the conduction band minimum around the M-point. More clearly, the curvature in the K-M direction is sharper than the  $\Gamma$ -M direction which leads to highly anisotropic electron effective masses along the zigzag (K-M) and armchair ( $\Gamma$ -M) directions. Therefore, we extracted electron effective masses in two directions  $\Gamma$ -M and K-M by parabolic fitting of the band structure. The result demonstrate that a very heavy effective mass  $m_e^*/m_e=3.37$  in the  $\Gamma$ -M direction, while light one has  $m_e^*/m_e=0.39$  in the K-M direction.

In addition, as shown in Fig. 4.3(a) significant splitting between the spin-up and spin-down states near the  $E_F$  suggests the intrinsic ferromagnetism of an  $\text{TiSe}_2\text{-1H}$  monolayer. In spin-polarized calculations, for the  $\text{TiSe}_2\text{-1H}$  structure, hydrogen donates an electron into  $\text{TiSe}_2$  monolayer, and these donated electron improves the magnetic moment of the bare structure, as a result the magnetic moments  $1.0 \mu_B$  is found for the  $\text{TiSe}_2\text{-1H}$ . The spin charge density difference is shown in Fig. for the ferromagnetic case, the metal atom Ti is carried local magnetic moments which are contributed mainly by  $d$  orbitals, while the contributions from other atoms are rather small. The calculated magnetic moments of Ti atom is  $0.86 \mu_B$  whereas, the H-bonded Se and H atoms have nearly  $0.02 \mu_B$  magnetic moments, and the uncovered Se atom has negative magnetic moment which is less than  $0.01 \mu_B$ . Therefore, the analysis demonstrate that Ti  $3d$  orbitals mainly dominate

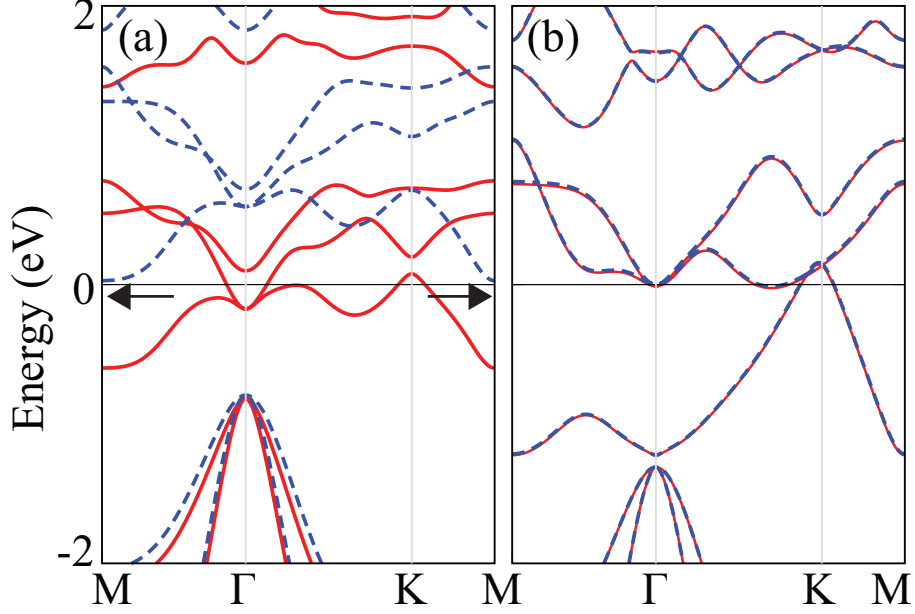


Figure 4.3. (Color online) The spin-polarized band structures of (a) TiSe<sub>2</sub>-1H and (b) TiSe<sub>2</sub>-2H monolayers. The  $E_F$  is at 0. The red and blue dashed curves represent spin-up and spin-down bands, respectively.

for the spin-polarized state, while contributions from Se 4*p* and H 1*s* orbitals are negligible. The variation of charge transfer between different atoms can be also important for the magnetism in the TiSe<sub>2</sub>-1H structure. According to Bader charge analysis, Ti atom loses 1.3 *e*, while H gains 0.1 *e*; as for Se, the one with H bonding gains about 0.5 *e*, while the one without H bonding gains about 0.7 *e*. Similarly, for the case of TiSe<sub>2</sub>-2H, Ti atom loses 1.2 *e*, while H atoms gain 0.1 *e*, and every H-bonded Se atoms gain 0.5 *e*. Moreover, a stable ferromagnetic state with high Curie temperature ( $T_c$ ) is necessary for the real full potential of spintronic devices. To this end, we further examine the preferred magnetic coupling of the TiSe<sub>2</sub>-1H monolayer. We use the  $2 \times 2$  cell as shown in Fig. for two different magnetic configurations. The energy difference between the antiferromagnetic (AFM) and ferromagnetic (FM) states which give the exchange energy ( $E_{ex}$ ), is calculated as  $E_{ex}=(E_{AFM}-E_{FM})/4$ . The calculated  $E_{xc}$  value is positive and found to be 32 meV, which satisfies the TiSe<sub>2</sub>-1H has FM ground state because the FM state has lower energy than the AFM state. In particular, Ising theory and Heisenberg model can be approximated Curie temperature of the materials. Based on the Ising model, the magnetic coupling of Hamiltonian can be written as;  $H = -\sum_{i,j} J_{ij} \hat{m}_i \hat{m}_j$ , where *J* is the Heisenberg exchange parameter and  $\hat{m}_i/\hat{m}_j$  represent the magnetic moment of the nearest neighbor-



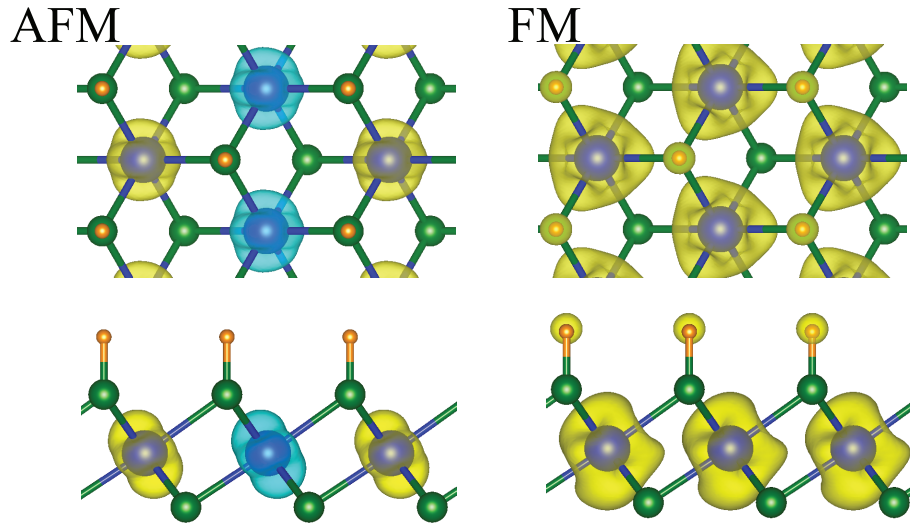


Figure 4.4. (Color online) The spin charge density difference of  $\text{TiSe}_2\text{-1H}$  structures top and side views, for the antiferromagnetic (AFM) and ferromagnetic (FM) states where yellow (blue) colors represent the majority (minority) spin states. The spin charge density difference is plotted at same isosurface value of  $0.003 \text{ e}/\text{\AA}^3$ .

unitcells. Details of the method (Kudrnovský et al., 2004) and different methodologies can be found previous studies (Torun et al., 2015; Kan et al., 2013) After all, using the mean field theory and the Heisenberg model to estimate the  $T_c$  from  $k_B T_c = (2/3) E_{ex}$ , which gives 248 K. The result reveal that  $\text{TiSe}_2\text{-1H}$  can be new magnetic materials to used in spintronics.

#### 4.5. Hydrogenated $\text{TiSe}_2$ Monolayers on $\text{HfX}_2$

Finally, we also perform an analysis of the electronic and magnetic properties for the one-side and both of its sides hydrogenated  $\text{TiSe}_2$  monolayers on different substrates. Among the possible choices, the  $\text{HfSe}_2$  and  $\text{HfS}_2$  which have semiconducting property, are chosen. The reason is that  $\text{HfX}_2$  monolayers have several characteristics in common hydrogenated  $\text{TiSe}_2$ . Furthermore, Hf-based TMDs have predicted that large work functions and reasonable mobilities, making them suitable for a range of nanoelectronic and optoelectronic device applications (Yue et al., 2014). Both  $\text{HfSe}_2$  and  $\text{HfS}_2$  monolayers are in 1T phase likewise  $\text{TiSe}_2$  and the optimizing lattice constants are 3.72 and 3.63 Å, which are very close to that of  $\text{TiSe}_2\text{-1H}$  and  $\text{TiSe}_2\text{-2H}$  structures. As shown in Fig. 4.5,

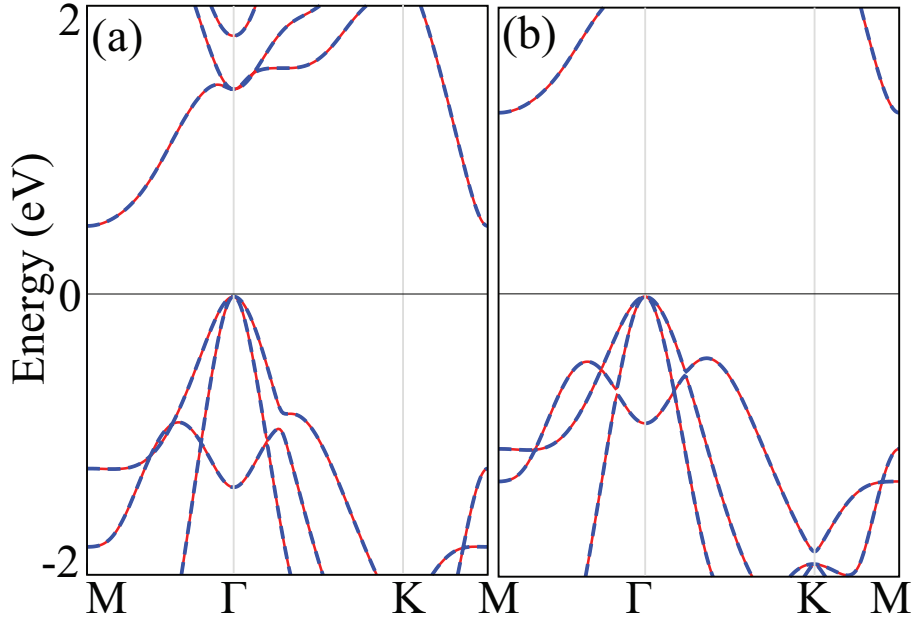


Figure 4.5. (Color online) The PBE band structures of (a) HfSe<sub>2</sub>, and (b) HfS<sub>2</sub> monolayers, where red curves are for spin-up while dashed blue curves are spin down. The  $E_F$  level is set to the valence band maximum.

the band-gap of the structures are found 0.47 and 1.26 eV for HfX<sub>2</sub> (X=Se, S), respectively. The band dispersions indicate that both monolayers are indirect band gaps and the electron effective masses are highly anisotropic similar to TiSe<sub>2</sub>-1H.

Since hydrogenated TiSe<sub>2</sub> monolayers have different lattice constants, we put TiSe<sub>2</sub>-1H on HfSe<sub>2</sub> and TiSe<sub>2</sub>-2H on HfS<sub>2</sub> monolayers. The heterostructures of them give the minimum total energy for TiSe<sub>2</sub>-1H on top of HfSe<sub>2</sub> monolayer (Fig. 4.6(a)), while for TiSe<sub>2</sub>-2H are shifted on HfS<sub>2</sub> monolayer such as the metal Ti atom is aligned on the top of sulfur atom, and the bottom H atom is on the metal atom Hf which is shown in Fig. 4.6(b).

The calculated lattice constant of TiSe<sub>2</sub>-1H/HfSe<sub>2</sub> heterostructure is found to be 3.70 Å and the layer-layer distance is 2.94 Å, with a binding energy is found to be 0.28 eV. The total magnetic moment of the system is 1.0  $\mu_B$ . Similarly, for the case of TiSe<sub>2</sub>-2H/HfS<sub>2</sub>, the lattice constant of the system is found to be 3.62 Å, and the layer-layer distance is 1.67 Å with the binding energy is about 0.40 eV, and zero net magnetic moment is found. The net magnetic moments of the hydrogenated structures in hetero form with HfX<sub>2</sub> are even same.

In addition, the electronic band structures of the systems are shown in Fig. 4.6.

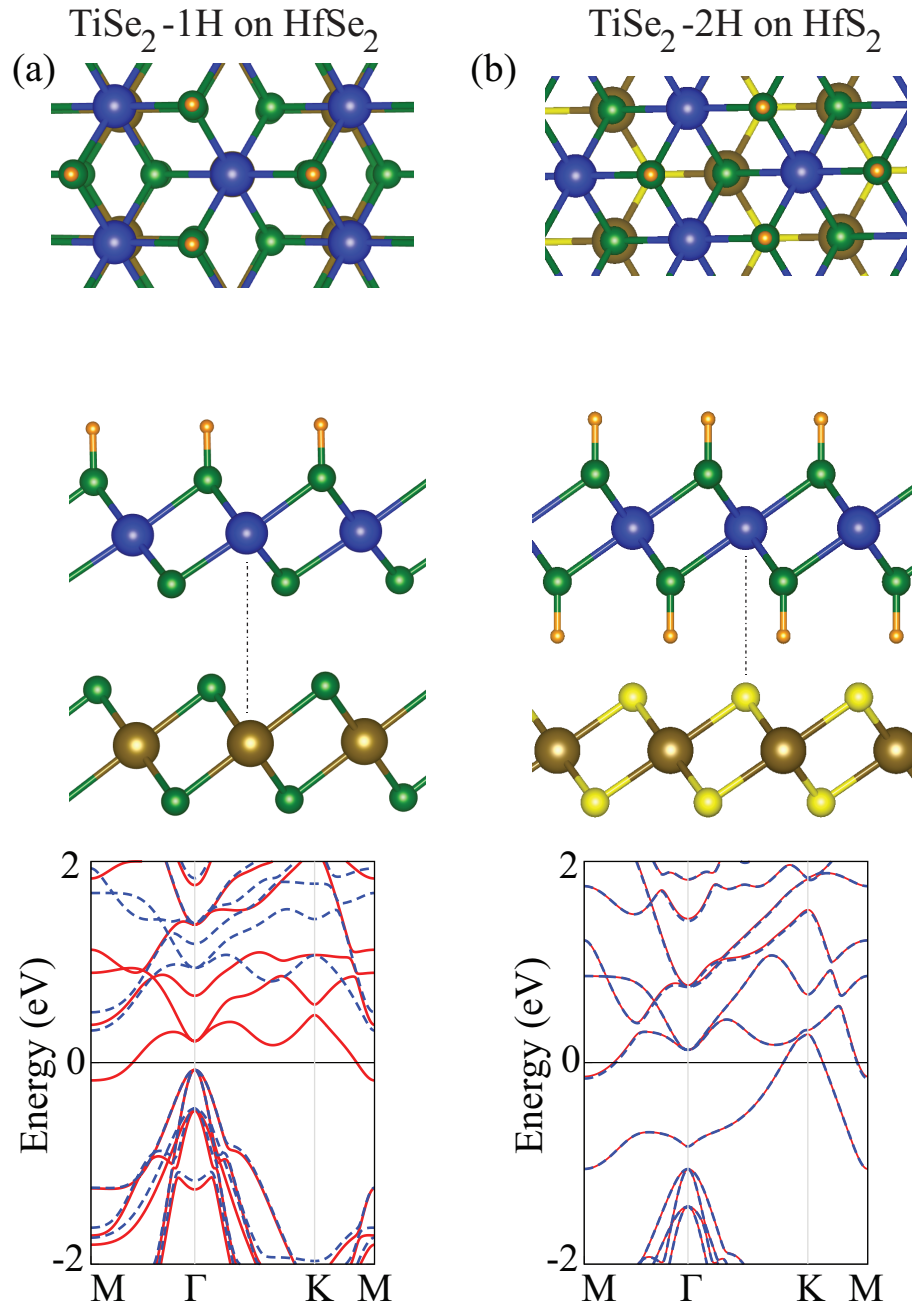


Figure 4.6. (Color online) Top and side views of hydrogenated monolayers on HfX<sub>2</sub> (X=Se, S). Their band structures are shown at the bottom of the figure, where the red and blue (dashed) curves represent spin-up and spin-down bands, respectively. The  $E_F$  is set 0 eV.

As in the case of  $\text{TiSe}_2$ -1H structure, semi hydrogenated monolayer preserve its half-metallicity behavior when it is on top of the  $\text{HfSe}_2$  monolayer. The only difference is that the spin-up and spin-down bands are shifted upward direction. Whereas, for the  $\text{TiSe}_2$ -2H structures on  $\text{HfS}_2$  monolayer, the electronic band property has minor changes. The metallic property is conserved, where the extra band cuts the Fermi level at very close to the M-point. This contribution comes from Hf atom due to the strong interaction between the  $\text{TiSe}_2$ -2H and  $\text{HfS}_2$  monolayers.

Our results demonstrate that the antiferromagnetic metallic ground state of  $\text{TiSe}_2$  can be tuned to become ferromagnetic and half-metallic by one-side hydrogenation, on the other hand, two-side hydrogenated  $\text{TiSe}_2$  exhibits antiferromagnetic metallic properties as its bare form. We have predicted that the ferromagnetic one-side hydrogenated  $\text{TiSe}_2$  has a Curie temperature  $T_c$  of 248 K. Its electronic band dispersion reveals that electron effective masses are highly anisotropic along the high-symmetry directions. Additionally, the structural and electronic properties of the hydrogenated monolayers on different substrates have also been investigated. The chosen  $\text{HfX}_2$  ( $X=\text{S}, \text{Se}$ ) substrates, which have semiconducting property and high electron mobilities so they are suitable for a range of nano-electronic and opto-electronic device applications, are well adapted to hydrogenated monolayers.

## CHAPTER 5

# ELECTRONIC AND MAGNETIC PROPERTIES OF ZIGZAG AND ARMCHAIR EDGED $\text{TiSe}_2$ AND $\text{PtSe}_2$ NANORIBBONS

The presence of exotic properties in 2D materials, that stemmed from increasing quantum confinement effects, has also motivated researchers to further reduce their dimension and to investigate one-dimensional (1D) nanoribbons (NRs). Commonly, one-dimensional nanostructures have been of both fundamental and technological interest due to interesting electronic and physical properties are intrinsically associated with their low dimensionality and quantum confinement effects. Therefore, the electronic and magnetic properties of graphene nanoribbons (GNRs) have been intensively studied (Son et al., 2006a; Han et al., 2007).

Motivated by the recent synthesis of single layer  $\text{TiSe}_2$ , in this chapter we investigate the structural and electronic properties of zigzag and armchair-edged nanoribbons of this material (Ozaydin et al., 2015). Similar to 1T- $\text{TiSe}_2$ , the epitaxial growth of high-quality single-crystal, monolayer platinum diselenide ( $\text{PtSe}_2$ ), a new member of TMDs family, by a single-step of a direct selenization of Pt(111) substrate is demonstrated (Wang et al., 2015). In addition, we also analyze the electronic properties of 1T phase of  $\text{PtSe}_2$  nanoribbons.

### 5.1. Computational Details

The PBE form of the GGA are adopted to describe the electron exchange and correlation for both spin-polarized and spin-unpolarized cases. In order to correct the PBE band structure for a monolayer of  $\text{TiSe}_2$  (also for  $\text{PtSe}_2$ ), we also use the Heyd-Scuseria-Ernzerhof 06 (HSE06) functional (Heyd et al., 2003, 2006) which is known to give better electronic structure description that is close to experiments and produce accurate band gaps. Since it improves the accuracy of standard band gaps, we determined HSE06 functional parameters as an enhanced fraction of the Hartree-Fock exchange  $\alpha = 0.25$  and screening  $0.2 \text{ \AA}^{-1}$ . The kinetic energy cutoff for the plane-wave expansion is set to 500

eV where the Brillouin Zone (BZ) was sampled with Monkhorst Pack (MP) by  $7 \times 1 \times 1$  k-point grids. For all band structure calculations, we use a  $75 \times 1 \times 1$   $\Gamma$ -centered k-point mesh. To avoid the interaction between periodic images, we ensured a sufficient large supercell which is  $20 \text{ \AA}$  long perpendicular to the nanoribbon plane and with an edge-to-edge distance of at least  $13 \text{ \AA}$ . At the same time, all the atoms in the supercell are fully relaxed during the geometry optimization. The convergence threshold for energy is chosen as  $10^{-5}$  eV and  $10^{-4}$  eV/ $\text{\AA}$  for the force. The charge distribution on the atoms are calculated by using the Bader analysis.

Moreover, we investigate hydrogen saturated nanoribbons in order to study the edge stability. The hydrogen saturation is realized by adding one hydrogen atom to the edge of Ti (Pt) and Se atoms for the zigzag nanoribbons, however for the armchair nanoribbons one hydrogen atom is added to the edge of Se atoms and two hydrogen atoms are added to the Ti (Pt) atom. For the determination of the most favorable structure (for the case of  $\text{TiSe}_2$  NRs) which means the structure after hydrogenation, the binding energies are estimated from:  $E_B = E_T[\text{NR}] + nE_T[\text{H}] - E_T[\text{NR} + n\text{H}]$  where  $E_T[\text{NR}]$  is the total energy of the  $\text{TiSe}_2$  nanoribbon,  $E_T[\text{H}]$  is the energy of the free hydrogen atom,  $E_T[\text{NR} + n\text{H}]$  is the total energy of the  $\text{TiSe}_2$  nanoribbon saturated by hydrogen atoms, and  $n$  is the total number of saturated hydrogen atoms.

## 5.2. Two-Dimensional Monolayer $\text{TiSe}_2$

Before a comprehensive investigation of  $\text{TiSe}_2$  nanoribbons, we first present the atomic, electronic and magnetic properties of the  $\text{TiSe}_2$  monolayer. Principally, layered structures of TMDs can form several different phases, *e.g.* H and T, that result in diverse electronic properties. Monolayer  $\text{TiSe}_2$  has a hexagonal crystal structure composed of three atom layers with a metal atom Ti layer sandwiched between two chalcogen Se layers. Here octahedral coordination of the metal atoms results in the 1T structure as shown in Fig. 5.1(a). Similar to graphite and graphene, in bulk  $\text{TiSe}_2$  the monolayers are bound together through the interlayer van der Waals (vdW) interaction. The bond lengths are uniformly  $d_{\text{Ti-Se}} = 2.56 \text{ \AA}$ ,  $d_{\text{Se-Se}} = 3.72 \text{ \AA}$ , where the angle between the Ti-Se bonds is  $\theta_{\text{Se-Ti-Se}} = 93.12^\circ$  and the optimized lattice constant is  $3.52 \text{ \AA}$  from PBE calculation.

The PBE electronic band dispersion, shown in Fig. 5.1(b), shows that single layer  $\text{TiSe}_2$  is a metal with a nonmagnetic ground state. In addition, the partial density of states (PDOS) reveals that while there is negligible contribution from the Se orbitals around the Fermi level ( $E_F$ ), those bands are mainly composed of Ti-3d orbitals ( $d_{z^2}$ ,  $d_{xy}$ ,  $d_{yz}$ ).

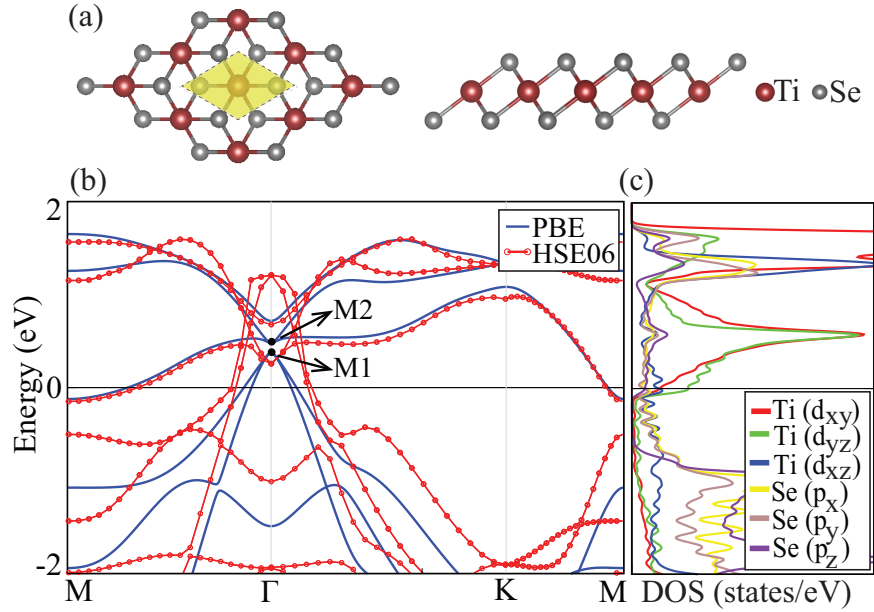


Figure 5.1. (Color online) (a) Atomic structure of monolayer 1T-TiSe<sub>2</sub> with top and side views where the dashed yellow area denotes the unitcell of the monolayer, and (b) the band structure calculated with PBE and HSE06, (c) partial density of states as calculated with PBE. Labels M1 and M2 are discussed in Fig. 5.6.

At the same time, a Bader analysis indicates that each Ti atom gives 1.4 electrons to the Se atoms which means that 0.7 electrons are taken by one Se atom, hence this situation shows that the character of the bonding is ionic. In contrast, the band structure of 1T TiS<sub>2</sub> is semiconducting. Usually the difference in chalcogen atoms affects the structural properties, but has little influence on the electronic properties. For instance single layers of MoSe<sub>2</sub> and MoS<sub>2</sub> are both direct band gap semiconductors. However, a TiSe<sub>2</sub> sheet exhibits a metallic behavior with a low band crossing of the Fermi level, which is different from TiS<sub>2</sub>.

To further examine the electronic properties of 1T-TiSe<sub>2</sub>, we also calculated the band structure with the HSE06 method which is shown in Fig. 5.1(b). As can be seen the calculated bands below the Fermi level are shifted upward while above the Fermi level they are slightly shifted downward. At the same time, below the Fermi level the bands are decomposed but the bands above the Fermi level almost overlap with those of the PBE result. Consequently, from both the PBE and HSE06 methods we may conclude that TiSe<sub>2</sub> is metallic.

In general, relative to the experimental values, band gaps of semiconducting mate-

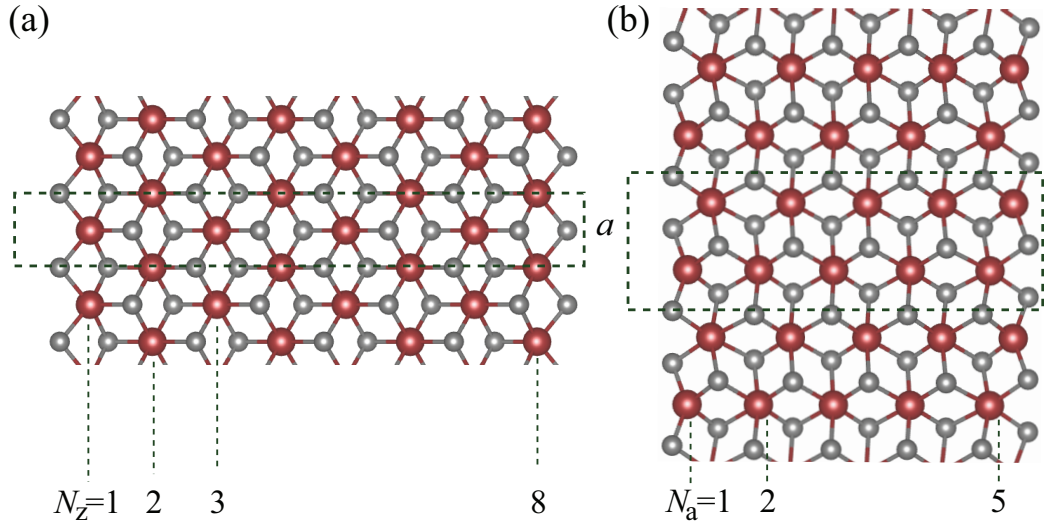


Figure 5.2. (Color online) Top view of (a) zigzag and (b) armchair TiSe<sub>2</sub> nanoribbons. The unitcell is indicated by the dashed box.

rials are underestimated by PBE, but they are overestimated when HSE06 corrections are added. However, PBE+HSE06 provides better agreement with the experimental values. Applying HSE06 corrections to metallic systems is not very common due to its computational cost, and no expected qualitative change in the band structures. Its effect is to introduce some shifts to the bands but the metallic character is preserved. For instance, single-layered VS<sub>2</sub> and T-MoS<sub>2</sub> are still found metallic with HSE06 correction.

### 5.3. Nanoribbons of 1T-TiSe<sub>2</sub>

The TiSe<sub>2</sub> nanoribbons (TiSe<sub>2</sub>-NRs) are obtained by cutting the 2D-TiSe<sub>2</sub> monolayer. According to the different directions of termination, there are two kinds of nanoribbons: zigzag (TiSe<sub>2</sub>-ZNR), and armchair (TiSe<sub>2</sub>-ANR). Apart from the termination, TiSe<sub>2</sub>-NRs are defined by their widths. The width of the zigzag nanoribbon is denoted as  $N_z$  (TiSe<sub>2</sub>- $N_z$ ZNR) and for armchair nanoribbon, the width is denoted by  $N_a$  (TiSe<sub>2</sub>- $N_a$ ANR). In Fig. 5.2 the lattice structure of TiSe<sub>2</sub>-8ZNR and TiSe<sub>2</sub>-5ANR are presented. In our calculations, we consider width  $N_z$  from 2 to 10 and  $N_a$  from 2 to 8.

The fully optimized NRs exhibit structural deviation at the edges. For example TiSe<sub>2</sub>-ANRs are strongly distorted after relaxation, compared to TiSe<sub>2</sub>-ZNRs. In the triple layer networks, the edge selenium atoms shift their position from the Se layers to the Ti



layer for both zigzag and armchair nanoribbons whereas the Ti atoms at the edges shift their position from the Ti layer to the Se layers for only zigzag nanoribbons. At one of the edges the Ti atom is closer to the lower Se layer, and the Ti atom at the other edge is closer to the upper Se layer. As seen in Fig. 5.2(b) for armchair nanoribbons reconstruction takes place, as the Ti atoms at the edges moved towards the ribbon's center and the Se atoms tend to shift slightly outward. For  $\text{TiSe}_2$ -8ZNR, shown in Fig. 5.2(a), the Ti atoms moved slightly out of the plane, leading to a change of the Ti-Se bond length along the ribbon-axis. Nevertheless, the triple-layer networks are well kept intact for both ribbons. For instance, the average Ti-Se bond lengths for  $\text{TiSe}_2$ -7ZNR are 2.56 Å in the inner site, and 2.44 Å at the two edges. The angle between Se-Ti-Se bond is 6.22° between the center and edge of the  $N_z=7$  zigzag nanoribbon. For the  $\text{TiSe}_2$ -8ANR, coordination of atoms are different so that the Ti-Se bond length is different with values of 2.50, 2.57, and 2.64 Å in the inner site, at the edges it decreases to 2.38 Å. All of the nanoribbons display the same structural property, and the only difference is that the bond lengths between the edge Ti-Se atoms are longer in ZNRs than those in ANRs. Similar to the case of  $\text{MoS}_2$  nanoribbons(Li et al., 2008), at the edges the Ti-Se bond lengths decrease because of the irregular force on the edge atoms. Also, a Bader charge analysis tells us that charges on both Ti and Se atoms are equally distributed along the ribbon axis, since all of the Ti atoms lose the same amount of electron charge which is taken by the Se atoms. Likewise in the 2D- $\text{TiSe}_2$  layer, every Ti atom loses 1.4 electrons to the Se atoms which gain 0.7 electrons along the ribbon axis.

### 5.3.1. Electronic Properties

During the geometry optimization, we first carried out both spin-polarized and spin-unpolarized total energy calculations in order to determine the ground state of the different  $\text{TiSe}_2$ - $N_z$ ZNR ( $\text{TiSe}_2$ - $N_a$ ANR). There is no energy difference between spin-polarized and spin-unpolarized calculations which indicates that zigzag and armchair  $\text{TiSe}_2$  nanoribbons have a nonmagnetic ground state. To be more confident about the magnetization of the edges, we also performed calculations for four different magnetic orderings for  $\text{TiSe}_2$ -4ZNR and also  $\text{TiSe}_2$ -5ZNR by taking a double unitcell, such as antiferromagnetic (AFM), ferromagnetic (FM) (where, the atoms are located at different edges are AFM coupled, and at the same edge are FM coupled) (see Fig. 5.4(a)). We take the case of a  $\text{TiSe}_2$ -5ZNR as an example. Calculations starting from the four magnetic states, namely AFM-AFM, AFM-FM, FM-AFM, and FM-FM, and results in the same total energy. The

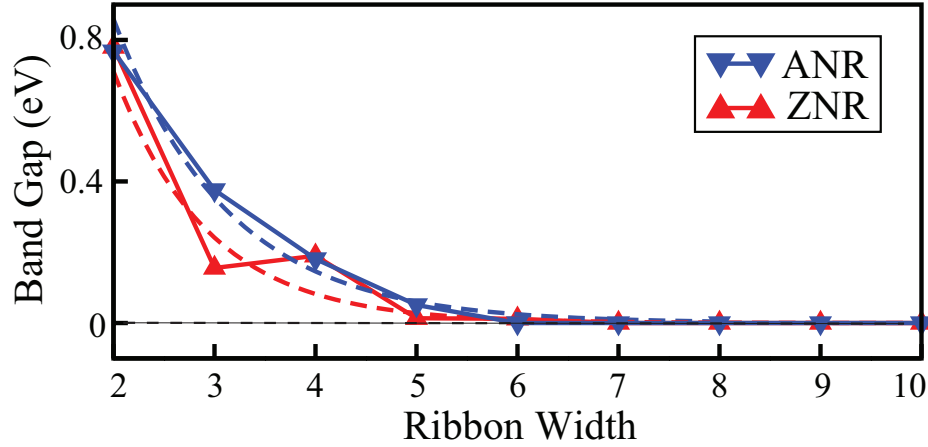


Figure 5.3. (Color online) Energy gap of zigzag ( $2 \leq N_z \leq 10$ ) and armchair ( $2 \leq N_a \leq 10$ ) 1T-TiSe<sub>2</sub> nanoribbons as function of the ribbon width. Dashed curves are exponential fits.

same magnetic test is also applied to armchair nanoribbons (see Fig. 5.4(b)). All the test results gave the same total energy and zero net magnetic moment. As a result, TiSe<sub>2</sub> armchair nanoribbons have a nonmagnetic ground state like MoS<sub>2</sub>-ANRs (Li et al., 2008). Thus, our calculation demonstrates that TiSe<sub>2</sub>-ZNRs and TiSe<sub>2</sub>-ANRs are not magnetic and the edge states do not effect the magnetization of the structures.

After analyzing the structural and magnetic properties, we investigated the band dispersion of the TiSe<sub>2</sub>-NRs. Electronic structures of TiSe<sub>2</sub>-NRs show similar behavior like the single-layer 1T-TiSe<sub>2</sub>. In fact, we found that reducing the dimensionality from 2D to 1D, at a certain ribbon width a metal to semiconductor transition is found for both zigzag and armchair nanoribbons as seen in Fig. 5.3. The band gap decays monotonically with the ribbon width for armchair nanoribbons, however for zigzag nanoribbons the rapid band gap decrease is superposed with an even-odd oscillation with increasing  $N_z$  and finally both structures switches to the zero energy gap of monolayer TiSe<sub>2</sub> (for  $N_z \geq 7$ , and  $N_a \geq 6$ ). Similar oscillatory behavior is also observed in the equilibrium lattice constant for TiSe<sub>2</sub>- $N_z$ ZNRs, when we increase the ribbon width  $N_z$ , the lattice constant approached slowly the value 3.52Å which is the same as that calculated for the 2D-TiSe<sub>2</sub>. The edge reconstructions are more effective in changing the equilibrium lattice constant of ultra narrow ribbons.

As illustrated in Fig. 5.3, the band gaps as a function of ribbon width for both

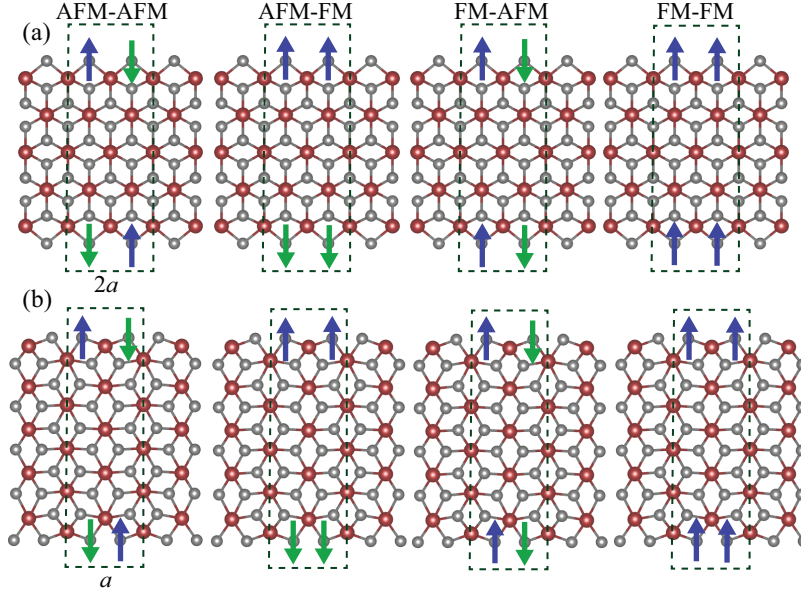


Figure 5.4. (Color online) Different magnetic interaction cases for (a)  $\text{TiSe}_2$ -5ZNR and (b)  $\text{TiSe}_2$ -5ANR.

zigzag and armchair-edged nanoribbons decay very rapidly, except for a small superposed oscillation observed in ultranarrow zigzag nanoribbons. Similar band gap oscillations as a function of ribbon width were also predicted for other semiconducting nanoribbons (Son et al., 2006b). Nevertheless, due to the rapid decay in both types of nanoribbons, to provide a quantitative measure for these decays the band gap variations are fitted to the exponential functions,  $E_{gap}(N) = \alpha \exp(-N\beta)$ , where  $N$  is the width of the nanoribbon (for ZNRs  $N=N_z$  and for ANRs  $N=N_a$ ), and  $\alpha$  and  $\beta$  are fitting parameters. For armchair and zigzag nanoribbons, the values of the fitting parameters are found to be  $\alpha=5.06$ ,  $\beta=0.89$  eV and  $\alpha=6.17$ ,  $\beta=1.08$  eV, respectively. For  $N \geq 7$ , the band gaps of both types of nanoribbons are vanished.

Spin-unpolarized band structures of  $\text{TiSe}_2$ - $N_z$ ZNRs are presented in Fig. 5.5. Notice that the band structures show similar property at the X-point for odd and even numbers of ribbon width. For the ribbon width of  $N_z=2$  a large gap of about 0.786 eV is found. Among the four ZNRs in Fig. 5.5,  $\text{TiSe}_2$ -4ZNR has the largest band gap of 0.201 eV,  $\text{TiSe}_2$ -3ZNR has a medium band gap of 0.165 eV,  $\text{TiSe}_2$ -5ZNR and  $\text{TiSe}_2$ -6ZNR have the smallest band gaps of 12 meV and 5 meV, respectively. Both the direct band gap of zigzag-edged and the indirect band gap of armchair-edged ultranarrow nanoribbons decrease with increasing ribbon width and eventually vanish for  $N_z \geq 7$ , and  $N_a \geq 6$ . The conduction band minimum (CBM) and the valance band maximum (VBM) cross resulting

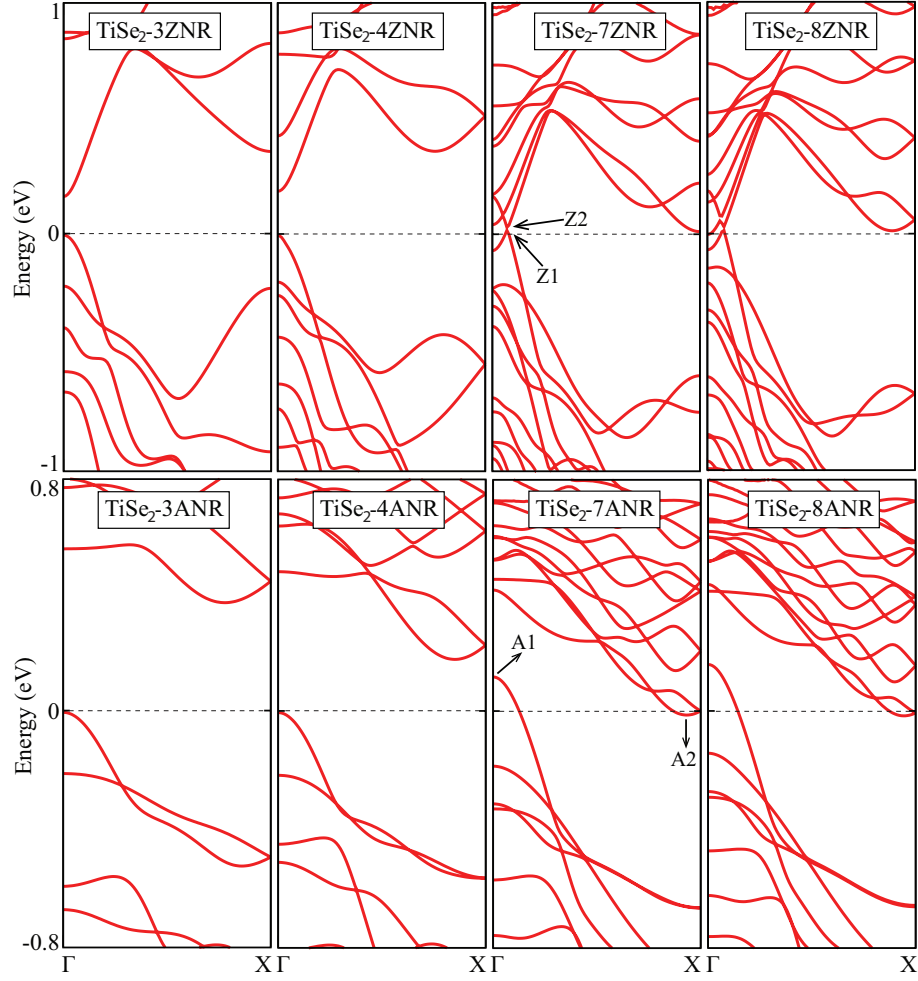


Figure 5.5. (Color online) Electronic band structure of a series of zigzag and armchair nanoribbons of 1T-TiSe<sub>2</sub> by using the PBE method.

in a semimetallic band structure with overlapping bands.

In order to investigate this width-dependent transition in the band structure, as well as the odd-even variations observed in the narrowest ZNRs, we have considered partial charge density (PCD) profiles corresponding to VBM and CBM, or for some specific pair of points in the band structures. These pair of points are M1 and M2 for 2D-TiSe<sub>2</sub> (Fig. 5.1), Z1 and Z2 for ZNRs, and A1 and A2 for ANRs (Fig. 5.5). The PCD plots of the VBM and the CBM as shown in Fig. 5.6 indicate the electronic states around the Fermi level. For TiSe<sub>2</sub>-3ZNR (TiSe<sub>2</sub>-4ZNR), the VBM and the CBM originate from a hybridized mixture of 3d electrons of Ti and 4p electrons of Se atoms with the hybridization being stronger in the VBM than that in the CBM. A comparison of the VBM states of TiSe<sub>2</sub>-3ZNR and TiSe<sub>2</sub>-4ZNR indicate that they are localized more at the edges for odd  $N_z$ ,

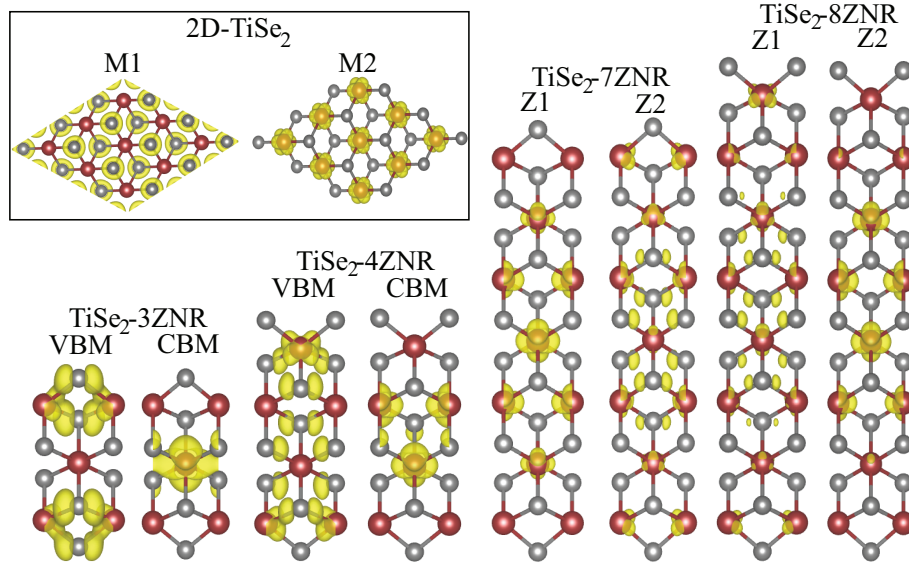


Figure 5.6. (Color online) Band decomposed charge density plots of monolayer and  $N_z=3,4,7,8$  nanoribbons of  $\text{TiSe}_2$  where Z1 and Z2 are shown in the band-structures (see Fig. 5.5). Inset shows the  $\Gamma$ -point charge densities of M1 and M2 band edges (shown in Fig. 5.1) of 2D  $\text{TiSe}_2$ .

whereas they are more uniform distributed for even  $N_z$  ribbons. For wider ribbons ( $N_z > 4$ ), both the VBM and CBM states tend to delocalize and the metallic character is attained (this is evident for  $N_z=7$  and  $N_z=8$  in Fig. 5.6). With increasing  $N_z$ , the PCD plots at the Z1 and Z2 points tend to converge to those at the M1 and M2 pair for 2D- $\text{TiSe}_2$ , where the corresponding states are localized on the Se and Ti atoms, respectively. The opening of a band gap in very narrow ribbons can be attributed to quantum size effects.

Typical band structures for a series of armchair  $\text{TiSe}_2$  nanoribbons are also shown in Fig. 5.5. Unlike zigzag nanoribbons, the electronic structure of the armchair ribbons exhibit an indirect band gap for  $N_a \leq 6$ . The gap decreases exponentially with the ribbon width. The band gap is almost halved when the ribbon width is increased from  $N_a=2$  to  $N_a=4$ .  $\text{TiSe}_2$ -5ANR still has a band gap of about 5.2 meV. Starting with  $N_a=6$ , the CBM dips into the Fermi level, so that the armchair nanoribbons become metallic for wider widths. Some partial charge density plots for  $\text{TiSe}_2$ - $N_a$ ANRs are also illustrated in Fig. 5.7. Similarly, the VBM and CBM states are composed of a hybridized mixture of Ti-3d and Se-4p orbitals for small nanoribbons, however for the ribbon width larger than four, the hybridization becomes lost.

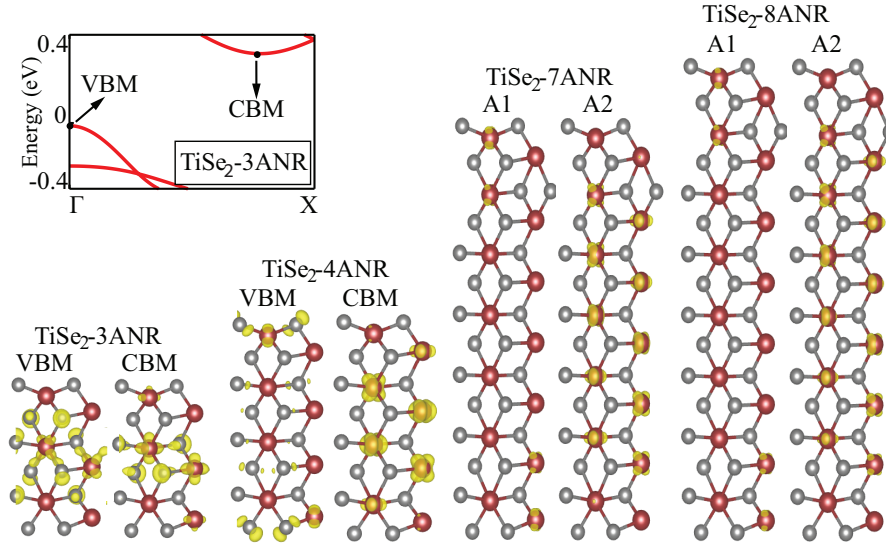


Figure 5.7. (Color online)  $\text{TiSe}_2$ -3ANR band structure and band decomposed charge densities of  $N_a=3,4,7,8$  nanoribbons of  $\text{TiSe}_2$  where the A1 and A2 refer to the states indicated in Fig. 5.5.

#### 5.4. Hydrogen Termination of Edges

In order to investigate the effect of dangling states present at the edges of the nanoribbons, we have passivated the edge atoms by hydrogen atoms. These unsaturated bonds influence the electronic properties of the ribbons. Naturally these states do not exist in the infinite  $\text{TiSe}_2$  single layer, therefore reducing dimensionality from 2D to 1D it will be of importance control the dangling bonds. Earlier, it was shown for graphene nanoribbons that when the dangling bonds at the edges are passivated with hydrogen atoms the electronic and magnetic properties of the ribbons are modified.(Barone et al., 2006) Unlike graphene, the  $\text{TiSe}_2$ -NRs have two types of atoms at the edges so that both Ti and Se atoms have to be passivated by hydrogen atoms to compensate the edge states.

Among possible configurations for the edge termination with hydrogen atoms, the most energetically favorable structure is shown for the  $\text{TiSe}_2$ -4ZNR in Fig. 5.8. As seen in the figure where the edge atoms are passivated by hydrogen atoms symmetrically, hydrogenation of the nanoribbons also enhances the stability of the structures. After hydrogenation the ground state energies is lowered, and the binding energy is found to be 11.7 eV for the case of  $\text{TiSe}_2$ -4ZNR. The band structures for several hydrogenated ZNRs are shown in Fig. 5.9. The  $\text{TiSe}_2$ - $N_z$ ZNRs are all metallic except for  $N_z=4$ .

We performed a analysis for the armchair nanoribbons. In  $\text{TiSe}_2$ -3ANR, as an

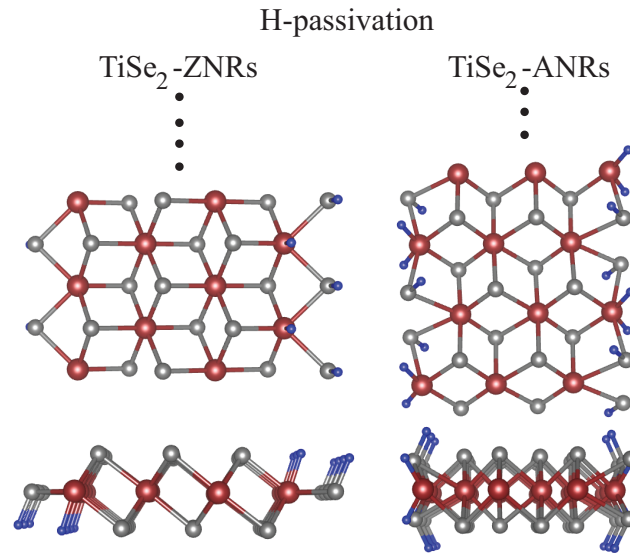


Figure 5.8. (Color online) Passivation of the edge states with hydrogen atoms (blue colored) for the zigzag and armchair nanoribbons.

example shown in Fig. 5.8, the edge Se and Ti atoms are passivated by one and two hydrogen atoms, respectively. The binding energy of the TiSe<sub>2</sub>-3ANR is 23.4 eV. After the hydrogenation, TiSe<sub>2</sub>-3ANR and TiSe<sub>2</sub>-4ANR are semiconductors with an increasing band gap. Also, the VBM state moves a little away from the  $\Gamma$ -point in case of  $N_a=3$ . TiSe<sub>2</sub>-7ANR and TiSe<sub>2</sub>-8ANR are still metallic after hydrogenation, however the overlap of the conduction and valance bands is reduced.

## 5.5. Pristine Single Layer and Nanoribbons of 1T-PtSe<sub>2</sub>

On the contrary the traditional sythesis method of MX<sub>2</sub> through exfoliation or chemical vapor deposition, Wang *et al.* (Wang et al., 2015) reported that the synthesis of PtSe<sub>2</sub> can be achieved via the direct deposition of Se atoms on a Pt substrate. Through angle-resolved photoemission spectroscopy (ARPES) measurements and band structure calculations confirm for the first time the semiconducting electronic structure of monolayer PtSe<sub>2</sub>, contrary to the semimetal properties of its bulk counterpart.

Our systematic study begins with calculating the electronic properties of PtSe<sub>2</sub> in its monolayer form. The optimized lattice constant is  $a=b= 3.696 \text{ \AA}$  (GGA+vdW), while the Se-Pt-Se bond angle is  $85.71^\circ$ . These values are in good agreement with previous theoretical calculations (Li et al., 2016) and also with the experimental ones of  $a=b= 3.70$

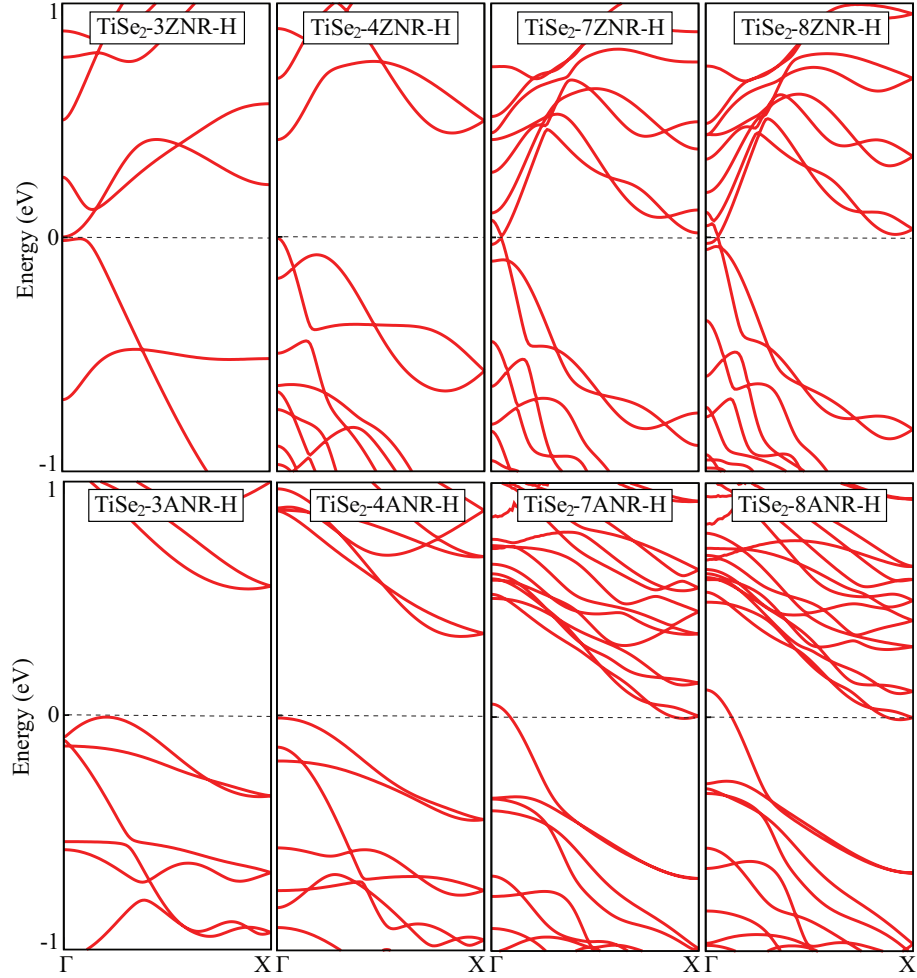


Figure 5.9. (Color online) Band structures for zigzag and armchair nanoribbons where the edge atoms are passivated by hydrogen atoms.

Å (Wang et al., 2015). As shown in Fig.5.10, monolayer PtSe<sub>2</sub> is a semiconductor with an indirect bandgap of 1.38 eV between the  $\Gamma$  point and a point half way along the  $\Gamma$ -M line. Our calculated bandgap is slightly smaller than previously predicted one of 1.41 eV (Zhuang and Hennig, 2013). Band structure for monolayer PtSe<sub>2</sub> calculated by HSE06 hybrid functional, shows the semiconductor nature of PtSe<sub>2</sub> monolayer with a value of 1.91 eV. At the same time, DOS reveals that valance band maksimum (VBM) ( $\Gamma$ -point) is mainly contributed by Se p orbitals and the coupling between the Pt d orbitals (mainly  $d_{xy}+d_{x^2}$ ) and Se p orbitals. Yet the conduction band minimum (CBM) (between  $\Gamma$ -M point) is mainly contributed by Pt  $d_{yz}+d_{xz}$  orbitals and, to less extent, by Se p orbitals and Pt  $d_{xy}+d_{x^2}$  orbitals. It is useful to say that, when increasing the thickness, bilayer PtSe<sub>2</sub> remains a semiconductor, but the energy gap decreases to 0.21 eV. Starting from a



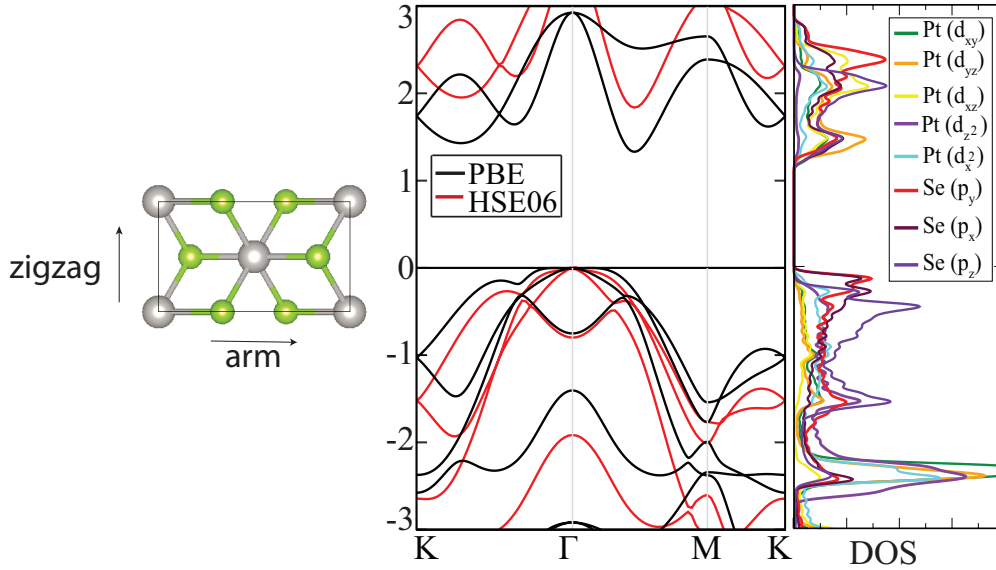


Figure 5.10. (Color online) Band structure and density of states (DOS) of monolayer PtSe<sub>2</sub>.

trilayer, PtSe<sub>2</sub> becomes semimetallic, therefore only monolayer PtSe<sub>2</sub> is a semiconductor with a sizable bandgap (Wang et al., 2015). The opening of a sizable bandgap within the range of visible light makes monolayer PtSe<sub>2</sub> potentially suitable for opto-electronics and photo-catalysis.

After we optimized the structure of a single PtSe<sub>2</sub> layer, two kinds of PtSe<sub>2</sub> nanoribbons can be distinguished according to the different directions of termination: zigzag and armchair. Following the previous convention used for TiSe<sub>2</sub> nanoribbons with armchair and zigzag shaped edges are classified by the number of Pt atoms across the ribbon width for the case of PtSe<sub>2</sub> NRs. After full relaxation, the triple-layer networks are well kept at both ribbons, only small structural deviations occur at the edges like TiSe<sub>2</sub> NRs as shown in Fig.5.2.

During the structure optimization, we have carried out both spin-unpolarized and spin-polarized computations to determine the ground state of PtSe<sub>2</sub> NRs. For both PtSe<sub>2</sub> ribbons, spin-polarized total energies are less favorable than spin-unpolarized ones, indicating that armchair and zigzag nanoribbons have a nonmagnetic ground states.

Fig.5.11 represents band structures for both armchair and zigzag nanoribbons of PtSe<sub>2</sub> in which the ribbon width changes  $4 \leq N_a(\text{or } N_z) \leq 9$ . The calculated band structures of the armchair and zigzag NRs clearly show that they are direct band gap semiconductors with band gaps of about 120 meV (about 80 meV for PtSe<sub>2</sub>-N<sub>z</sub>ZNRs). The gap are really

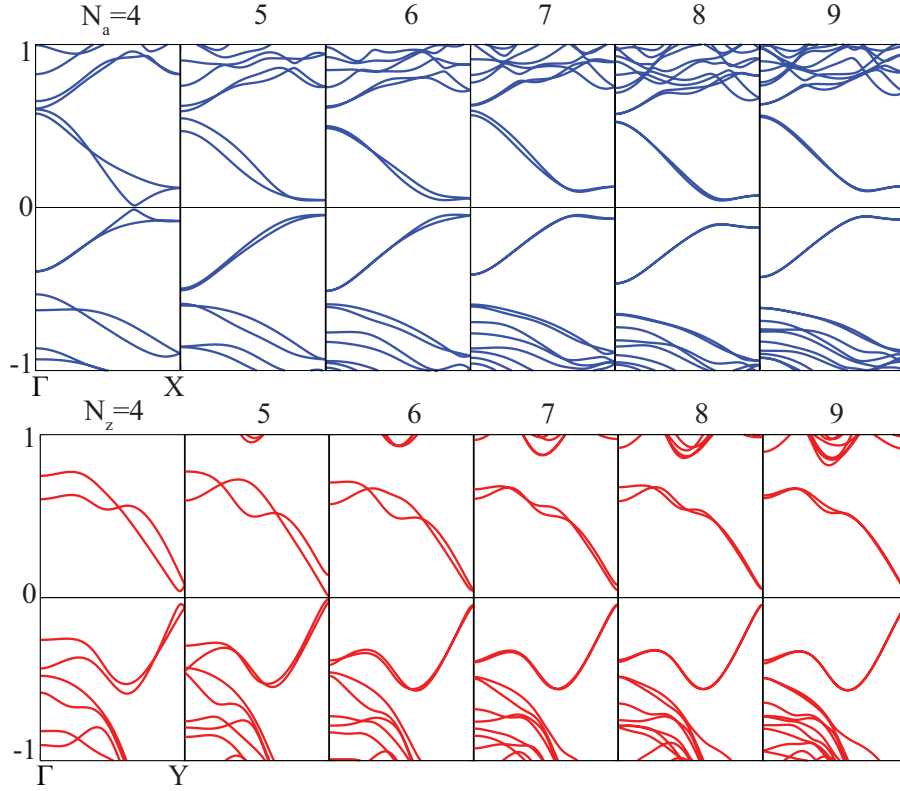


Figure 5.11. (Color online) Band structures for zigzag and armchair edged PtSe<sub>2</sub> nanoribbons.

small and almost width independent, because as it can be seen from Fig.5.11 increasing the ribbon width does not change the gap so much for both type of NRs. However, it is surprising that the both nanoribbons return to metallic when their width decrease to  $N_a=4$  for armchair and  $N_z=5$  for zigzag ribbon. When the edges of these ribbons are passivated by hydrogen atom, the ribbons return to semiconductor. Therefore, the hydrogenation process not only changes the magnetic property but also modulates the electronic property of the nanoribbons.

Generally, the introduction of hydrogen atoms to saturate the dangling states at the edges can improve the stabilities of the NRs and also can modulate the electronic and magnetic properties. Fig.5.12, represent typical band structure for PtSe<sub>2</sub>-7ZNR and PtSe<sub>2</sub>-7ANR, respectively. These band structures are all representative for the other hydrogenated zigzag and armchair PtSe<sub>2</sub> NRs.

The zigzag nanoribbons without hydrogen saturation have a small band gap. However, after hydrogenation of the edge atoms, it was found that PtSe<sub>2</sub>-7ZNR has an indirect band gap of about 1.17 eV. The minority and majority spin band are fully degenerate and

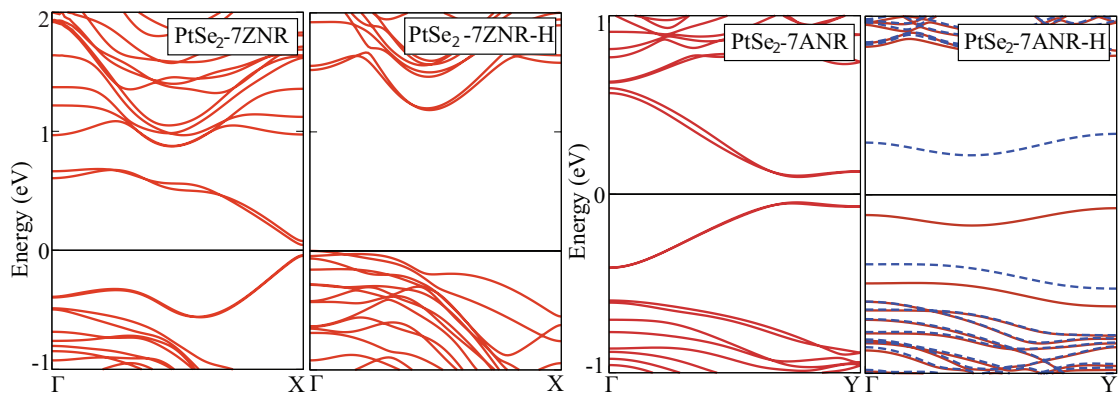


Figure 5.12. (Color online) Band structures of  $\text{PtSe}_2$ -7ZNR and the hydrogenated  $\text{PtSe}_2$ -7ZNR-H (and right side for the similar case of armchair nanoribbons.) The red solid and blue dashed lines are showed the spin-up and spin-down channels, respectively.

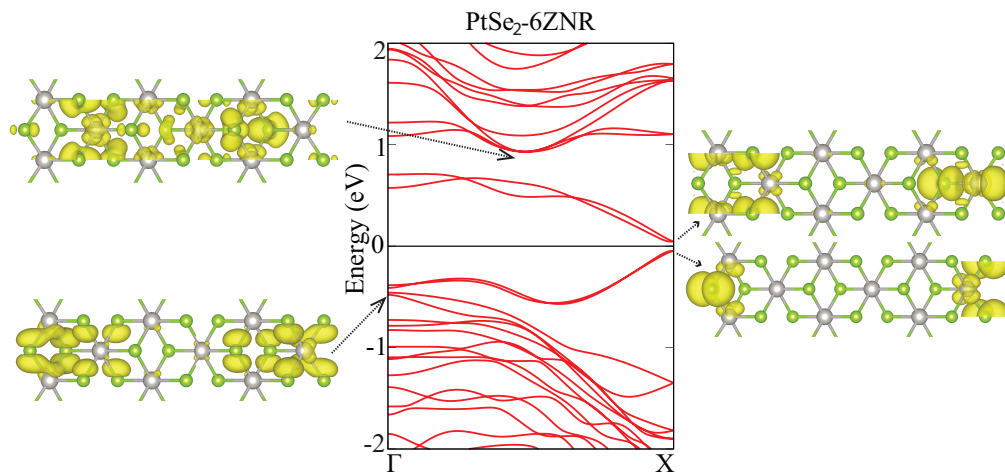


Figure 5.13. (Color online) Band structures for zigzag and armchair edged  $\text{PtSe}_2$  nanoribbons.

therefore the system is nonmagnetic. The partial charge density of states (as shown in Fig.5.13) reveals that the valance band top states are dominated by the p electrons of Se atoms at the edges and the small contribution from Pt-d electrons, while the d electrons from the Pt atoms at the edges mainly contribute to the conduction band bottom. Furthermore, the state below the valance band top is mainly located at the edges, but the the state above the conduction band bottom is uniformly distributed along the ribbon side. Since hydrogenation removes the effect of dangling bonds at the edges and the states around the fermi level are disappeared and the band gaps of the zigzag nanoribbons are increased. Similar to zigzag NRs, the dispersion relation for the case of armchair nanoribbons show that (Fig.5.13) semiconducting property. The only difference is that the majority and minority spin channels are split and the structure become ferromagnetic. For example, the total magnetic moment of PtSe<sub>2</sub>-7ANR increases from 0  $\mu_B$  to 1  $\mu_B$  due to the hydrogen termination. Hydrogen termination induce the magnetism of armchair PtSe<sub>2</sub> nanoribbons since the edge atoms do not recover the same state as that of inner atoms due to the H termination. As shown in Fig.5.14 for the case of PtSe<sub>2</sub>-6ANR is representative for all bare PtSe<sub>2</sub>-ANRs, the states around the fermi level are both dominated by the Pt-d and Se-p orbitals. However, their conduction band bottoms are shifted upward and valance band top are shifted downward directions due to the termination of the dangling states at the edges, resulting in an increase of their band gaps.

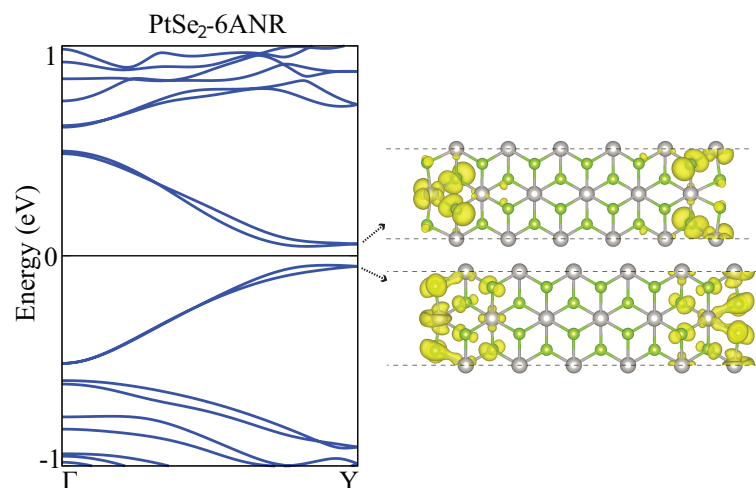


Figure 5.14. (Color online) Band structures for zigzag and armchair edged PtSe<sub>2</sub> nanoribbons.

Our analysis reveals that, differing from ribbons of other ultra-thin materials such as graphene,  $\text{TiSe}_2$  nanoribbons have some distinctive properties. The electronic band gap of the nanoribbons decreases exponentially with the width and vanishes for ribbons wider than 20 Angstroms. For ultranarrow zigzag-edged nanoribbons we find odd-even oscillations in the band gap width, although their band structures show similar features. Moreover, our detailed magnetic-ground-state analysis reveals that zigzag and armchair edged ribbons have nonmagnetic ground states. Passivating the dangling bonds with hydrogen at the edges of the structures influences the band dispersion. For the  $\text{PtSe}_2$  NRs, we found that both armchair and zigzag-edged nanoribbons have almost width-independent ultranarrow band gap. Furthermore, the  $\text{PtSe}_2$  NRs have either armchair and zigzag shaped edges on both sides with hydrogen passivation. Both varieties of ribbons are shown to have band gaps. This differs from the results of bare  $\text{PtSe}_2$  and  $\text{TiSe}_2$  nanoribbons. Our results shed light on the characteristic properties of T phase nanoribbons of similar crystal structures.

# CHAPTER 6

## WIDTH-INDEPENDENT BAND-GAP: $\text{TiS}_3$ NANORIBBONS

Similar to previous chapter, in this chapter we focus on nanoribbons form of transition metal chalcogenide that we investigate the electronic properties, mobility and strain response of transition metal tri-chalcogenide  $\text{TiS}_3$  (titanium tri-sulfide) nanoribbons from first-principles calculations (Kang et al., 2015). Several recent works have reported the synthesis of thin  $\text{TiS}_3$  films and few-layer of  $\text{TiS}_3$  nanoribbons which show a direct band gap of  $\sim 1.1$  eV (Ferrer et al., 2012, 2013). More importantly, the fabricated  $\text{TiS}_3$  NRs show ultrahigh photoresponse and fast switching times (Island et al., 2014). Most recently, 2D  $\text{TiS}_3$  nanosheets have been exfoliated its bulk crystal and implemented into field-effect transistors (Island et al., 2015). The electronic structure of single layer  $\text{TiS}_3$  was computed and indirect to direct band gap transition from bulk to monolayer was found (Dai and Zeng, 2015). The properties of defective monolayer  $\text{TiS}_3$  have also been studied (Iyikanat et al., 2015). Before further applying these materials in nanoelectronic and optical devices, a more comprehensive study from theoretical aspect is needed (Jin et al., 2015). Although there are a few theoretical investigations on the electronic properties of two-dimensional  $\text{TiS}_3$ , (Dai and Zeng, 2015; Jin et al., 2015) the characteristic properties of one-dimensional nanoscale structures of  $\text{TiS}_3$  ( $\text{TiS}_3$  NRs) have not been explored. Therefore, our study addresses some important questions on this novel material:

- (i) Do  $\text{TiS}_3$  NRs show chirality-dependent electronic and magnetic properties like graphene (Son et al., 2006a) and  $\text{MoS}_2$  NRs (Li et al., 2008)?
- (ii) Does quantum confinement in one-dimension result in a width-dependent electronic band gap of  $\text{TiS}_3$  NRs as in NRs of graphene (Son et al., 2006a), graphene (Şahin et al., 2010), silicene (Kim et al., 2012), and phosphorene (Tran and Yang, 2014)?
- (iii) What is the role of applied strain, which was shown to tune the electronic properties of chalcogenides (He et al., 2013; Johari and Shenoy, 2012), in the the properties of  $\text{TiS}_3$  NRs?
- (iv) Can the high electron mobility predicted for  $\text{TiS}_3$  (Dai and Zeng, 2015) be preserved in the NRs?

(v) How are the properties of  $\text{TiS}_3$  NRs affected by edge passivation?

The above-mentioned questions are answered in this chapter by using the state-of-the-art *ab-initio* calculations.

## 6.1. Computational Details

The generalized gradient approximation of Perdew-Burke-Ernzerhof (GGA-PBE) is adopted. The wavefunctions are expanded by plane-wave basis sets with a cutoff of 400 eV. Part of the calculations are also performed using the Heyd-Scuseria-Ernzerhof (HSE06) hybrid functional to get better band gap values. By mixing up the PBE and Hatree-Fock exchange functionals together, the HSE06 method reduces the localization and delocalization errors (Mori-Sánchez et al., 2008) of those functions, thus describe the band gap much better. The screen length of HSE06 is  $0.2 \text{ \AA}^{-1}$  and the mixing rate of Hatree-Fock (HF) exchange potential is 0.25. Brillouin zone sampling is performed with Monkhorst-Pack (MP) special k-point meshes including  $\Gamma$ -point. The k-grids for nanoribbons is either  $7 \times 1 \times 1$  or  $1 \times 11 \times 1$ , depending on the ribbon orientation, and for monolayer a  $7 \times 11 \times 1$  grid is used. The vacuum layer is larger than  $10 \text{ \AA}$  between two adjacent images. The convergence threshold for structure relaxation is  $0.01 \text{ eV/\AA}$ . The vacuum level is taken as zero reference to calculate the deformation potential.

## 6.2. Structural Properties and Edge Energetics

The monolayer of  $\text{TiS}_3$  has a rectangle unit cell which is composed of 2 Ti and 6 S atoms, with two lattice vectors  $a$  and  $b$ . Our optimized values for  $a$  and  $b$  are  $3.41 \text{ \AA}$  and  $5.02 \text{ \AA}$ , respectively, which are very close to the experimental bulk values ( $3.40 \text{ \AA}$  and  $4.96 \text{ \AA}$ ) (Brattas and Kjekshus, 1972) and other theoretical results ( $3.39 \text{ \AA}$  and  $4.98 \text{ \AA}$ ) (Jin et al., 2015). In the present work, two types of ribbons are studied, with their ribbon axis along  $a$  and  $b$  axis. The nanoribbons are indicated as  $N$ -**a**- $\text{TiS}_3$ NR and  $N$ -**b**- $\text{TiS}_3$ NR, where  $N$  stands for the number of Ti atoms in the unitcell of the ribbon, and **a**- $\text{TiS}_3$ NR and **b**- $\text{TiS}_3$ NR are along the  $a$  and  $b$  lattice vectors, respectively. Here we consider  $N=6-12$  for **a**- $\text{TiS}_3$ NR and  $N=4-10$  for **b**- $\text{TiS}_3$ NR. Figs. 6.1(a) and (c) show the structure of 8-**a**- $\text{TiS}_3$ NR and 6-**b**- $\text{TiS}_3$ NR. In Figs. 6.1(b) and (d) variation of the edge energy with ribbon width is shown. The edge energy of a  $N$ - $\text{TiS}_3$  NR is defined as  $(E_{\text{NR}} - \frac{N}{2}E_{2\text{D}})/(2L)$ , where  $E_{\text{NR}}$  is the total energy of the ribbon unit cell,  $E_{2\text{D}}$  is the total energy of a primitive unit

Bond index	1	2	3	4	5
<b>8-a-TiS<sub>3</sub> NR</b>					
Bond length in ribbon (Å)	2.62	2.57	2.38	2.23	2.43
Bond length in monolayer (Å)	2.46	2.67	2.50	2.46	2.50
<b>6-b-TiS<sub>3</sub> NR</b>					
Bond length in ribbon (Å)	2.40	2.52	2.51	2.50	2.61
Bond length in monolayer (Å)	2.46	2.50	2.50	2.67	2.67

Table 6.1. The lengths of the edge bonds of a 8-**a**-TiS<sub>3</sub> NR and an 6-**b**-TiS<sub>3</sub> NR, and the corresponding values in a TiS<sub>3</sub> monolayer. The labels of bonds are shown in Fig. 6.1

cell of TiS<sub>3</sub> monolayer, and  $L$  is the lattice constant along the axis of the ribbon. The edge energy describes the energy cost to create a new edge from a monolayer. The edge energy of **a**-TiS<sub>3</sub>NRs oscillates with different ribbon width, and ranges from 454 meV/Å to 475 meV/Å. This is close to the values of many other TMC nanoribbons such as ribbons of MoS<sub>2</sub>, WS<sub>2</sub> and ZrS<sub>2</sub> (Güller et al., 2015). The situation in **b**-TiS<sub>3</sub>NRs is however much different, the edge energy is typically around 60 meV/Å, and slightly decreases as the ribbon width increases. Compared with the edge energies of graphene and many other TMC nanoribbons, which are in the order of 1 eV/Å, (Jun, 2008; Güller et al., 2015) **b**-TiS<sub>3</sub>NRs have much smaller edge energy, suggesting that formation of **b**-TiS<sub>3</sub>NRs from 2D TiS<sub>3</sub> can be much easier. In fact, the experimentally reported TiS<sub>3</sub> NRs are along the  $b$  direction (Island et al., 2014). The small edge energy of **b**-TiS<sub>3</sub>NRs can be attributed to the fact that the bonds along the  $a$  direction in 2D TiS<sub>3</sub> is much weaker than those along  $b$ , in accordance with the low in-plane stiffness (5.225 eV/Å<sup>2</sup>) along this direction.

In the TiS<sub>3</sub> NRs, there is no remarkable structural reconstruction, and the overall geometry of the monolayer is maintained. Due to the dangling bonds at the edge, the edge atoms undergo a structural relaxation. The lengths of the different bonds at the edges for the 8-**a**-TiS<sub>3</sub>NR and 6-**b**-TiS<sub>3</sub>NR are listed in Table 6.1. Compared with the case of monolayer, in 8-**a**-TiS<sub>3</sub>NR the length of bond 1 becomes larger, but the other bonds become shorter. In 6-**b**-TiS<sub>3</sub>NR, the length of bond 2 and 3 slightly increases, whereas the length of bond 1, 4, and 5 decreases significantly. Therefore, in general the bonds at the edge exhibit a contractive behavior. Apparently the dangling bonds that originate from the edge atoms result in compressive edge stress. For further understanding the reorganization of edge atoms we also calculate the edge stress of different TiS<sub>3</sub> NRs using the method in Ref. Jun, 2008. For **a**-TiS<sub>3</sub>NRs, the edge stress is in the range of 3.19-5.07



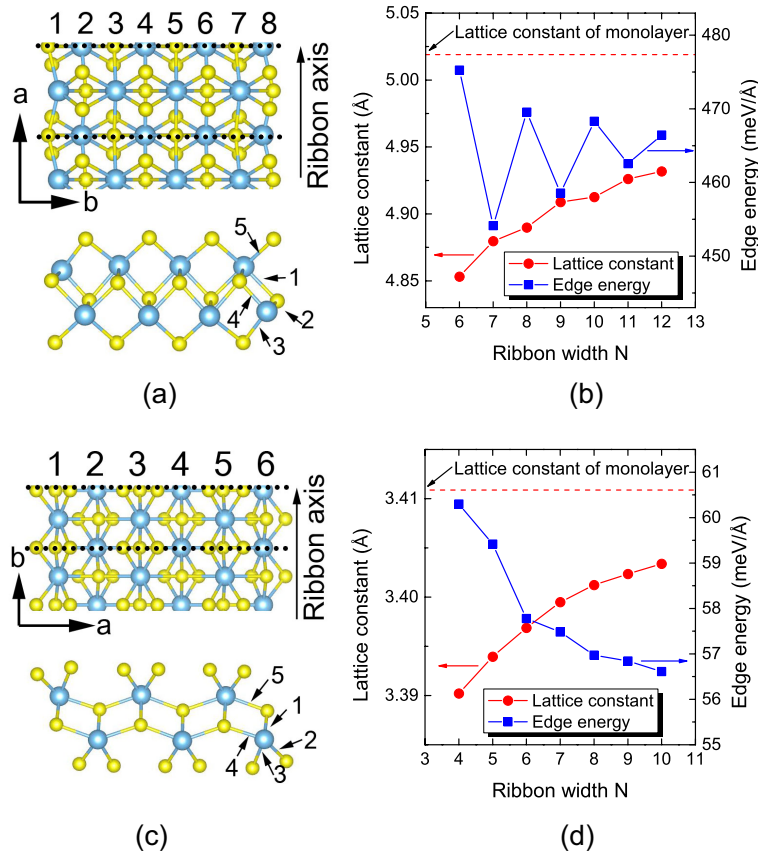


Figure 6.1. (Color online) (a) Top view and side view of an 8-**a**-TiS<sub>3</sub>NR. *a* and *b* are the lattice vectors of the 2D TiS<sub>3</sub>. The dashed lines indicate the unitcell of the 8-**a**-TiS<sub>3</sub>NR. The bonds at the edge are labeled by 1-5. (b) The lattice constant and edge energy of different **a**-TiS<sub>3</sub>NRs. The red dashed line indicates the lattice constant along *a* of the 2D TiS<sub>3</sub>. (c) The same as (a) but for a 6-**b**-TiS<sub>3</sub>NR. (d) The same as (b) but for 6-**b**-TiS<sub>3</sub>NRs.

eV/Å. For **b**-TiS<sub>3</sub>NRs, when *N* goes from 4 to 10, the edge stress decreases from 0.19 eV/Å to 0.17 eV/Å. The edge stress of **a**-TiS<sub>3</sub>NRs is much larger than that of **b**-TiS<sub>3</sub>NRs, which can be attributed to the larger bond contraction at the edges of **a**-TiS<sub>3</sub>NR. The compressive edge stress also reduces the lattice constants of the TiS<sub>3</sub> NRs. As seen in Figs. 6.1(b) and 6.1(d), the lattice constants of TiS<sub>3</sub> NRs are smaller than the value of the 2D monolayer. This behavior is more significant in **a**-TiS<sub>3</sub>NRs because of their larger edge stress. As the width of the ribbon increases, the lattice constant becomes closer to the one of 2D.

### 6.3. Width-Dependent Electronic Structure

We next study the electronic structure and width-dependent characteristics of **a**- and **b**-TiS<sub>3</sub>NRs. Our calculations reveal that all the **a**-TiS<sub>3</sub>NRs have metallic characters with non-zero density of states at the Fermi level. The electronic band dispersion of 10-**a**-TiS<sub>3</sub>NR, which is representative for all **a**-TiS<sub>3</sub>NRs, is shown in Fig. 6.2(a). It is seen from the figure that the metallic property stems from multiple up and down bands crossing the Fermi level at different points of the Brillouin Zone. Another feature of **a**-TiS<sub>3</sub>NRs is their magnetic ground state. We see that for various ribbon widths spin-polarization results in a net magnetic moment varying between 0.2  $\mu_B$  to 0.8  $\mu_B$  per unit cell. To get further insight on the spin-polarization in **a**-TiS<sub>3</sub>NR, we also calculate the spin density, which is the difference between up and down spin channels, for the 10-**a**-TiS<sub>3</sub>NR. As shown in Fig. 6.2(b), while the spin-polarized state mainly originates from the unpaired electrons of edge atoms, there is a small (ignorable) contribution from the Ti (S) atoms inside the ribbon.

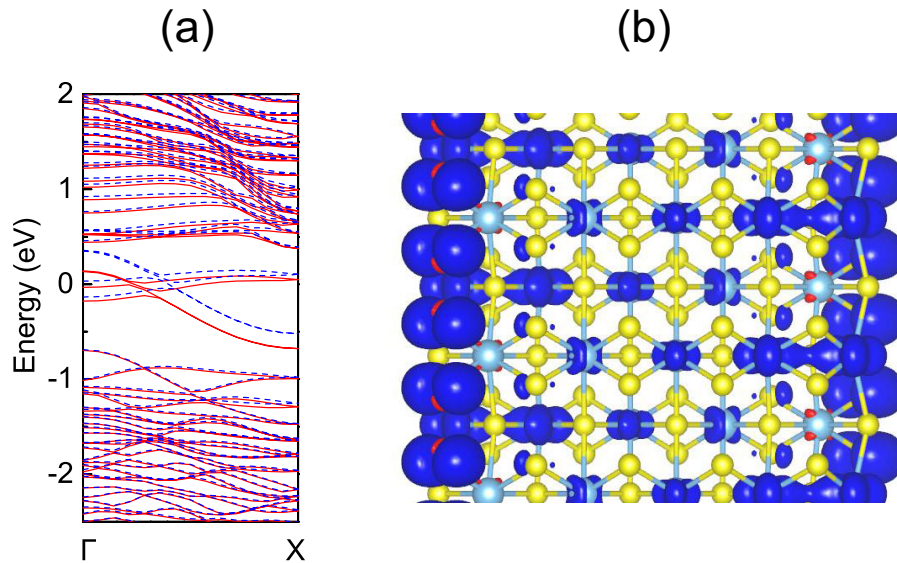


Figure 6.2. (Color online) (a) The band structures of a 10-**a**-TiS<sub>3</sub>NR obtained by GGA-PBE. Spin-up and spin-down channels are presented by red solid and blue dashed curves, respectively. The Fermi level is set to zero. (b) The magnetization charge density of the 10-**a**-TiS<sub>3</sub>NR.

In contrast to the **a**-TiS<sub>3</sub>NRs, all **b**-TiS<sub>3</sub>NRs are found to have a direct band gap located at the  $\Gamma$  point. In addition, magnetic structure analysis reveals that the **b**-TiS<sub>3</sub>NRs

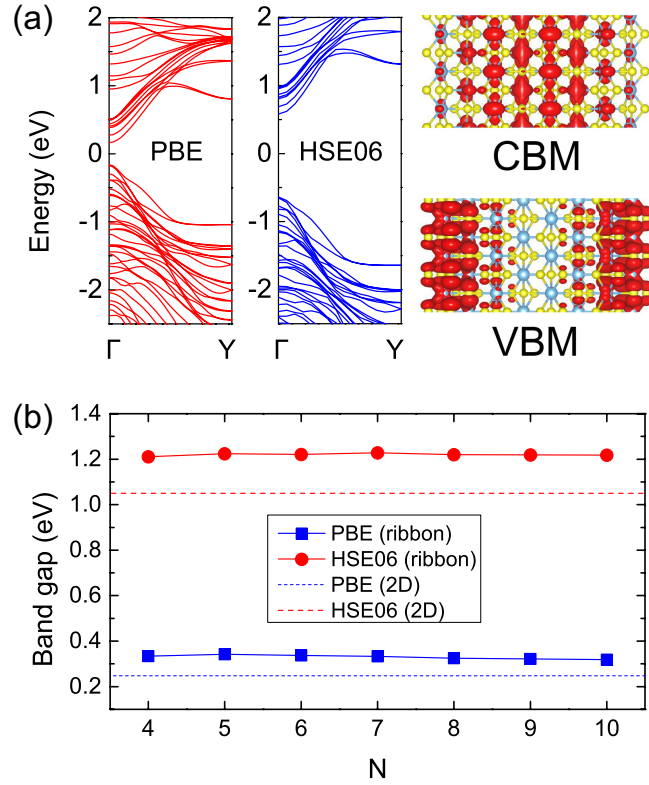


Figure 6.3. (Color online) (a) The band structures of an 8-**b**-TiS<sub>3</sub>NR obtained by GGA-PBE and HSE06, and the charge density of its CBM and VBM states. (b) The band gap as a function of the **b**-TiS<sub>3</sub>NR width  $N$ . Both GGA-PBE and HSE06 results are given. The dashed lines are the values for the 2D case.

have no ferromagnetic or anti-ferromagnetic order in their ground state and therefore they are non-magnetic semiconductors. In Fig. 6.3(a) a representative band structure of **b**-TiS<sub>3</sub>NRs (for 8-**b**-TiS<sub>3</sub>NR) is presented. It is seen that 8-**b**-TiS<sub>3</sub>NR have a band gap of 0.32 eV. However, the HSE06-approximated band gap value is 1.22 eV. It is well-known that although the band dispersions are almost the same in bare-GGA and HSE06 calculations, band gap values are underestimated by GGA exchange-correlation functionals. Therefore, we show band gap values of HSE06 together with GGA-PBE in Fig. 6.3. If not specified, the results in the following are from GGA-PBE. In Fig. 6.3(a), the charge densities of CBM and VBM states are plotted. The VBM state is localized at the edges, and mainly composed of S- $p_y$  orbital, together with some contribution from Ti  $d_{xy}$  and  $d_{yz}$  orbitals ( $x$  and  $y$  are along the transverse and axial directions of **b**-TiS<sub>3</sub> NRs, respectively, and  $z$  is perpendicular to the ribbon plane). On the other hand, the CBM state is distributed inside the ribbon and it mainly originates from Ti  $d_{x^2-y^2}$  and  $d_{z^2}$  orbitals.

Unique width dependence of the band gap values of **b**-TiS<sub>3</sub>NRs is illustrated in Fig. 6.3(b). Usually, due to the quantum confinement effect, the band gap of nanoribbons is strongly width dependent (Son et al., 2006a; Şahin et al., 2010; Kim et al., 2012; Tran and Yang, 2014). As the width  $W$  of the ribbon increases, the band gap will decrease and gradually approach the monolayer limit, and the typical decay behavior is  $1/W^\alpha$ . However, for **b**-TiS<sub>3</sub>NRs, it is interesting to note that the band gap is almost independent of the ribbon width. All **b**-TiS<sub>3</sub>NRs exhibit direct gaps around 0.32 eV (GGA-PBE) or 1.22 eV (HSE06). Furthermore, for  $N > 5$ , the positions of CBM and VBM states in different **b**-TiS<sub>3</sub>NRs are nearly the same, the difference is only a few meV. Therefore the band offset between ribbons of different widths is almost zero.

The reason for the width independent band gap can be explored by further analyzing the character of the VBM and CBM states. As shown in Fig. 6.3(a), the VBM states of **b**-TiS<sub>3</sub>NRs originate from the edge states and charge carriers are negligibly confined along the  $a$  direction, and hence the VBM energy has a weak width dependence. On the other hand, the CBM states are mainly composed of the inner region, hence are more "bulk-like" than the VBM states and can be affected by the quantum confinement effect. The strength of quantum confinement is inversely proportional to the effective mass. The electron effective mass of 2D TiS<sub>3</sub> along the  $a$  direction is quite large ( $1.52 m_0$ , see Table 6.2), indicating a quite flat conductive band along this direction. As a result, the confinement along the  $a$  direction only introduces minor changes of the CBM states. Therefore, both the position of VBM and CBM are not significantly affected by the confinement along  $a$ , leading to a width-independent band gap.

Synthesis of ribbons in laboratory conditions is always realized together with the formation of edge roughnesses which lead to undesired fluctuations in electronic properties of the structure. We see that for **b**-TiS<sub>3</sub>NRs, for a wide range of ribbon width, the band gap is almost constant and the band offset is negligible. Even with rough edges, the band gap of **b**-TiS<sub>3</sub>NR shows no spatial variation, also there is no transport barrier induced by a band offset. Such a property can facilitate the easy-integration of **b**-TiS<sub>3</sub>NRs in electronic devices. In addition, compared with monolayer case, the gaps of **b**-TiS<sub>3</sub>NRs are slightly larger. The gap value of 1.22 eV predicted by HSE06 is also good for adsorption of visible light, making **b**-TiS<sub>3</sub>NRs promising candidates for optoelectronic applications.

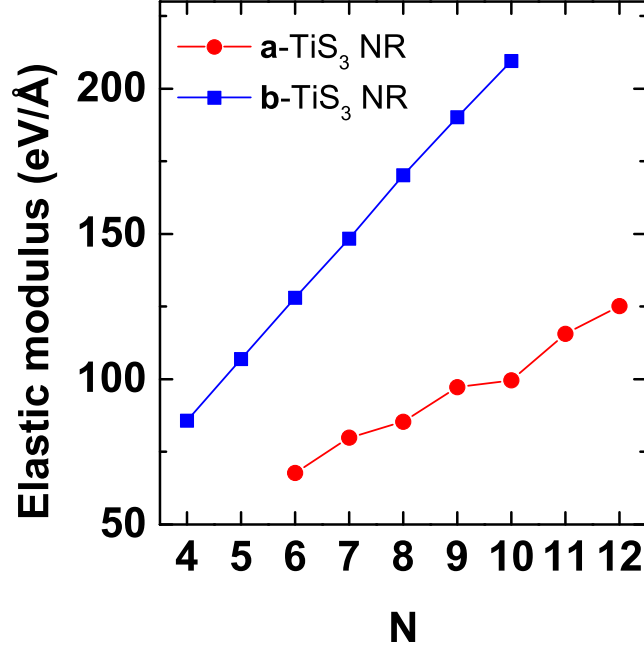


Figure 6.4. The calculated 1D elastic modulus for **a**-TiS<sub>3</sub>NRs and **b**-TiS<sub>3</sub>NRs, as function of the NR width.

### 6.3.1. Mechanical Properties and Response to Strain

The mechanical properties for 2D and 1D materials can be characterized by their elastic modulus  $C_{2D}$  and  $C_{1D}$ . For 2D system,  $C_{2D} = (1/S_0)(\partial^2 E / \partial \varepsilon^2)$ , where  $E$  is the total energy, and  $S_0$  is the equilibrium area. For 1D system,  $C_{1D} = (1/L)(\partial^2 E / \partial \varepsilon^2)$ , where  $L$  is the lattice constant. The calculated results for different TiS<sub>3</sub> NRs are shown in Fig. 6.4. The elastic modulus is found to scale linearly with the width. Moreover, with the same  $N$ , the width of an **a**-TiS<sub>3</sub>NR is larger than that of a **b**-TiS<sub>3</sub>NR, but the elastic modulus of the former is much smaller. Therefore, the strength of **a**-TiS<sub>3</sub>NRs is smaller than that of **b**-TiS<sub>3</sub>NRs. This is consistent with the smaller in-plane stiffness along the  $a$  direction in the TiS<sub>3</sub> monolayer (see Table 6.2).

Then we investigate the band structure response of **b**-TiS<sub>3</sub>NRs to strain  $\varepsilon$  by applying uniaxial tensile strain up to 10%. The variation of the band gap with strain is plotted in Fig. 6.5(a). Notice that the band gap of **b**-TiS<sub>3</sub>NRs monotonously increases with increasing strain. The response of **b**-TiS<sub>3</sub>NRs with different width is quite similar. The band gaps increase from  $\sim 0.3$  eV at  $\varepsilon = 0$  to  $\sim 0.9$  eV at  $\varepsilon = 10\%$ . Within the range of  $0 < \varepsilon < 4\%$ , the changes in the band gap of different ribbons are almost identical. Even

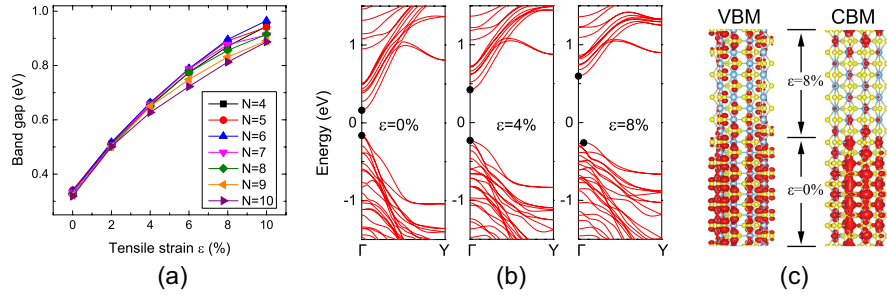


Figure 6.5. (Color online) (a) The band gap of **b**-TiS<sub>3</sub>NRs as function of tensile strain  $\epsilon$ . (b) The band structure of an 8-**b**-TiS<sub>3</sub>NR with  $\epsilon=0$ , 4% and 8%. The dots indicate the CBM and VBM states. (c) The CBM and VBM charge density of a 4-**b**-TiS<sub>3</sub>NR which is locally strained with 8%.

for  $\epsilon$  up to 10%, at each strain value, the maximum difference in band gap is less than 90 meV for  $N=4-10$ . The band gap of 4-**b**-TiS<sub>3</sub>NR is still direct at  $\Gamma$  in the strain range considered. In other **b**-TiS<sub>3</sub>NRs, a direct-to-indirect band gap transition is observed when strain is sufficiently large. The threshold strain value such a transition changes with the width of the ribbon. It is smaller in a wider ribbon. For example, the transition occurs at 10%, 6% and 4% for  $N=6$ , 8 and 10, respectively. Fig. 6.5(b) shows the band structure of an 8-**b**-TiS<sub>3</sub>NR with different strain. At  $\epsilon=4\%$ , the band gap is direct. When  $\epsilon$  is 8%, the VBM state moves a little away from the  $\Gamma$  point, while the CBM state remains at  $\Gamma$ , resulting in an indirect band gap. However, the direct gap at the  $\Gamma$  point is only 14 meV larger than the indirect gap. This is similar for other **b**-TiS<sub>3</sub>NRs. The difference between the direct and indirect gaps is very small, in the order of 10 meV. Also, the VBM state is still very close to the  $\Gamma$  point after the direct-indirect-band gap transition. Hence, all the **b**-TiS<sub>3</sub>NRs can be considered to have direct or quasi-direct band gap when tensile strain is applied.

The increase in band gap with increasing tensile strain is also consistent with the calculated deformation potential constant listed in Table 6.2. The deformation potential constant, which is the measure of the energy shift of the band edge states with respect to strain, is defined by  $dE_{edge}/d\epsilon$ , where  $E_{edge}$  is the band edge energy and  $\epsilon$  is the applied strain. For **b**-TiS<sub>3</sub>NRs, the deformation potential is positive for CBM, and negative for VBM. As a result, when tensile strain is applied, the CBM shifts upwards (energy increases), and the VBM shifts downwards (energy decreases), leading to a larger band gap. The calculated deformation potential also implies that the band alignment between unstrained and stretched **b**-TiS<sub>3</sub>NRs is type-I. When tensile strain is applied to a segment

	$m_h^*$ ( $m_0$ )	$m_e^*$ ( $m_0$ )	$E_v$ (eV)	$E_c$ (eV)	$C_{1D}$ (eV/Å)	$C_{2D}$ (eV/Å <sup>2</sup> )	$\mu_h$ ( $10^3 \text{ cm}^2\text{V}^{-1}\text{s}^{-1}$ )	$\mu_e$ ( $10^3 \text{ cm}^2\text{V}^{-1}\text{s}^{-1}$ )
monolayer (along $a$ )	0.308	1.523	3.882	0.740	-	5.225	0.831	0.935
monolayer (along $b$ )	0.998	0.381	-4.443	0.780	-	8.373	0.097	21.611
$N=4$	0.160	0.361	-7.969	1.339	85.788	-	0.168	1.751
$N=5$	0.163	0.362	-8.107	1.437	106.955	-	0.196	1.885
$N=6$	0.165	0.369	-8.134	1.485	128.059	-	0.229	2.057
$N=7$	0.204	0.370	-8.046	1.533	148.375	-	0.197	2.228
$N=8$	0.202	0.374	-8.224	1.386	170.233	-	0.219	3.092
$N=9$	0.204	0.373	-8.112	1.362	190.133	-	0.248	3.576
$N=10$	0.206	0.374	-8.200	1.311	209.585	-	0.264	4.222

Table 6.2. Calculated effective mass of hole ( $m_h^*$ ) and electron ( $m_e^*$ ), deformation potential constants for VBM ( $E_v$ ) and CBM ( $E_c$ ), elastic modulus ( $C_{1D}$  and  $C_{2D}$ ), and carrier mobility for hole and electron ( $\mu_h$  and  $\mu_e$ ) at 300 K for TiS<sub>3</sub> monolayer and the **b**-TiS<sub>3</sub> NRs.  $m_0$  is the mass of a free electron.

of a **b**-TiS<sub>3</sub>NR, a type-I band offset can be formed. The CBM (VBM) of the strained region will be higher (lower) than that of the unstrained region. Consequently, electrons and holes will localize in the unstrained region. The localization enhances the combination rate of electron and hole, and thus can lead to a stronger photoluminescence. The calculated charge densities of the CBM and VBM states of 4-**b**-TiS<sub>3</sub>NR, shown in Fig. 6.5(c), with a local strain of 8% (a part of the ribbon is strained and the other part is unstrained), show that both the CBM and VBM are mainly localized in the unstrained region. Except for carrier localization, local strain can also affect the charge transport properties of **b**-TiS<sub>3</sub>NRs. Enlargement of the band gap in the strained region induces energy barriers for electrons and holes in the ribbon, which can reduce the conductivity. Hence, the **b**-TiS<sub>3</sub>NRs can be potentially important as strain sensor.

### 6.3.2. Carrier Mobility

Carrier mobility is a critical property of semiconductors. High mobility leads to a high response of carriers to an external field, and therefore is feasible for high speed field-effect devices. In this part we discuss the carrier mobility of **b**-TiS<sub>3</sub>NRs. A recent theoretical study reported that the carrier mobility in 2D monolayer TiS<sub>3</sub> is highly anisotropic, and the electron mobility along the  $b$  direction is of the order of  $10^4 \text{ cm}^2\text{V}^{-1}\text{s}^{-1}$  (Dai and Zeng, 2015). Experimentally reported mobility of TiS<sub>3</sub> are of the order of  $10^2 \text{ cm}^2\text{V}^{-1}\text{s}^{-1}$  for sheets and  $10^0 \text{ cm}^2\text{V}^{-1}\text{s}^{-1}$  for ribbons (Island et al., 2014, 2015). The deviation between theoretical and experimental values stems from the fact that the TiS<sub>3</sub> in experiment are multi-layers rather than a monolayer, and that the presence of defects and a substrate

in the experiment can affect the mobility to a large extent. Nevertheless, predicting mobility from theory provides valuable insight to the fundamental properties of materials. Recently the anisotropic character of the carrier mobility in TiS<sub>3</sub> was also observed in the experimental study (Island et al., 2015).

In inorganic semiconductors, one dominant mechanism of scattering of carriers at low energy is the electron-acoustic phonon coupling, which can be well described by a deformation potential theory proposed by Bardeen and Shockly (Bardeen and Shockley, 1950). In combination with the effective mass approximation, the carrier mobility in 2D and 1D systems can be calculated by the following formulas (Beleznyay et al., 2003; Long et al., 2009, 2011; Cai et al., 2014):

$$\mu_{2D} = \frac{2e\hbar^3 C_{2D}}{3k_B T |m^*|^2 |E_1|^2} \quad (6.1)$$

$$\mu_{1D} = \frac{e\hbar^2 C_{1D}}{(2\pi k_B T)^{1/2} |m^*|^{3/2} |E_1|^2} \quad (6.2)$$

Here  $k_B$  is the Boltzmann constant,  $T$  is the temperature, and  $m^*$  is the carrier effective mass.  $E_1$  is the deformation potential constant.  $C_{1D}$  and  $C_{2D}$  are the elastic modulus for 1D and 2D systems, respectively.

It was demonstrated that polar scattering can be an important factor in limiting the carrier mobility at high temperatures (Ma and Jena, 2014). Neglecting polar scattering overestimates the carrier mobility. According to a recent work (Kaasbjerg et al., 2012), the carrier mobility is overestimated by 100% for MoS<sub>2</sub> if only acoustic scattering is considered. In the present study, we limit ourselves to an order of magnitude estimate and to the trend of the mobility rather than providing precise values. By neglecting polar scattering we cannot provide very accurate results for the mobility, however it can still give qualitatively satisfied results for orders of magnitude. For example, a previous study showed that the magnitude of mobility ( $\sim 100 \text{ cm}^2 \text{V}^{-1} \text{s}^{-1}$ ) of MoS<sub>2</sub> could be deduced by using Eqns. 6.1 (Cai et al., 2014).

The calculated mobility for different **b**-TiS<sub>3</sub>NRs, as well as those for 2D monolayer, are listed in Table 6.2. We show the trend of the mobility with the ribbon width in Fig. 6.6. For 2D TiS<sub>3</sub> sheet, our results is in good agreement with previous theoretical findings (Dai and Zeng, 2015). The electron (hole) mobility along the *b* direction is one order higher (lower) than that along the *a* direction. Moreover, the electron mobility along the *b* direction is as high as  $2.16 \times 10^4 \text{ cm}^2 \text{V}^{-1} \text{s}^{-1}$ , two orders higher than that of holes. This results from the larger effective mass and deformation potential of holes



than of electrons. The **b**-TiS<sub>3</sub>NRs are all along the *b* direction. Table 6.2 shows that the discrepancy in electron/hole mobility of 2D monolayer also appears in these ribbons. For  $N=4-10$ , the mobility of electrons in the ribbons varies from  $1.751 \times 10^3 \text{ cm}^2\text{V}^{-1}\text{s}^{-1}$  to  $4.222 \times 10^3 \text{ cm}^2\text{V}^{-1}\text{s}^{-1}$ . The hole mobility is in the range of  $1.68 \times 10^2 \text{ cm}^2\text{V}^{-1}\text{s}^{-1}$  to  $2.64 \times 10^2 \text{ cm}^2\text{V}^{-1}\text{s}^{-1}$ , one order lower than that of electrons. The effective mass of holes is about half of that of electrons, but holes have a much larger deformation potential, leading to their low mobility. As discussed above, the charge density of the VBM state has more components along the axial (*y*) direction than the CBM does, therefore it is more sensitive to axial strain, and the deformation potential of holes is larger.

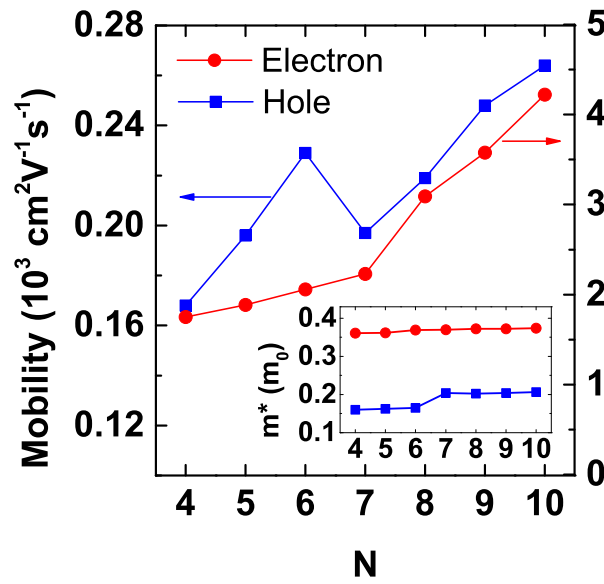


Figure 6.6. Carrier mobility for **b**-TiS<sub>3</sub>NRs. The inset shows the calculated effective mass  $m^*$  of electrons and holes for different ribbon widths.  $m_0$  is the mass of a free electron.

As shown in Fig. 6.6, generally the mobility increases with the width of the ribbon. Compared with the infinite 2D sheet, the electron mobility in **b**-TiS<sub>3</sub>NRs is smaller. From monolayer to nanoribbon, the electron effective mass is almost unchanged, but there is a large increase (70%–100%) in the deformation potential. This explains the reduction of the electron mobility. Nevertheless, the electron mobility of  $\sim 10^3 \text{ cm}^2\text{V}^{-1}\text{s}^{-1}$  in **b**-TiS<sub>3</sub>NRs is still considerable for TMCs. In contrast, the mobility of MoS<sub>2</sub> nanoribbons is only around  $200 \text{ cm}^2\text{V}^{-1}\text{s}^{-1}$  (Cai et al., 2014). Therefore, devices fabricated with **b**-TiS<sub>3</sub>NRs are expected to perform much better than those with MoS<sub>2</sub> nanoribbons. The presence of an edge reduces the electron mobility, but enhances the hole mobility. The

hole mobility in **b**-TiS<sub>3</sub>NRs is 2 to 3 times larger than that in a monolayer. Due to the strong edge effect, from monolayer to nanoribbon, the effective mass of the hole significantly reduces, which compensates the increase in deformation potential and leads to the higher mobility. In addition, from  $N=6$  to  $N=7$  there is a sudden decrease in hole mobility, which is mainly caused by the change in hole effective mass. As seen in the inset of Fig. 6.6, the hole effective mass is around  $0.16 m_0$  for  $N \leq 6$  and around  $0.20 m_0$  for  $N > 6$ . A larger effective mass leads to a smaller mobility.

It should be noted that Eqns. 6.1 assume an ideal parabolic band dispersion. It can be seen from Fig. 6.3a that the band dispersion of TiS<sub>3</sub>NRs around the CBM and VBM are close to parabolic dispersion. To further see whether such an approximation is valid, we did test calculations for 6-**b**-TiS<sub>3</sub>NR following the method of Long *et al.* (Long *et al.*, 2011) who used the full band dispersion instead of the effective mass approximation. The calculated mobility for electrons and holes were  $3.708 \times 10^3 \text{ cm}^2 \text{V}^{-1} \text{s}^{-1}$  and  $0.352 \times 10^3 \text{ cm}^2 \text{V}^{-1} \text{s}^{-1}$ , respectively. On the other hand, using the effective mass approximation results in an electron mobility of  $2.057 \times 10^3 \text{ cm}^2 \text{V}^{-1} \text{s}^{-1}$  and a hole mobility of  $0.229 \times 10^3 \text{ cm}^2 \text{V}^{-1} \text{s}^{-1}$  as listed in Table 6.2. Thus both methods lead to the same conclusion that the magnitude of electron and hole mobility is  $10^3 \text{ cm}^2 \text{V}^{-1} \text{s}^{-1}$  and  $10^2 \text{ cm}^2 \text{V}^{-1} \text{s}^{-1}$ , respectively. Our main concern was to provide an order of magnitude and the trend in the mobility rather than precise values, and therefore the effective mass approximation is sufficient for the systems studied in the present work.

## 6.4. Edge Termination

Formation of one-dimensional structures of single layer crystals results in the emergence of additional features such as edge states. It has been shown for many materials that termination of dangling bond states located at the edges can change the characteristics of the material drastically. In this section we investigate the effect of edge termination on the electronic and magnetic properties of **a**- and **b**-TiS<sub>3</sub>NRs. For the termination of ribbon edges we make use of hydrogenation. Compared to graphene nanoribbons, TiS<sub>3</sub> NRs are quite different due to their edge morphology. At each ribbon edge, while **a**-TiS<sub>3</sub>NRs have four edge atoms in its unitcell, **b**-TiS<sub>3</sub>NRs have two edge atoms. Among the various possible hydrogenation scenarios we employ single hydrogen termination of each edge atom.

Our calculations reveal that upon hydrogenation of **a**-TiS<sub>3</sub>NR edges, metallic behavior of bare **a**-edged ribbons is still preserved. As shown in Fig. 6.7(a), compared with

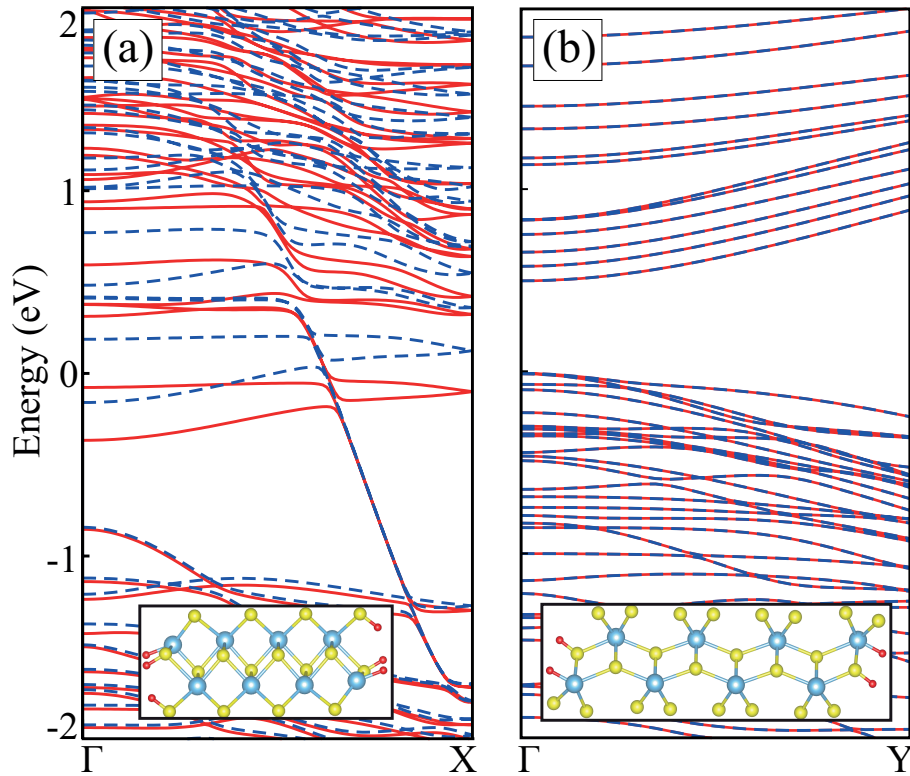


Figure 6.7. (Color online) Band dispersions of (a) 8-**a**-TiS<sub>3</sub>NR and (b) 8-**b**-TiS<sub>3</sub>NR in which the edge atoms are passivated by hydrogen (red colored) atoms. The solid and dashed curves are spin-up and spin-down components. Insets: side view of edge structure.

the bare edge case the overall electronic band dispersion of 8-**a**-TiS<sub>3</sub>NR is not affected significantly. However, the magnetic ground state of the structure is modified upon edge termination. As can be deduced from the enhanced splitting in spin up (solid curves) and spin down (dashed curves) bands, hydrogenated ribbons possess larger net magnetic moment in their ground state. For instance, in the case of 8-**a**-TiS<sub>3</sub>NR the total magnetic moment increases from 0.3 to 1.1  $\mu_B$  per unit cell. The robust metallic and ferromagnetic nature of **a**-TiS<sub>3</sub>NRs is an essential feature for spintronic device applications.

On the other hand, the situation is entirely different for **b**-TiS<sub>3</sub>NRs. Comparing Fig. 6.7(b) and Fig. 6.3(a), the band gap of 8-**b**-TiS<sub>3</sub>NR enlarges due to edge termination. It increased from 0.32 to 0.51 eV. Moreover, although the VBM and the CBM points are still located at the  $\Gamma$  point, the band dispersion is significantly affected by the edge termination. It is also seen that similar to bare ribbons hydrogen terminated **b**-TiS<sub>3</sub>NRs are nonmagnetic. The presence of a band gap in the electronic structure of **b**-TiS<sub>3</sub>NRs is important for their potential use in optoelectronic device applications.

In summary, we investigated the electronic properties, mobility and strain response of  $\text{TiS}_3$  NRs by first-principles calculations. Two types of ribbons with different orientations are studied, labeled as **a**- $\text{TiS}_3$  NRs and **b**- $\text{TiS}_3$  NRs. The **a**- $\text{TiS}_3$  NRs have large edge energy ranging from 450 to 480 meV/Å. On the other hand, the **b**- $\text{TiS}_3$  NRs are found to have small edge energy around 60 meV/Å, suggesting that their isolation from 2D monolayer is not difficult. All the **a**- $\text{TiS}_3$  NRs are metallic, and exhibit non-zero magnetic moment. The spin density is contributed mostly by edge atoms. On the contrast, all the **b**- $\text{TiS}_3$  NRs have direct band gaps at the  $\Gamma$  point. Interestingly, the gap value and the band edge position are almost independent of the ribbon width, indicating strong edge effects. This feature promises a constant band gap in a **b**- $\text{TiS}_3$  NR with rough edge, where the ribbon width differs in different regions. The mobility of **b**- $\text{TiS}_3$  NRs is calculated by using the deformation potential theory in combine with the effect mass approximation. The **b**- $\text{TiS}_3$  NRs exhibit high electron mobility in the order of  $10^3 \text{ cm}^2\text{V}^{-1}\text{s}^{-1}$ . The hole mobility of the **b**- $\text{TiS}_3$  NRs is one order lower, but it is enhanced compared with the monolayer case, due to a reduction in hole effective mass. The band gap of **b**- $\text{TiS}_3$  NRs is strain tunable. It increases with increasing tensile strain, and a direct-to-indirect band gap transition can be triggered by strain. Moreover, local strain in a **b**- $\text{TiS}_3$  NR creates a type-I band offset, which can induce carrier localization and charge transport barrier.

# CHAPTER 7

## CONCLUSION

The main goal of this thesis was to investigate the electronic and structural properties of graphene and graphene-like free standing nanostructures such as transition metal chalcogenides by using first-principles calculations based on density functional theory. We have presented the extensive ab-initio investigation for characteristic properties of two- and one-dimensional different nanoscale structures.

First we have studied the adsorption, diffusion and magnetic properties of Pt clusters on three different two-dimensional atomic crystals. We have been able to understand graphene, 1H-MoS<sub>2</sub> 1T-TaS<sub>2</sub> provide different nucleation characteristics for Pt cluster formation. At low temperatures, while the bridge site is the most favorable site where the growth of a Pt cluster starts on graphene, top-Mo and top-Ta sites are preferred on 1H-MoS<sub>2</sub> and 1T-TaS<sub>2</sub>, respectively. We found that the formation of Pt<sub>2</sub> dimer and a triangle-shaped Pt<sub>3</sub> cluster perpendicular to the surface are favored over the three different surfaces. While bent rhombus shaped Pt<sub>4</sub> is formed on graphene, the formation of tetrahedral shaped clusters are more favorable on 1H-MoS<sub>2</sub> and 1T-TaS<sub>2</sub>. We can conclude that the formation of Pt<sub>*n*</sub> clusters is favorable on graphene, MoS<sub>2</sub> and TaS<sub>2</sub> substrates.

Next, we have predicted that the electronic and magnetic properties of TiSe<sub>2</sub> monolayer can be tuned by hydrogenation. The results demonstrate that non-metal hydrogen atom can be chemically adsorbed on the surface of 2D-TiSe<sub>2</sub> substrate where the most stable configuration is the top of Se atom. Differing from bare TiSe<sub>2</sub>, electronic band structure calculations indicate that one-side hydrogenation of TiSe<sub>2</sub> has half-metallic characteristic in its ground state. However, two-side is fully covered with hydrogen atom, the ground state is still metallic like bare form. Moreover, we can conclude that only one-side hydrogenated structure can introduce magnetism with the total magnetic moment is found to be 1.0  $\mu_B$ . The spin-polarized state is dominated by 3*d* orbitals of Ti atom, while contributions from other atoms are relatively small. Due to the exceptional electronic band dispersion, in which the metallic behavior in one spin-direction, while semiconducting behavior in the another spin direction, we have obtained the estimated  $T_c$  value of 248 K. In addition, the electronic band dispersion is also revealed that electron effective masses are highly anisotropic around the M-point. Moreover, the hetero form of hydrogenated monolayers on HfX<sub>2</sub> (X=S,Se) is also investigated. The PBE results demonstrate that the

structural and electronic properties of heterostructure indicate some differences. One-side hydrogenated TiSe<sub>2</sub> monolayer has still half-metallic electronic band character on HfSe<sub>2</sub>, whereas the metallicity of the two-side hydrogenated structure undergoes a minor change on HfS<sub>2</sub> monolayer but the metallic characteristic is still preserved. Finally, the intrinsic ferromagnetic property and the different electronic band dispersions are achieved through the hydrogenated TiSe<sub>2</sub> monolayer. As a result, the functionalization of TiSe<sub>2</sub> monolayer surfaces with hydrogen could be opened a new path to explore spintronics.

Lastly, we have performed electronic and magnetic properties of two different types materials in the nanoribbon form; TiSe<sub>2</sub> (and PtSe<sub>2</sub>) and TiS<sub>3</sub>. Overall, our results demonstrate that TMD nanoribbons which are in 1T phase have quite different characteristics from nanoribbons of other widely studied materials such as graphene or MoS<sub>2</sub>. Our calculations revealed that only ultranarrow zigzag and armchair nanoribbons exhibit semiconducting behavior and their band gap rapidly decreases to zero with increasing ribbon width.  $N_a \geq 6$  and  $N_z \geq 7$  nanoribbons exhibit metallic behavior like two-dimensional TiSe<sub>2</sub>. The width dependency of the band gap can be fairly represented by an exponential decay function. Both zigzag and armchair ribbons have nonmagnetic ground states. In addition, the robust metallic behavior of both zigzag and armchair TiSe<sub>2</sub> nanoribbons remains unaltered even after passivation of the edges by hydrogen atoms. The metallic character of the wider ribbons of TiSe<sub>2</sub> regardless of their edge symmetry is an advantageous property for utilizing them as one-dimensional interconnects of nanoscale circuits. In contrast to TiSe<sub>2</sub> NRs, the electronic structures show ultranarrow and almost width independent band gap for both zigzag and armchair edged PtSe<sub>2</sub> NRs. Both types of ribbons have non-magnetic ground states similar to TiSe<sub>2</sub> NRs. However, the band gaps of PtSe<sub>2</sub> NRs increase due to the edge termination. Upon hydrogenation of zigzag PtSe<sub>2</sub> NRs, the non-magnetic behavior is still preserved. While for armchair edged PtSe<sub>2</sub> NRs are magnetic after hydrogen passivation.

Different from 1T phase of nanoribbons, transition metal tri-chalcogenide TiS<sub>3</sub> NRs exhibit entirely different structural and electronic characteristics. Instead of zigzag and armchair edged NRs, the **a**- and **b**-edged TiS<sub>3</sub> NRs are labeled because of the rectangular unitcell of the TiS<sub>3</sub> monolayer. The **a**-TiS<sub>3</sub> NRs and **b**-TiS<sub>3</sub> NRs show very different properties. The **a**-TiS<sub>3</sub> NRs have large edge energy ranging from 450 to 480 meV/Å. On the other hand, the **b**-TiS<sub>3</sub> NRs are found to have small edge energy around 60 meV/Å, suggesting that the isolation of **b**-TiS<sub>3</sub> NRs from 2D monolayer is not difficult. All the **a**-TiS<sub>3</sub> NRs are metallic, and exhibit non-zero magnetic moment. The spin density is contributed mostly by edge atoms. All the TiS<sub>3</sub> NRs have direct band gaps

at the  $\Gamma$  point. Interestingly, the gap value is almost independent of the ribbon width, indicating strong edge effects. From monolayer to nanoribbon, the electron mobility of  $\text{TiS}_3$  is reduced. Nevertheless, the **b**- $\text{TiS}_3$  NRs still have high electron mobility, in the order of  $10^3 \text{ cm}^2\text{V}^{-1}\text{s}^{-1}$ . The hole mobility of the **b**- $\text{TiS}_3$  NRs is one order lower, but it is enhanced compared with the monolayer case, due to a reduction in hole effective mass. When tensile strain is applied, the band gap of **b**- $\text{TiS}_3$  NRs increases, and a direct-to-indirect band gap transition occurs. Moreover, local strain in a **b**- $\text{TiS}_3$  NR creates a type-I band offset, which can induce carrier localization and a charge transport barrier. The direct, width-independent and strain tunable band gap, as well as the high carrier mobility, promise **b**- $\text{TiS}_3$  NRs great application potentials in many fields nanoelectronics, such as field-effect devices, opto-electronic applications and strain sensor.

Consequently, the discovery of 2D materials has started a new era of materials science. New materials, atomically thin and mechanically, thermally and electronically stable, with a large variety of electronic properties are available and they can be assembled in ultrathin flexible devices. The manufacturing of new devices requires the detailed understanding of the properties of two- and one-dimensional materials, which is supported by structural and electronic properties presented in this thesis.

## REFERENCES

- Ataca, C., H. Sahin, and S. Ciraci (2012). Stable, single-layer  $mx_2$  transition-metal oxides and dichalcogenides in a honeycomb-like structure. *The Journal of Physical Chemistry C* 116(16), 8983–8999.
- Aydinol, M., A. Kohan, G. Ceder, K. Cho, and J. Joannopoulos (1997). Ab initio study of lithium intercalation in metal oxides and metal dichalcogenides. *Physical Review B* 56(3), 1354.
- Balendhran, S., S. Walia, H. Nili, S. Sriram, and M. Bhaskaran (2015). Elemental analogues of graphene: silicene, germanene, stanene, and phosphorene. *Small* 11(6), 640–652.
- Bardeen, J. and W. Shockley (1950). Deformation potentials and mobilities in non-polar crystals. *Physical Review* 80(1), 72.
- Barone, V., O. Hod, and G. E. Scuseria (2006). Electronic structure and stability of semi-conducting graphene nanoribbons. *Nano letters* 6(12), 2748–2754.
- Beleznay, F., F. Bogár, and J. Ladik (2003). Charge carrier mobility in quasi-one-dimensional systems: Application to a guanine stack. *The Journal of chemical physics* 119(11), 5690–5695.
- Bianco, E., S. Butler, S. Jiang, O. D. Restrepo, W. Windl, and J. E. Goldberger (2013). Stability and exfoliation of germanane: a germanium graphane analogue. *Acs Nano* 7(5), 4414–4421.
- Blöchl, P. E. (1994). Projector augmented-wave method. *Physical Review B* 50(24), 17953.
- Błoński, P., S. Dennler, and J. Hafner (2011). Strong spin–orbit effects in small pt clusters: geometric structure, magnetic isomers and anisotropy. *The Journal of chemical physics* 134(3), 034107.
- Błoński, P. and J. Hafner (2011). Geometric and magnetic properties of pt clusters sup-



- ported on graphene: Relativistic density-functional calculations. *The Journal of chemical physics* 134(15), 154705.
- Born, M. and R. Oppenheimer (1927). On the quantum theory of molecules. *Ann. Phys* 84(4), 457–484.
- Bovet, M., D. Popović, F. Clerc, C. Koitzsch, U. Probst, E. Bucher, H. Berger, D. Naimović, and P. Aebi (2004). Pseudogapped fermi surfaces of 1 t- tas 2 and 1 t- tase 2: A charge density wave effect. *Physical Review B* 69(12), 125117.
- Brattas, L. and A. Kjekshus (1972). Properties of compounds with zrse 3-type structure. *Acta Chemica Scandinavica* 26(9), 3441–3449.
- Butler, S. Z., S. M. Hollen, L. Cao, Y. Cui, J. A. Gupta, H. R. Gutierrez, T. F. Heinz, S. S. Hong, J. Huang, A. F. Ismach, et al. (2013). Progress, challenges, and opportunities in two-dimensional materials beyond graphene. *ACS nano* 7(4), 2898–2926.
- Cabria, I., M. López, and J. Alonso (2010). Theoretical study of the transition from planar to three-dimensional structures of palladium clusters supported on graphene. *Physical Review B* 81(3), 035403.
- Cai, J., P. Ruffieux, R. Jaafar, M. Bieri, T. Braun, S. Blankenburg, M. Muoth, A. P. Seitsonen, M. Saleh, X. Feng, et al. (2010). Atomically precise bottom-up fabrication of graphene nanoribbons. *Nature* 466(7305), 470–473.
- Cai, Y., G. Zhang, and Y.-W. Zhang (2014). Polarity-reversed robust carrier mobility in monolayer mos2 nanoribbons. *Journal of the American Chemical Society* 136(17), 6269–6275.
- Calandra, M. and F. Mauri (2011). Charge-density wave and superconducting dome in tise 2 from electron-phonon interaction. *Physical review letters* 106(19), 196406.
- Chan, K. T., J. Neaton, and M. L. Cohen (2008). First-principles study of metal adatom adsorption on graphene. *Physical Review B* 77(23), 235430.
- Chen, C., W. Fabian, F. Brown, K. Woo, B. Davies, B. DeLong, and A. Thompson (1980). Angle-resolved photoemission studies of the band structure of ti se 2 and ti s 2. *Phys-*

*ical Review B* 21(2), 615.

Chhowalla, M., H. S. Shin, G. Eda, L.-J. Li, K. P. Loh, and H. Zhang (2013a). The chemistry of two-dimensional layered transition metal dichalcogenide nanosheets. *Nature chemistry* 5(4), 263–275.

Chhowalla, M., H. S. Shin, G. Eda, L.-J. Li, K. P. Loh, and H. Zhang (2013b). The chemistry of two-dimensional layered transition metal dichalcogenide nanosheets. *Nature chemistry* 5(4), 263–275.

Claessen, R., R. Anderson, G.-H. Gweon, J. Allen, W. Ellis, C. Janowitz, C. Olson, Z. Shen, V. Eyert, M. Skibowski, et al. (1996). Complete band-structure determination of the quasi-two-dimensional fermi-liquid reference compound tite 2. *Physical Review B* 54(4), 2453.

Cong, X., C. Cheng, Y. Liao, Y. Ye, C. Dong, H. Sun, X. Ji, W. Zhang, P. Fang, L. Miao, et al. (2015). Intrinsic charge storage capability of transition metal dichalcogenides as pseudocapacitor electrodes. *The Journal of Physical Chemistry C* 119(36), 20864–20870.

Dai, J. and X. C. Zeng (2015). Titanium trisulfide monolayer: Theoretical prediction of a new direct-gap semiconductor with high and anisotropic carrier mobility. *Angewandte Chemie International Edition* 54(26), 7572–7576.

De Boer, D., C. Van Bruggen, G. Bus, R. Coehoorn, C. Haas, G. Sawatzky, H. Myron, D. Norman, and H. Padmore (1984). Titanium ditelluride: Band structure, photoemission, and electrical and magnetic properties. *Physical Review B* 29(12), 6797.

Di Salvo, F. J., D. Moncton, and J. Waszczak (1976). Electronic properties and superlattice formation in the semimetal tise 2. *Physical Review B* 14(10), 4321.

Dubois, S.-M., Z. Zanolli, X. Declerck, and J.-C. Charlier (2009). Electronic properties and quantum transport in graphene-based nanostructures. *The European Physical Journal B* 72(1), 1–24.

Eda, G., H. Yamaguchi, D. Voiry, T. Fujita, M. Chen, and M. Chhowalla (2011). Photoluminescence from chemically exfoliated mos2. *Nano letters* 11(12), 5111–5116.

- Elias, D. C., R. R. Nair, T. Mohiuddin, S. Morozov, P. Blake, M. Halsall, A. Ferrari, D. Boukhvalov, M. Katsnelson, A. Geim, et al. (2009). Control of graphene's properties by reversible hydrogenation: evidence for graphane. *Science* 323(5914), 610–613.
- Fang, C., R. De Groot, and C. Haas (1997). Bulk and surface electronic structure of 1 t-tis 2 and 1 t-tise 2. *Physical Review B* 56(8), 4455.
- Fermi, E. (1927). Application of statistical gas methods to electronic systems. *Atti Accad. Naz. Lincei* 6, 602–607.
- Ferrer, I., J. Ares, J. Clamagirand, M. Barawi, and C. Sánchez (2013). Optical properties of titanium trisulphide (tis 3) thin films. *Thin Solid Films* 535, 398–401.
- Ferrer, I., M. Maciá, V. Carcelén, J. Ares, and C. Sánchez (2012). On the photoelectrochemical properties of tis 3 films. *Energy Procedia* 22, 48–52.
- Gao, D., S. Shi, K. Tao, B. Xia, and D. Xue (2015). Tunable ferromagnetic ordering in mos2 nanosheets with fluorine adsorption. *Nanoscale* 7(9), 4211–4216.
- Grimme, S. (2006). Semiempirical gga-type density functional constructed with a long-range dispersion correction. *Journal of computational chemistry* 27(15), 1787–1799.
- Güller, F., A. Llois, J. Goniakowski, and C. Noguera (2015). Prediction of structural and metal-to-semiconductor phase transitions in nanoscale mos 2, ws 2, and other transition metal dichalcogenide zigzag ribbons. *Physical Review B* 91(7), 075407.
- Han, M. Y., B. Özyilmaz, Y. Zhang, and P. Kim (2007). Energy band-gap engineering of graphene nanoribbons. *Physical review letters* 98(20), 206805.
- He, J., K. Wu, R. Sa, Q. Li, Y. Wei, et al. (2010). Magnetic properties of nonmetal atoms absorbed mos2 monolayers. *Applied Physics Letters* 96(8), 082504.
- He, K., C. Poole, K. F. Mak, and J. Shan (2013). Experimental demonstration of continuous electronic structure tuning via strain in atomically thin mos2. *Nano letters* 13(6), 2931–2936.

- Henkelman, G., A. Arnaldsson, and H. Jónsson (2006). A fast and robust algorithm for bader decomposition of charge density. *Computational Materials Science* 36(3), 354–360.
- Heyd, J., G. E. Scuseria, and M. Ernzerhof (2003). Hybrid functionals based on a screened coulomb potential. *The Journal of Chemical Physics* 118(18), 8207–8215.
- Heyd, J., G. E. Scuseria, and M. Ernzerhof (2006). Erratum:“hybrid functionals based on a screened coulomb potential”[j. chem. phys. 118, 8207 (2003)]. *The Journal of Chemical Physics* 124(21), 219906.
- Hildebrand, B., C. Didiot, A. M. Novello, G. Monney, A. Scarfato, A. Ubaldini, H. Berger, D. Bowler, C. Renner, and P. Aebi (2014). Doping nature of native defects in 1 t- tise 2. *Physical review letters* 112(19), 197001.
- Hohenberg, P. and W. Kohn (1964). Inhomogeneous electron gas. *Physical review* 136(3B), B864.
- Huda, M., M. K. Niranjana, B. Sahu, and L. Kleinman (2006). Effect of spin-orbit coupling on small platinum nanoclusters. *Physical Review A* 73(5), 053201.
- Ishii, A., M. Yamamoto, H. Asano, and K. Fujiwara (2008). Dft calculation for adatom adsorption on graphene sheet as a prototype of carbon nanotube functionalization. In *Journal of Physics: Conference Series*, Volume 100, pp. 052087. IOP Publishing.
- Island, J. O., M. Barawi, R. Biele, A. Almazán, J. M. Clamagirand, J. R. Ares, C. Sánchez, H. S. van der Zant, J. V. Álvarez, R. D’Agosta, et al. (2015). Tis3 transistors with tailored morphology and electrical properties. *Advanced Materials* 27(16), 2595–2601.
- Island, J. O., M. Buscema, M. Barawi, J. M. Clamagirand, J. R. Ares, C. Sánchez, I. J. Ferrer, G. A. Steele, H. S. van der Zant, and A. Castellanos-Gomez (2014). Ultrahigh photoresponse of few-layer tis3 nanoribbon transistors. *Advanced Optical Materials* 2(7), 641–645.
- Iyikanat, F., H. Sahin, R. Senger, and F. Peeters (2015). Vacancy formation and oxidation characteristics of single layer tis3. *The Journal of Physical Chemistry C* 119(19),

10709–10715.

- Jaiswal, M., C. H. Yi Xuan Lim, Q. Bao, C. T. Toh, K. P. Loh, and B. Ozyilmaz (2011). Controlled hydrogenation of graphene sheets and nanoribbons. *ACS nano* 5(2), 888–896.
- Jin, Y., X. Li, and J. Yang (2015). Single layer of  $mx_3$  ( $m = \text{ti, zr}$ ;  $x = \text{s, se, te}$ ): a new platform for nano-electronics and optics. *Physical Chemistry Chemical Physics* 17(28), 18665–18669.
- Jishi, R. and H. Alyahyaei (2008). Electronic structure of superconducting copper intercalated transition metal dichalcogenides: First-principles calculations. *Physical Review B* 78(14), 144516.
- Johari, P. and V. B. Shenoy (2012). Tuning the electronic properties of semiconducting transition metal dichalcogenides by applying mechanical strains. *ACS nano* 6(6), 5449–5456.
- Jones, R. O. and O. Gunnarsson (1989). The density functional formalism, its applications and prospects. *Reviews of Modern Physics* 61(3), 689.
- Jun, S. (2008). Density-functional study of edge stress in graphene. *Physical Review B* 78(7), 073405.
- Kaasbjerg, K., K. S. Thygesen, and K. W. Jacobsen (2012). Phonon-limited mobility in n-type single-layer mos 2 from first principles. *Physical Review B* 85(11), 115317.
- Kan, M., J. Zhou, Q. Sun, Y. Kawazoe, and P. Jena (2013). The intrinsic ferromagnetism in a  $\text{mno}_2$  monolayer. *The journal of physical chemistry letters* 4(20), 3382–3386.
- Kang, J., H. Sahin, H. D. Ozaydin, R. T. Senger, and F. M. Peeters (2015). Tis 3 nanoribbons: Width-independent band gap and strain-tunable electronic properties. *Physical Review B* 92(7), 075413.
- Kim, J., S. Byun, A. J. Smith, J. Yu, and J. Huang (2013). Enhanced electrocatalytic properties of transition-metal dichalcogenides sheets by spontaneous gold nanoparticle decoration. *The journal of physical chemistry letters* 4(8), 1227–1232.

- Kim, J., M. V. Fischetti, and S. Aboud (2012). Structural, electronic, and transport properties of silicane nanoribbons. *Physical Review B* 86(20), 205323.
- Koch, W. and M. C. Holthausen (2015). *A chemist's guide to density functional theory*. John Wiley & Sons.
- Koh, E. W. K., C. H. Chiu, Y. K. Lim, Y.-W. Zhang, and H. Pan (2012). Hydrogen adsorption on and diffusion through mos 2 monolayer: First-principles study. *International journal of hydrogen energy* 37(19), 14323–14328.
- Kohn, W. and L. J. Sham (1965). Self-consistent equations including exchange and correlation effects. *Physical review* 140(4A), A1133.
- Kresse, G. and J. Furthmüller (1996). Efficient iterative schemes for ab initio total-energy calculations using a plane-wave basis set. *Physical review B* 54(16), 11169.
- Kresse, G. and D. Joubert (1999). From ultrasoft pseudopotentials to the projector augmented-wave method. *Physical Review B* 59(3), 1758.
- Kudrnovský, J., I. Turek, V. Drchal, F. Máca, P. Weinberger, and P. Bruno (2004). Exchange interactions in iii-v and group-iv diluted magnetic semiconductors. *Physical review B* 69(11), 115208.
- Kusmartseva, A. F., B. Sipos, H. Berger, L. Forro, and E. Tutiš (2009). Pressure induced superconductivity in pristine 1 t- tise 2. *Physical review letters* 103(23), 236401.
- Landau, L. D. and E. Lifshitz (1980). *Statistical physics, part i*.
- Li, G., W. Hu, D. Qian, D. Hsieh, M. Hasan, E. Morosan, R. Cava, and N. Wang (2007). Semimetal-to-semimetal charge density wave transition in 1 t- tise 2. *Physical review letters* 99(2), 027404.
- Li, H., Z. Yin, Q. He, H. Li, X. Huang, G. Lu, D. W. H. Fam, A. I. Y. Tok, Q. Zhang, and H. Zhang (2012). Fabrication of single- and multilayer mos2 film-based field-effect transistors for sensing no at room temperature. *small* 8(1), 63–67.
- Li, P., L. Li, and X. C. Zeng (2016). Tuning the electronic properties of monolayer and

- bilayer ptse 2 via strain engineering. *Journal of Materials Chemistry C* 4(15), 3106–3112.
- Li, X., X. Wang, L. Zhang, S. Lee, and H. Dai (2008). Chemically derived, ultrasmooth graphene nanoribbon semiconductors. *Science* 319(5867), 1229–1232.
- Li, Y., Z. Zhou, S. Zhang, and Z. Chen (2008). Mos2 nanoribbons: high stability and unusual electronic and magnetic properties. *Journal of the American Chemical Society* 130(49), 16739–16744.
- Long, M., L. Tang, D. Wang, Y. Li, and Z. Shuai (2011). Electronic structure and carrier mobility in graphdiyne sheet and nanoribbons: theoretical predictions. *ACS nano* 5(4), 2593–2600.
- Long, M.-Q., L. Tang, D. Wang, L. Wang, and Z. Shuai (2009). Theoretical predictions of size-dependent carrier mobility and polarity in graphene. *Journal of the American Chemical Society* 131(49), 17728–17729.
- Lopez-Sanchez, O., D. Lembke, M. Kayci, A. Radenovic, and A. Kis (2013). Ultrasensitive photodetectors based on monolayer mos2. *Nature nanotechnology* 8(7), 497–501.
- Ma, N. and D. Jena (2014). Charge scattering and mobility in atomically thin semiconductors. *Physical Review X* 4(1), 011043.
- Mak, K. F., C. Lee, J. Hone, J. Shan, and T. F. Heinz (2010). Atomically thin mos 2: a new direct-gap semiconductor. *Physical Review Letters* 105(13), 136805.
- Manchanda, P., V. Sharma, H. Yu, D. J. Sellmyer, and R. Skomski (2015). Magnetism of ta dichalcogenide monolayers tuned by strain and hydrogenation. *Applied Physics Letters* 107(3), 032402.
- Meziane, S., H. Feraoun, T. Ouahrani, and C. Esling (2013). Effects of li and na intercalation on electronic, bonding and thermoelectric transport properties of mx 2 (m= ta; x= s or se) dichalcogenides—ab initio investigation. *Journal of Alloys and Compounds* 581, 731–740.
- Miro, P., M. Audiffred, and T. Heine (2014). An atlas of two-dimensional materials.

*Chemical Society Reviews* 43(18), 6537–6554.

Monkhorst, H. J. and J. D. Pack (1976). Special points for brillouin-zone integrations. *Physical review B* 13(12), 5188.

Mori-Sánchez, P., A. J. Cohen, and W. Yang (2008). Localization and delocalization errors in density functional theory and implications for band-gap prediction. *Physical review letters* 100(14), 146401.

Morosan, E., H. Zandbergen, B. Dennis, J. Bos, Y. Onose, T. Klimczuk, A. Ramirez, N. Ong, and R. Cava (2006). Superconductivity in *CuTe<sub>2</sub>*. *Nature Physics* 2(8), 544–550.

Neto, A. C., F. Guinea, N. M. Peres, K. S. Novoselov, and A. K. Geim (2009). The electronic properties of graphene. *Reviews of modern physics* 81(1), 109.

Ni, Z., Q. Liu, K. Tang, J. Zheng, J. Zhou, R. Qin, Z. Gao, D. Yu, and J. Lu (2011). Tunable bandgap in silicene and germanene. *Nano letters* 12(1), 113–118.

Nicolosi, V., M. Chhowalla, M. G. Kanatzidis, M. S. Strano, and J. N. Coleman (2013). Liquid exfoliation of layered materials. *Science* 340(6139), 1226419.

Novoselov, K., A. K. Geim, S. Morozov, D. Jiang, M. Katsnelson, I. Grigorieva, S. Dubonos, and A. Firsov (2005). Two-dimensional gas of massless dirac fermions in graphene. *nature* 438(7065), 197–200.

Novoselov, K. S., A. K. Geim, S. V. Morozov, D. Jiang, Y. Zhang, S. V. Dubonos, I. V. Grigorieva, and A. A. Firsov (2004). Electric field effect in atomically thin carbon films. *science* 306(5696), 666–669.

Novoselov, K. S., Z. Jiang, Y. Zhang, S. Morozov, H. Stormer, U. Zeitler, J. Maan, G. Boebinger, P. Kim, and A. Geim (2007). Room-temperature quantum hall effect in graphene. *Science* 315(5817), 1379–1379.

O’hare, A., F. Kusmartsev, and K. Kugel (2012). A stable flat form of two-dimensional crystals: Could graphene, silicene, germanene be minigap semiconductors? *Nano letters* 12(2), 1045–1052.



- Oshima, C. and A. Nagashima (1997). Ultra-thin epitaxial films of graphite and hexagonal boron nitride on solid surfaces. *Journal of Physics: Condensed Matter* 9(1), 1.
- Ozaydin, H., H. Sahin, J. Kang, F. Peeters, and R. Senger (2015). Electronic and magnetic properties of 1 t-tise2 nanoribbons. *2D Materials* 2(4), 044002.
- Ozaydin, H. D., H. Sahin, R. T. Senger, and F. M. Peeters (2014). Formation and diffusion characteristics of pt clusters on graphene, 1h-mos2 and 1t-tas2. *Annalen der Physik* 526(9-10), 423–429.
- Pan, H. (2014). Electronic and magnetic properties of vanadium dichalcogenides monolayers tuned by hydrogenation. *The Journal of Physical Chemistry C* 118(24), 13248–13253.
- Parr, R. G. (1980). Density functional theory of atoms and molecules. In *Horizons of Quantum Chemistry*, pp. 5–15. Springer.
- Payne, M. C., M. P. Teter, D. C. Allan, T. Arias, and J. Joannopoulos (1992). Iterative minimization techniques for ab initio total-energy calculations: molecular dynamics and conjugate gradients. *Reviews of Modern Physics* 64(4), 1045.
- Peierls, R. (1934). Remarks on transition temperatures. *Helv. Phys. Acta* 7(2), 81–83.
- Peierls, R. (1935). Quelques propriétés typiques des corps solides. In *Annales de l'institut Henri Poincaré*, Volume 5, pp. 177–222.
- Peng, J.-P., J.-Q. Guan, H.-M. Zhang, C.-L. Song, L. Wang, K. He, Q.-K. Xue, and X.-C. Ma (2015). Molecular beam epitaxy growth and scanning tunneling microscopy study of tise 2 ultrathin films. *Physical Review B* 91(12), 121113.
- Perdew, J. P., K. Burke, and M. Ernzerhof (1996). Generalized gradient approximation made simple. *Physical review letters* 77(18), 3865.
- Perdew, J. P., J. Chevary, S. Vosko, K. A. Jackson, M. R. Pederson, D. Singh, and C. Fiolhais (1992). Atoms, molecules, solids, and surfaces: Applications of the generalized gradient approximation for exchange and correlation. *Physical Review B* 46(11), 6671.

- Pillo, T., J. Hayoz, H. Berger, F. Lévy, L. Schlapbach, and P. Aebi (2000). Photoemission of bands above the fermi level: The excitonic insulator phase transition in 1 t- tise 2. *Physical Review B* 61(23), 16213.
- Pumera, M. and C. H. A. Wong (2013). Graphane and hydrogenated graphene. *Chemical Society Reviews* 42(14), 5987–5995.
- Radisavljevic, B. and A. Kis (2013). Mobility engineering and a metal–insulator transition in monolayer mos2. *Nature materials* 12(9), 815–820.
- Radisavljevic, B., A. Radenovic, J. Brivio, i. V. Giacometti, and A. Kis (2011). Single-layer mos2 transistors. *Nature nanotechnology* 6(3), 147–150.
- Ramirez, C. and W. Schattke (2001). Diffusion and intercalation of alkali atoms in transition metal dichalcogenides. *Surface science* 482, 424–429.
- Rasch, J. C., T. Stemmler, B. Müller, L. Dudy, and R. Manzke (2008). 1 t- tise 2: Semimetal or semiconductor? *Physical review letters* 101(23), 237602.
- Robinson, T. (2012). On klein tunneling in graphene. *American Journal of Physics* 80(2), 141–147.
- Rösner, M., S. Haas, and T. Wehling (2014). Phase diagram of electron-doped dichalcogenides. *Physical Review B* 90(24), 245105.
- Ryu, S., M. Y. Han, J. Maultzsch, T. F. Heinz, P. Kim, M. L. Steigerwald, and L. E. Brus (2008). Reversible basal plane hydrogenation of graphene. *Nano letters* 8(12), 4597–4602.
- Şahin, H., C. Ataca, and S. Ciraci (2010). Electronic and magnetic properties of graphane nanoribbons. *Physical Review B* 81(20), 205417.
- Sahin, H. and S. Ciraci (2012). Chlorine adsorption on graphene: Chlorographene. *The Journal of Physical Chemistry C* 116(45), 24075–24083.
- Şahin, H., M. Topsakal, and S. Ciraci (2011). Structures of fluorinated graphene and their signatures. *Physical Review B* 83(11), 115432.

- Samuelsen, D., E. Pehlke, W. Schattke, O. Anderson, R. Manzke, and M. Skibowski (1992). Observation of surface-induced photon fields in the photoemission of 1t-tis 2. *Physical review letters* 68(4), 522.
- Schmidt, M. W., K. K. Baldrige, J. A. Boatz, S. T. Elbert, M. S. Gordon, J. H. Jensen, S. Koseki, N. Matsunaga, K. A. Nguyen, S. Su, et al. (1993). General atomic and molecular electronic structure system. *Journal of computational chemistry* 14(11), 1347–1363.
- Schrödinger, E. (1926). Quantization as an eigenvalue problem. *Annalen der Physik* 79(4), 361–376.
- Shi, H., H. Pan, Y.-W. Zhang, and B. I. Yakobson (2013). Strong ferromagnetism in hydrogenated monolayer mos 2 tuned by strain. *Physical Review B* 88(20), 205305.
- Son, Y.-W., M. L. Cohen, and S. G. Louie (2006a). Energy gaps in graphene nanoribbons. *Physical review letters* 97(21), 216803.
- Son, Y.-W., M. L. Cohen, and S. G. Louie (2006b). Half-metallic graphene nanoribbons. *Nature* 444(7117), 347–349.
- Splendiani, A., L. Sun, Y. Zhang, T. Li, J. Kim, C.-Y. Chim, G. Galli, and F. Wang (2010). Emerging photoluminescence in monolayer mos2. *Nano letters* 10(4), 1271–1275.
- Sreeprasad, T., P. Nguyen, N. Kim, and V. Berry (2013). Controlled, defect-guided, metal-nanoparticle incorporation onto mos2 via chemical and microwave routes: electrical, thermal, and structural properties. *Nano letters* 13(9), 4434–4441.
- Thomas, L. H. (1927). The calculation of atomic fields. In *Mathematical Proceedings of the Cambridge Philosophical Society*, Volume 23, pp. 542–548. Cambridge Univ Press.
- Torun, E., H. Sahin, S. Singh, and F. Peeters (2015). Stable half-metallic monolayers of fecl2. *Applied Physics Letters* 106(19), 192404.
- Tran, V. and L. Yang (2014). Scaling laws for the band gap and optical response of phosphorene nanoribbons. *Physical Review B* 89(24), 245407.

- Uchoa, B., C.-Y. Lin, and A. C. Neto (2008). Tailoring graphene with metals on top. *Physical Review B* 77(3), 035420.
- Wallace, P. R. (1947). The band theory of graphite. *Physical Review* 71(9), 622.
- Wang, Q. H., K. Kalantar-Zadeh, A. Kis, J. N. Coleman, and M. S. Strano (2012). Electronics and optoelectronics of two-dimensional transition metal dichalcogenides. *Nature nanotechnology* 7(11), 699–712.
- Wang, Y., L. Li, W. Yao, S. Song, J. Sun, J. Pan, X. Ren, C. Li, E. Okunishi, Y.-Q. Wang, et al. (2015). Monolayer ptse<sub>2</sub>, a new semiconducting transition-metal-dichalcogenide, epitaxially grown by direct selenization of pt. *Nano letters* 15(6), 4013–4018.
- Xu, P., L. Dong, M. Neek-Amal, M. L. Ackerman, J. Yu, S. D. Barber, J. K. Schoelz, D. Qi, F. Xu, P. M. Thibado, et al. (2014). Self-organized platinum nanoparticles on freestanding graphene. *ACS nano* 8(3), 2697–2703.
- Yin, Z., H. Li, H. Li, L. Jiang, Y. Shi, Y. Sun, G. Lu, Q. Zhang, X. Chen, and H. Zhang (2011). Single-layer mos<sub>2</sub> phototransistors. *ACS nano* 6(1), 74–80.
- Yue, R., A. T. Barton, H. Zhu, A. Azcatl, L. F. Pena, J. Wang, X. Peng, N. Lu, L. Cheng, R. Addou, et al. (2014). Hfse<sub>2</sub> thin films: 2d transition metal dichalcogenides grown by molecular beam epitaxy. *ACS nano* 9(1), 474–480.
- Zhou, J., Q. Wang, Q. Sun, X. Chen, Y. Kawazoe, and P. Jena (2009). Ferromagnetism in semihydrogenated graphene sheet. *Nano letters* 9(11), 3867–3870.
- Zhou, Z., F. Gao, and D. W. Goodman (2010). Deposition of metal clusters on single-layer graphene/ru (0001): Factors that govern cluster growth. *Surface Science* 604(13), L31–L38.
- Zhu, Z., Y. Cheng, and U. Schwingenschlöggl (2011). Giant spin-orbit-induced spin splitting in two-dimensional transition-metal dichalcogenide semiconductors. *Physical Review B* 84(15), 153402.
- Zhu, Z., S. Joshi, S. Grover, and G. Moddel (2013). Graphene geometric diodes for tera-

hertz rectennas. *Journal of Physics D: Applied Physics* 46(18), 185101.

Zhuang, H. L. and R. G. Hennig (2013). Computational search for single-layer transition-metal dichalcogenide photocatalysts. *The Journal of Physical Chemistry C* 117(40), 20440–20445.

# VITA

**Date and Place of Birth:** 12.07.1984, İzmir-TURKEY

## EDUCATION

### **2010 - 2015 Doctor of Philosophy in Physics**

Graduate School of Engineering and Sciences, İzmir Institute of Technology.

Thesis Title: Modelling Electronic and Structural Properties of Graphene and Transition Metal Chalcogenide Nanostructures

Supervisor: Prof. Dr. R. Tuğrul Senger

### **2006 - 2010 Master of Science in Physics**

Graduate School of Engineering and Sciences, İzmir Institute of Technology.

Thesis Title: Photonic Crystal Assisted L-shaped Waveguide Bend

Supervisor: Assoc. Prof. Dr. H. Sami Sözüer

### **2001 - 2006 Bachelor of Physics**

Department of Physics, Faculty of Science, İzmir Institute of Technology.

## PUBLICATIONS

Sözüer H. S. and Özeydin H. D., 2011: "Photonic crystal assisted  $90^0$  waveguide bend", International Journal of Modern Physics B, Volume 25, Number 16, Pp. 2167-2182.

Özeydin H. D., Şahin H., Senger R. T. and Peeters F. M., 2014: "Formation and diffusion characteristics of Pt clusters on Graphene", 1H-MoS<sub>2</sub> and 1T-TaS<sub>2</sub>." Annalen der Physik, Volume 526, Number 9-10, Pp. 423-429.

Bacaksız C., Şahin H., Özeydin H. D., Horzum S., Senger R. T. and Peeters F. M., 2015: "Hexagonal AlN: Dimensional-crossover-driven band-gap transition", Physical Review B, Volume 91, Number 8, Pp. 085430.

Kang J., Şahin H., Özeydin, H. D., Senger R. T. and Peeters F. M., 2015: "TiS<sub>3</sub> nanoribbons: Width-independent band gap and strain-tunable electronic properties", Physical Review B, Volume 92, Number 7, Pp. 075413.

Özeydin H. D. , Şahin H., Kang J., Senger R. T. and Peeters F. M., 2015: "Electronic and magnetic properties of 1T-TiSe<sub>2</sub> nanoribbons", 2D Materials, Volume 2, Number 4, Pp. 044002.

Özeydin H. D. and Senger R. T. 2016: "Tuning electronic and magnetic properties of TiSe<sub>2</sub> monolayer with hydrogenation", Physical Chemistry Chemical Physics (submitted).